BLOCH SURFACE WAVES IN PHOTONIC CRYSTAL FIBERS

ONDAS SUPERFICIALES DE BLOCH EN FIBRAS DE CRISTAL FOTÓNICO

Esteban González Valencia

Universidad Nacional de Colombia
Facultad de Ciencias, Escuela de Física
Medellín, Colombia
2019

BLOCH SURFACE WAVES IN PHOTONIC CRYSTAL FIBERS

Esteban González Valencia

Thesis submitted in partial fulfillment of the requirements for the degree of:
Doctor en Ciencias - Física

Advisor:
Ph.D. Pedro Ignacio Torres Trujillo

Research Group:
Grupo de Fotónica y Opto-electrónica - Universidad Nacional de Colombia Sede Medellín

Universidad Nacional de Colombia
Facultad de Ciencias, Escuela de Física
Medellín, Colombia
2019

Abstract

An electromagnetic surface wave (ESW) is a wave that travels at the interface between two media, and their fields decay exponentially on both sides of the boundary. ESWs are widely studied due to their potential applications in photonic devices and sensing applications, and some of the most relevant are the surface plasmon polaritons (SPPs), the lossy mode resonances (LMRs), and the Bloch surface waves (BSWs). BSWs are waves that propagate at the interface between an isotropic medium and a periodically non-homogeneous medium. This doctoral research is intended to demonstrate the excitation of Bloch surface waves in structures based on photonic crystal fibers (PCFs), seeking the development of new types of photonic devices and fiber-optic sensing applications. To achieve this objective, theoretical and numerical analysis were made, in addition to an experimental verification in D-shaped fibers. Multi-layer and a single-layer structures were proposed as sensing devices based on BSW excitations on PCFs. The designed structures have a high sensitivity and ultrahigh figure of merit, resulting in promising for high-resolution refractive index sensing.

Keywords: Surface electromagnetic waves; Bloch surface waves; Photonic crystals fibers; Fiber optics sensors.

Resumen

Una onda electromagnética superficial (ESW, por sus siglas en inglés) es una onda que se propaga en la interfaz entre dos medios, y sus campos decaen exponencialmente en ambos lados de la frontera. Las ESWs son ampliamente estudiadas debido a su potencial en aplicaciones de dispositivos fotónicos y aplicaciones de detección, y algunas de los más relevantes son los polaritones de plasmones de superficie (SPPs, por sus siglas en inglés), las resonancias de modos con pérdidas (LMRs, por sus siglas en inglés) y las ondas de superficiales de Bloch (BSW, por sus siglas en inglés). Los BSW son ondas que se propagan en la interfaz entre un medio isotrópico y un medio periódicamente no homogéneo. El objetivo de esta investigación doctoral es demostrar la excitación de las ondas de superficie de Bloch en estructuras basadas en fibras de cristal fotónico (PCF, por sus siglas en inglés), buscando el desarrollo de nuevos tipos de dispositivos fotónicos y aplicaciones de detección de fibra óptica. Para lograr éste objetivo, se realizaron análisis teóricos y numéricos, además de una verificación experimental en fibras en forma de D. Se propuso una estructura de múltiples capas y otra de una sola capa como dispositivos de detección basados en la excitación de BSWs en PCF. Las estructuras diseñadas tienen una alta sensibilidad y una ultra alta figura de mérito, lo que resulta prometedor para la sensado de alta resolución de índice de refracción.

Keywords: Ondas electromagnéticas superficiales; Ondas superficiales de Bloch; Fibras de crital fotónico; Sensores a fibra óptica.

Content

1. Introduction

From basic physics, it is known that the interface between two media plays an important role in various optical phenomena. For example, when a beam of light hits an interface, a part of the light is reflected and the rest is refracted; however, under certain conditions, it is possible that all light is reflected and there is no refracted ray. This phenomenon is known as total internal reflection and fiber optic technology is based on it. Even though there is not refracted light, the incident wave penetrates the second medium, which is known as the evanescent wave. This wave is mainly characterized for its exponentially decreasing amplitude the further it is from the interface.

Another less known phenomenon that takes place at the interface between two media is that light can travel at the surface, which is known as electromagnetic surface wave propagation. This wave can be considered as a surface wave if its amplitude decay exponentially on both side of the boundary. This is the main characteristic of the surface waves, which indicates that they are strongly confined at the interface. Electromagnetic surface waves (ESWs) are widely studied due to their potential applications in photonic devices and sensing applications in areas of biology, chemistry, physics, among others.

The first surface electromagnetic waves were found at the interface between a metal film and a dielectric medium and were called Surface Plasmon Polaritons (SPPs). Excitation of SPP waves has been used in multiple applications such as SPP waveguides, SPP sources, solar cells, among others [1, 2]. In addition, SPP waves have been used in the detection area, especially in thin film characterization, refractometers, biosensing, among others [1,3,4]. One of the main characteristics of SPP waves is their short propagation length which is caused by the strong absorption of the metallic layer. Because of this, there is a high interest in the surface waves between two dielectric media, since electromagnetic waves can propagate at the interface with minimum losses [5].

During the first decades after the discovery of SPPs, most surface-wave studies were focused on metal-dielectric interfaces, using increasingly complex materials and configurations. However, in the 1980s decade, the metal medium was replaced with alloys, metal oxides and eventually with dielectric media [6], leading to the study of surface waves in dielectric interfaces.

Some of the most relevant surface waves in dielectric interfaces are:

- ***Lossy mode resonances.*** It occurs when the electromagnetic wave propagates at the interface between a dielectric and a metal oxide thin film, so that the thin-film permittivity is positive and higher in magnitude than both its own imaginary part and the material surrounding the thin-film.
- ***Dyakonov Surface waves.*** These are waves that propagate at the interface between an isotropic and anisotropic medium.
- ***Bloch Surface waves.*** Also known as Tamm surface waves [7], these are waves that propagate at the interface between a isotropic medium and a periodically non-homogeneous medium.
- ***Dyakonov-Tamm Surface Waves.*** These are waves that propagate in the interface between an isotropic medium and a periodically non-homogeneous anisotropic medium.

Surface waves studies in dielectric interfaces began in the late 1970 decade, nevertheless, they have become more relevant in recent years. One of the reasons is the advances in dielectric media deposition techniques, which allowed to have a better control on the fabrication of isotropic, anisotropic, homogeneous materials and periodically non-homogeneous arrangements [6].

Most of the sensing structures based on ESW excitation proposed in the literature consist of prism-based configurations. ESW excitation in optical fibers is considered as a more compact, lightweight and robust alternative, with potential for remote and live monitoring applications [8, 9]. This is especially interesting with the actual tendency towards the concept of "lab-on-fiber"platforms for the development of modern optical system for communication and sensing applications [10].

On the other hand, the so-called photonic crystal fibers (PCFs), as will be shown below, are a relatively new type of optical fibers, characterized by having a array of holes parallel to the fiber core through the entire structure. PCFs have been extensively studied by their special properties, compared to conventional fibers. Among them we can find the possibility of confining more light in the core for long wavelengths [11], mono-mode operation at any wavelength [12], the possibility of scalar the scattering effects [13] and achieve and manipulate high birefringence values [14–18]. Some applications which use PCFs include the development of all-fiber sensing systems [14,17,19,20], advances in non-linear optics [21], the development of special light sources as high-power short pulse lasers and supercontinuum sources [13,18]. Additionally, it is possible to introduce material inside the PCF holes such as polymers, dielectrics (with different refractive indices) or conductive metal, which allows to manipulate the wave guiding properties of the fiber [22, 23].

The objective of this doctoral research is to demonstrate the excitation of Bloch surface waves in structures based on photonic crystal fibers, seeking the development of new types of photonic devices and fiber-optic sensing applications. To achieve the general objective of this thesis, three specific objectives were proposed. The first specific objective is to understand the general theory of electromagnetic surface waves in dielectric interfaces and the theoretical approach to Bloch surface waves in multilayer structures. To achieve this objective, the second chapter presents a summary of the state of the art of electromagnetic surface waves in optical fibers. In this study, the emphasis was placed on surface waves excited at dielectric interfaces. Additionally, in the third chapter, the general theory of light propagation in multilayer structures was studied. From this study, a program was written in Matlab to calculate the photonic band gaps of one-dimensional photonic crystals. Using this program is possible to design multilayer structures that support the propagation of BSWs.

The second specific objective is to study of the excitation of Bloch surface waves in photonic crystal fibers. To achieve this objective, in the third chapter a summary of the coupled mode theory (CMT) is made. Based on the CMT, another program was written in Matlab to study the excitation of BSWs in optical fibers. The obtained results were verified using computational tools to study the light propagation, which are presented in the first section of the fourth chapter. In addition, this chapter shows the first experimental verification of BSWs excited in D-shaped optical fibers.

The third specific objective is to propose a novel photonic device, or a sensing application based on Bloch surface waves in photonic crystal fibers. This objective is achieved in the fifth chapter, in which two different structures are proposed as refractive index sensing devices based on the excitation of BSWs in PCFs. The first design consists of a suspended core PCF with a multilayer structure deposited on the inner walls of its holes to excite BSWs. The second proposed structure consists of a commercial PCF, which under lateral polishing turns into a D-shaped PCF. A single dielectric layer is deposited on the flat surface of the fiber. In this case, the BSWs are excited at the interface between the bi-dimensional photonic crystal of the fiber and the coating layer.

Finally, the sixth chapter bring together the main conclusions achieve during the development of this doctoral research, and prospects of future work to continue the study of BSWs in optical fibers.

2. Electromagnetic surface waves

The origin of the study on ESWs dates back to 1907 when Jonathan Zenneck formulated the possibility that a radio wave could propagate at the interface between two media [24]. However, the concept of ESWs was first used in the late 1950s, when studies with ionic plasma in vacuum tubes showed that when electrons impact a metallic film, they suffer an unexpected energy loss. It was associated with the electronic-plasma oscillations on the surface of the film [6, 25], and was called Surface Plasmon (SP). Later, the vacuum was replaced by a dielectric material and the observed waves were called Surface Plasmon Polaritons (SPP). Because the SPP-based sensors proved to be very sensitive [26], during the last decades other types of ESWs has been studied, as the Dyakonov surface waves, the Bloch surface waves, the loosy mode resonances, among others.

2.1. Surface Plasmon Polariton

In 1958, T. Turbadar showed that when an aluminum thin layer is deposited on one side of a prism, the reflected light in this interface shows a decrease in intensity at angles above the critical, and even, for certain angles it completely disappeared [27]. However, for years it was not directly related to the excitation of surface plasmons. A decade later, in 1968, Otto introduced the attenuated total reflection method for coupling surface plasmons based on the evanescent field at the metal-dielectric interface [28], and, later this year, Kretschmann and Raether modified the Otto's configuration [29]. From these two works, the Turbadar-Otto and Turbadar-Kretschmann-Raether configurations were established as experimental methods to excite surface plasmon polariton (SPP) waves. The schemes of these two configurations are shown in Figure **2-1**.

Turbadar-Otto and Turbadar-Kretschmann-Raether configurations differ in the position of the metallic and the dielectric media with respect to the prism. However, the Turbadar-Otto configuration is less used especially in sensing applications, since the dielectric material must be sufficiently thin that the evanescent wave reaches the metal-dielectric interface, a condition that is difficult to achieve, especially in cases where the dielectric medium is a liquid

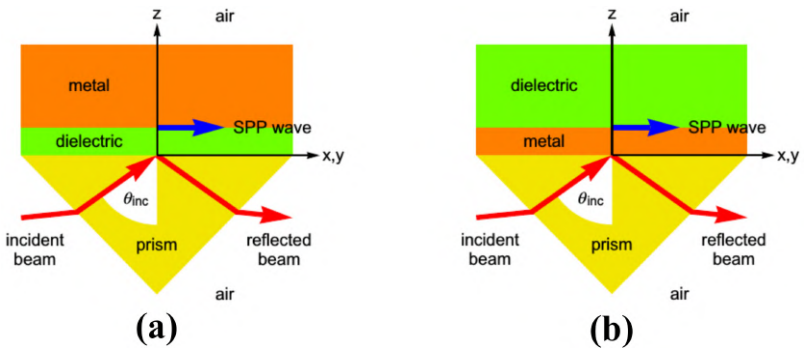

Figure 2-1.: Prism-based configurations to excite SPPs proposed by: **(a)** Turbadar-Otto and **(b)** Turbadar-Kretschmann-Raether [6].

containing the analyte. Alternatively, the Turbadar-Kretschmann-Raether configuration involves the deposition of a single thin film on the base of the prism (or placed it in contact with it), which has made it much more practical [6].

There are other methods to excite SPP without including a prism in the configuration, among them is the surface-relief grating (figure **2-2a**) in which the metal-dielectric interface has a periodic variation, forming a diffraction grating [6,30]. On the other hand, the confined light in a waveguide can excite SPP waves. It has been reported when the metal layer is directly deposited on the waveguide (figure **2-2b**)—in which the optical system becomes a simplified variation of the Kretschann-Raether configuration [31–33], or when the metallic layer is close to the waveguide but not in contact with it (figure **2-2c**)—where the SPP wave is excited by the evanescent field of the confined light [30, 34–37].

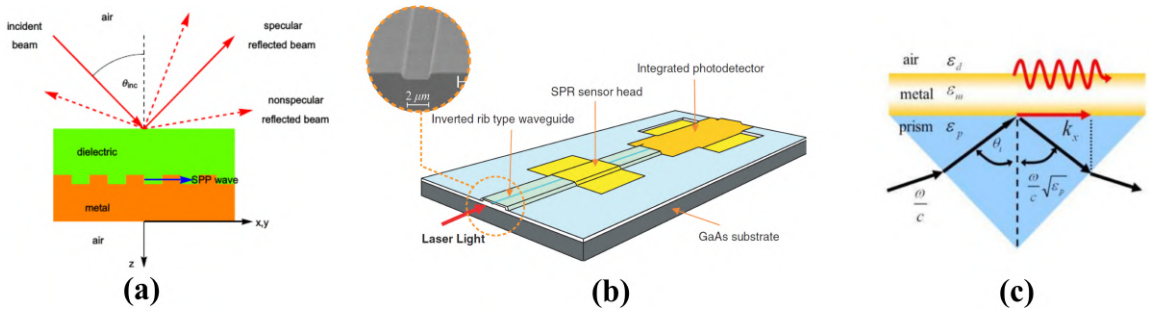

Figure 2-2.: Experimental configurations to excite SPP waves: **(a)** grating-coupled configuration [6], **(b)** metal layer deposited on the waveguide [32], and **(c)** resonance by evanescent field [34].

As thin films are widely used to excite SPP waves, it is necessary to clarify that a thin film supports different surface modes depending on the optical permittivity of the film. In the case of the surface plasmon polariton the thin film needs to be metallic in its optical character, having a negative real part of the optical permittivity which is in magnitude larger

than both that of the surrounding dielectric and its own imaginary part, then the transverse magnetic (TM) mode is labelled as an SPP wave [38, 39].

2.2. Lossy-mode resonances

As stated erlier, thin films support different surface modes depending on the optical properties of the film. Unlike SPP waves, if the real part of the thin film permittivity is positive and larger in magnitude than its own imaginary part and larger than the surrounding dielectric, the film support surface waves that exist for both polarizations (TM and TE), called lossy-mode resonances (LMR) [38] or long-range guided modes [39].

Del Villar et al. have demonstrated theoretically and experimentally that LMRs can be excited using a Turbadar-Kretschmann-Raether configuration on an indium tin oxide (ITO) layer [40, 41], using the setup shown in figure **2-3**. However, they had to use a personalized prism because it is necessary to ensure a near-grazing angle of the incident light. This condition can be achieved much easier in optical fibers, and most of the LMR research has been focused on this area [42].

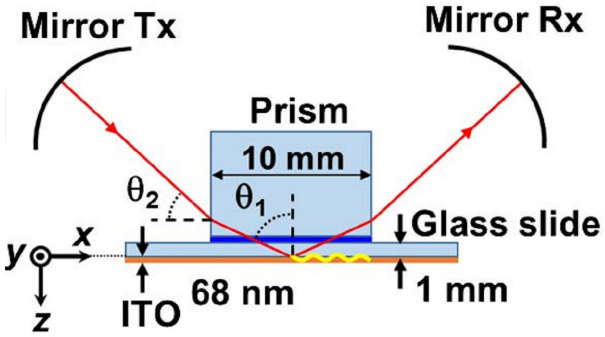

Figure 2-3.: Prism-based configuration to excite LMRs [41].

2.3. Dyakonov Surface Waves

In 1988, Dyakonov proposed that an electromagnetic wave could propagate at the interface between two dielectric materials, one of them isotropic and the other uniaxial positive, if the extraordinary axis of the birefringent medium matches the interface plane, as shown in figure **2-4a** [43]. Subsequently, the name of Dyakonov surface waves was given to the

electromagnetic waves that propagate at the interface between two dielectric media where at least one of them is anisotropic. In his studies, Dyakonov establishes that these surface waves can only propagate at certain directions, with respect to the principal axes of the uniaxial medium, which is known as the angular existence domain (AED) (figure **2-4b**).

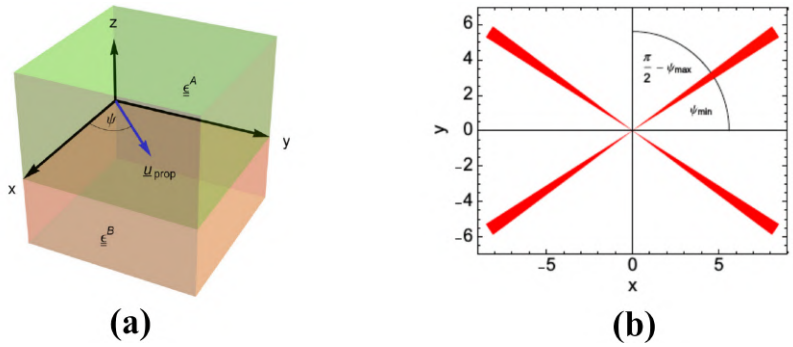

Figure 2-4.: Dyakonov surface waves: **(a)** interface between an isotropic medium $\underline{\underline{\epsilon}}^A$ and a uniaxial medium $\underline{\underline{\epsilon}}^B$, where $\underline{\mu}_{prop}$ is the direction of wave propagation; and **(b)** AED, where the propagation angle ψ is measured with respect to the x-axis, which is parallel to the extraordinary axis of the uniaxial medium [6].

However, it was not until 2009 that Takayama et al. reported a probable experimental verification of the existence of the Dyakonov waves using a modified Otto-Kretchmann configuration, as shown in figure **2-5a**. Takayama showed that using a KTP crystal (potassium titanyl phosphate) as the uniaxial medium and a index matching liquid as the isotropic one, the AED of the Dyakonov surface wave reached the value of $\Delta\psi \sim 0.1°$ (figure **2-5b**) [44]. One of the reasons that explain why this experimental verification took two decades to be achieve is the small AED values of the Dyakonov waves, which implies that they are difficult to excite. These complications caused that Dyakonov surface waves have not been widely studied for the development of photonic devices and sensing applications.

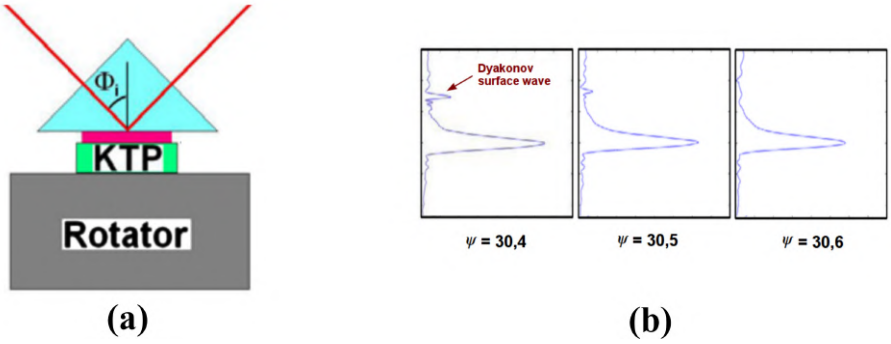

Figure 2-5.: Dyakonov surface waves: **(a)** experimental setup and **(b)** light intensity reflected for different angles ψ [44].

2.4. Dyakonov-Tamm Surface Waves

In 2007, Akhlesh Lakhtakia theoretically demonstrated the existence of a surface wave at the interface between two dielectric media, one of them homogeneous isotropic and the other one anisotropic, composed by a network of nanohelixes known as chiral sculptured thin film (CSTF) (Figure **2-6**). In this case, the surface wave satisfied the condition of the Dyakonov waves because it propagates at the interface between an isotropic medium and an anisotropic medium. Additionally, because of the nanohelixes shape, this medium can be also considered a periodically non-homogeneous (in the z-axis). This is the condition that Tamm waves (or Bloch waves) must satisfy. These waves were called Dyakonov-Tamm waves [6].

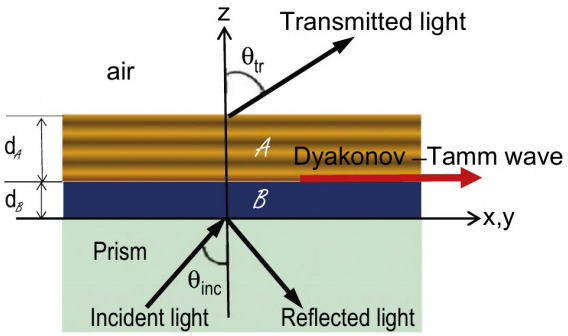

Figure 2-6.: Interface between an isotropic medium B, and a periodically non-homogeneous anisotropic medium A, to excite Dyakonov-Tamm surface waves [6].

The Dyakonov-Tamm surface waves had proved to be much easier to excite than the Dyakonov waves because their AED can be as large as 98° [45]. The experimental verification of the Dyakonov-Tamm waves was carried out in 2013 by using the prism-based setup shown in figure **2-7a**, at the interface between an isotropic medium and the CSTF medium as shown in figure **2-7b** [46, 47]. Using this structure, the first sensing application based on Dyakonov-Tamm surface waves was proposed in 2014 [48].

2.5. Bloch Surface Waves

Bloch surface waves (BSWs) are a type of waves named due to a investigation published in 1928 by the physicist Felix Bloch, who determined that a Bloch wave is a type of electron's wave function within a periodically repeating medium [49]. Other researchers called this waves as Tamm surface waves, due to the investigation published in 1932 by the physicist Igor Tamm, who determined the influence of the surface in the states of an electron close to the

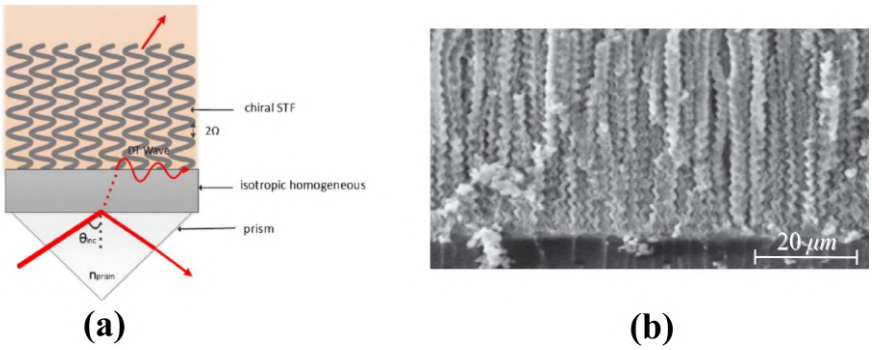

Figure 2-7.: Excitation of Dyakonov-Tamm surface waves: **(a)** experimental setup [48], and **(b)** SEM image of the CSTF structure [45].

boundary of a periodically repeating finite material [50]. The optical analog to these electron states is an electromagnetic wave guided at the interface between two media, where at least one of them should be periodically non-homogeneous in the normal direction to the interface (figure **2-8**) [5, 6]. In the simplest case, the periodically non-homogeneous medium consists of a one-dimensional photonic crystal (1DPC). The earliest studies of these electromagnetic waves go back to 1976 when Pochi Yev et al. proposed a general theory of electromagnetic wave propagation in periodic layered media [51], and one year later reported its first experimental evidence [52]. Although electromagnetic surface waves have been studied since 1977, recent advances in thin film deposition techniques allowed to increase the design possibilities and renovate the interest in the Bloch surface waves.

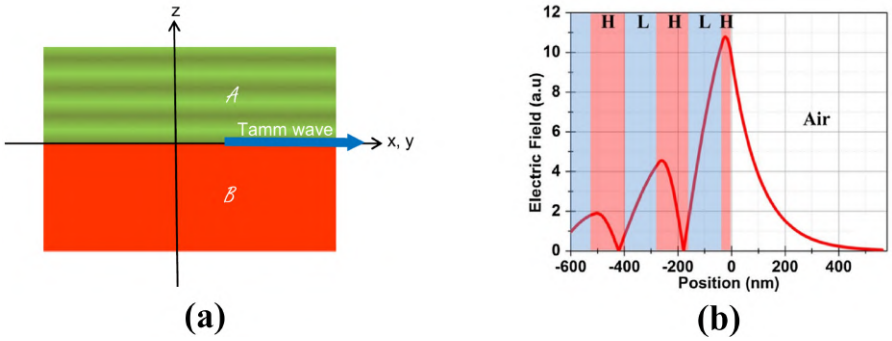

Figure 2-8.: Bloch surface waves: **(a)** interface between an isotropic medium B and a periodically non-homogeneous medium A [6], and **(b)** calculated transverse intensity distribution of a BSW [53].

Many different materials have been used in dielectric multilayer structures to excite BSWs, some of the most used are bilayers of TiO_2/SiO_2 [54–56], Si/SiO_2 [53, 57] and plasma composed by a mixture of SiH_4 and NH_3 at different concentrations [7, 58, 59]. The fabrication of these bilayers has been done mostly by chemical techniques, being Plasma Enhanced Chemical Vapor Deposition (PECVD) [7, 58, 59] and High Pressure Chemical Vapor Deposi-

tion (HPQVD) [53–56] the most widely used. Nevertheless, other techniques like sputtering systems or electron beam evaporator can also be used [60].

In contrast to Dyakonov and Dyakonov-Tamm surface waves, BSWs are excited between two isotropic media, which implies that they can propagate in any direction on the interface, having an AED of $\Delta\psi = 360°$. Therefore, BSWs were experimentally observed earlier and easier [52, 61, 62] than Dyakonov waves. In addition, the BSWs has been widely used in sensing applications based on prism-based configurations [54, 55, 57, 63–65] as well as in waveguide configurations [53, 66], as shown in figures **2-9** and **2-10**, respectively.

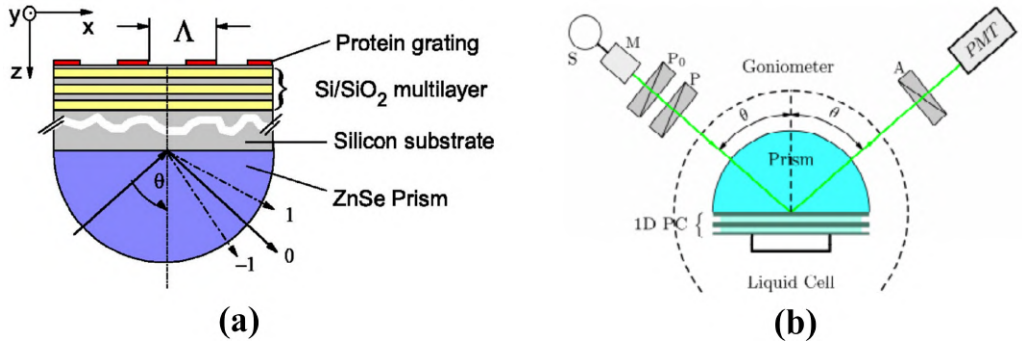

Figure 2-9.: Sensing applications on BSWs using prism-based configurations, with multilayer stacks of: **(a)** Si (267nm) / SiO_2 (324nm) [57], and **(b)** TiO_2 (96nm) / SiO_2 (140nm) [54].

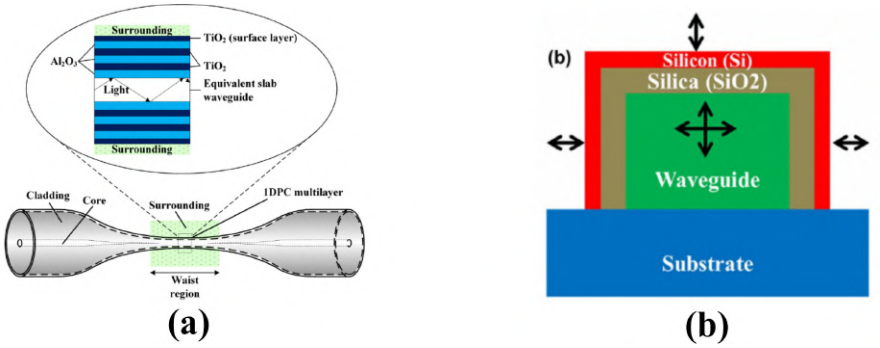

Figure 2-10.: BSWs in optical waveguides: **(a)** tapered fiber with a multilayer stack of Al_2O_3 (320nm) and TiO_2 (260nm) [66], and **(b)** rectangular waveguide with a bilayer of Si (70nm) and SiO_2 (676nm) [53].

2.6. Surface waves in optical fibers

Prism based configurations present some drawbacks as the presence of fragile mechanical parts or their relatively big sizes. Optical fibers are presented as an alternative to solve these problems by adding additional advantages such as compact design, remote sensing capabilities and immunity to electromagnetic interference, among others [67]. In general, SPP devices in optical fibers must be monitored in transmission, where variations in transmitted power indicate that the evanescent field of the light traveling along the fiber core has been coupled to an a surface wave. This coupling has a strong dependence on the light wavelength, the optical properties of the metal film (refractive index and extinction coefficient), thickness of the deposited film(s), fiber geometry, among others. The first designs of optical fiber SPP sensors were made by removing a small section of the fiber cladding and the core was coated with a metallic layer. Afterward, SPP waves have been excited in many types of optical fibers as shown in figure **2-11**, including single-mode fibers [68–70], multimode fibers [3, 71]; post-processed fibers such as tapered fibers [72–74], D-type fibers [24, 35, 75, 76] and H-type fibers [77].

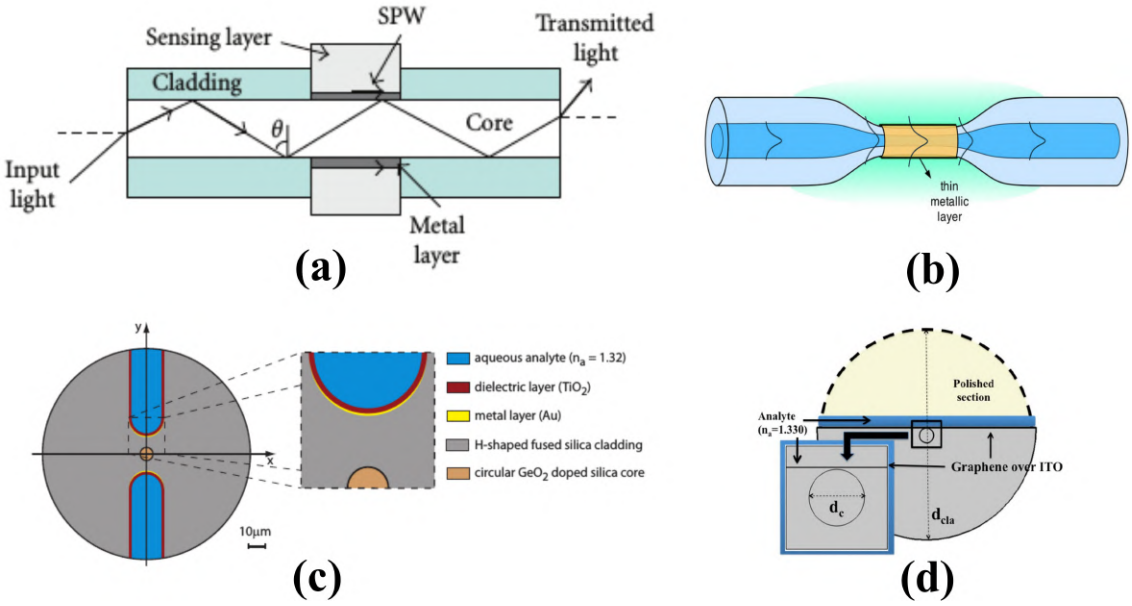

Figure 2-11.: Experimental setups used to excite SPP waves in optical fibers: **(a)** multimode fiber [31], **(b)** tappered fiber [72], **(c)** H-type fiber [77], **(d)** D-type fiber [35].

In 2006, a photonic crystal waveguide sensor based on SPP excitation was proposed [78], and later the first proposal for an SPP sensor in a PCF was made [79]. From there, many types of PCF have been designed to excite SPP waves, some of them are shown in the figure **2-12**. Additionally, in recent years the PCF manufacture techniques have been progressing,

and new configurations have been explored to improve SPP-based sensors. Among them, the suspended core fiber has gained especial relevance in sensing applications [80–82], which has allowed developing new configurations based on SPP wave excitation [36, 73, 83], some of these are shown in figure **2-13**.

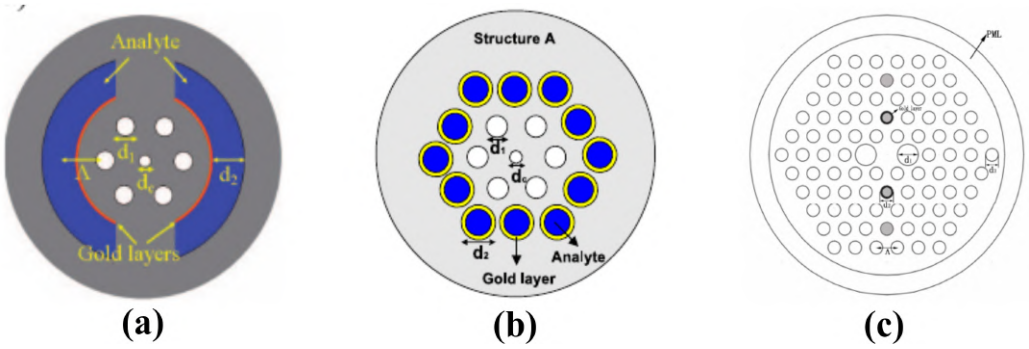

Figure 2-12.: Proposed photonic crystal fiber designs to excite SPP waves. Taken from: **(a)** [31], **(b)** [31, 84], **(c)** [85].

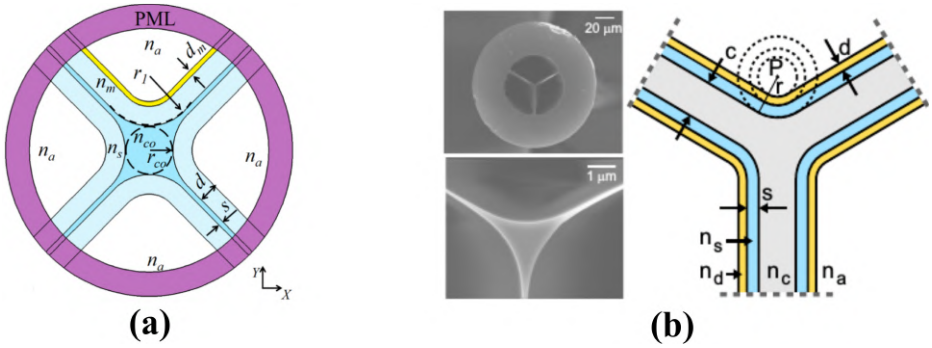

Figure 2-13.: Proposed SPP sensors based on suspended core PCF. Taken from: **(a)** [86], **(b)** [83].

On the other hand, and as mentioned earlier, the LMR waves are only excited when the incident light has a near-grazing angle, an optimal condition for optical fiber excitation [41, 42]. The first fiber optic LMR sensor was proposed in 2010 by Del Villar et al., and consisted of an ITO thin film coating the core of a post-processed multimode fiber [87]. However, in an investigation published in 2008 consisted of a metal oxide thin film deposited on a laterally polished fiber, no mention was made of the LMRs [88].

Besides ITO, some materials that permit the generation of LMRs are polymers and metallic oxides, however, latter have some advantages such as a flatter surface of thin films. Some of the metallic oxides used in LMR generation in optical fibers are tin dioxide (SnO_2) [89], cooper oxide (CuO) [90], titanium oxide (TiO_2) [91]. Some of the applications in which LMRs sensors have been used include refractometry [87,90,91], humidity sensors [92,93], pH

sensors [94,95], gas detection [96,97] and biosensing [98,99]. The main configurations used in the generation of LMR in optical fibers are the cladding-off multimode fiber [87,89], tapered fibers [100] and side polished (D-shaped) [38,95], as shown in figure **2-14**.

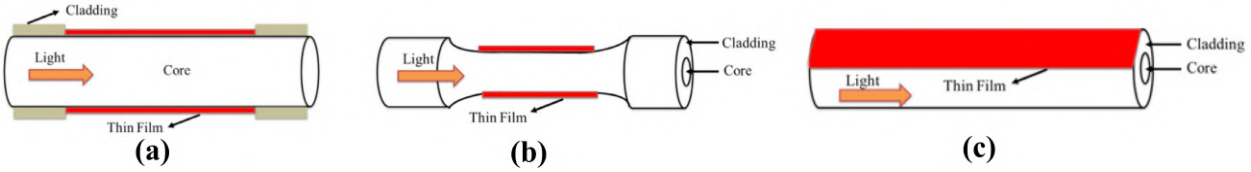

Figure 2-14.: Schematic of LMR-based sensors [67]: **(a)** cladding-off multimode fiber **(b)** Tappered fiber **(c)** D-shaped fiber

.

Finally, since 2015 there have been presented some designs of BSW excitation in optical fibers. In the first reported case, Shuna Li et al. proposed and numerically analyzed the use of a D-shaped single-mode optical fiber on whose flat surface can be deposited seven dielectric bilayers of TiO_2/SiO_2 to excite BSWs at 785 nm. In this paper, they assumed that the planar layer reaches the fiber core and the dielectric layers were directly deposited on it, as shown in figure **2-15**. In this case, the setup is similar to the prism-based configurations, and the light incidence angle θ was determined by the light wavelength [56].

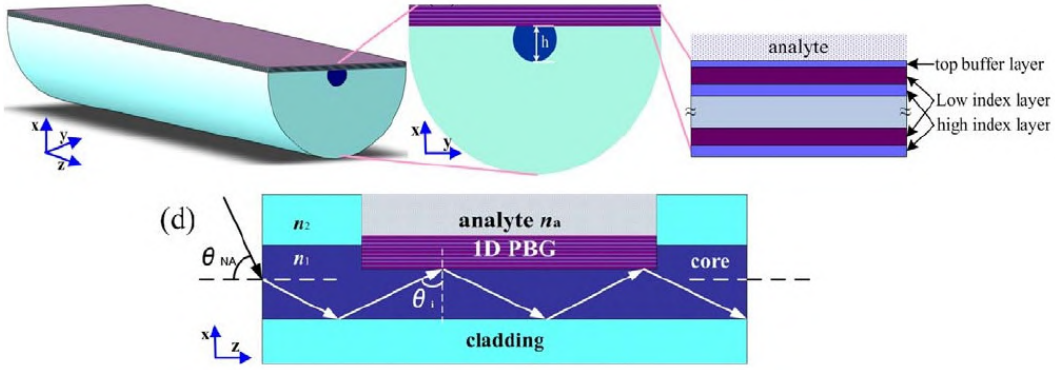

Figure 2-15.: Schematic of a multilayer structure on a D-shaped fiber to excite BSWs. The multilayer stack of TiO_2 (125nm) and SiO_2 (275nm) [56]

In 2016, Scaravilli et al. studied the possibility to excite BSWs on the tip of single mode optical fibers using a grating-coupled configuration and demonstrated it experimentally in 2018. They proposed two different configurations, the first one consisted in writing a diffraction grating on the fiber tip and latter in depositing a 1DPC of N dielectric bilayers of SiO/SiO_2 on it (figure **2-16a**). In the alternative configuration, the 1DPC is first deposited and the diffraction grating is placed on the surface of the photonic crystal (figure **2-16b**) [9,101,102].

In addition, in 2016 Xiao-Jie Tan et al. presented a theoretical study of a fiber sensor based

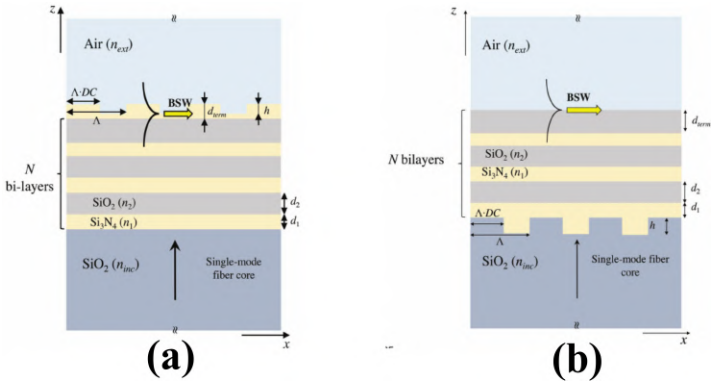

Figure 2-16.: Schematic of the on-tip diffraction-grating configuration to excite BSWs. The diffraction grating is written on: **(a)** the fiber tip, and **(b)** the top layer of the 1DPC. The thicknesses of the Si_3N_4/SiO_2 stacks are 350nm/760nm and 375nm/370nm, respectively [9]

on BSWs. The designed structure consists of a cladding-off multimode fiber, where a six layers 1DPC is deposited (in an omnidirectional direction) on its outer surface, as shown in figure **2-17** [103].

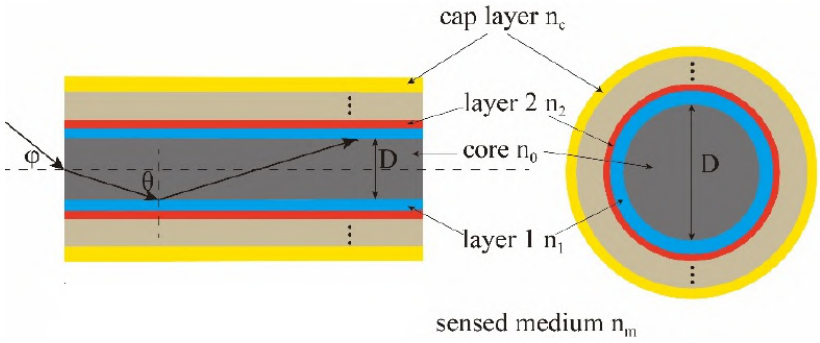

Figure 2-17.: Schematic of an omnidirectional 1DPC coating the core of a multimode fiber [103].

2.7. Summary

In summary, the research on ESW excitation has resulted in innovative technological developments. For several decades these advances were concentrated in SPPs, however recent advances have allowed the study and implementation of devices based on other types of surface waves. In particular, ESWs in dielectric interfaces have gained special relevance, within which we highlight the BSWs for their potential in communications and sensing applications.

Currently, some advances in BSW excitation in optical fibers have already been presented. Therefore, we consider that the next step is the implementation of BSW-based devices integrated into non-conventional optical fibers, such as PCFs, in order to take advantage of the unique features they can offer.

3. Theoretical background

This chapter presents a summary of the theoretical background on which this investigation is based. The first section shows how the electromagnetic analysis of light propagation in a inhomogeneous dielectric medium can be projected as a linear eigenvalues problem. This is the physical principle used by *COMSOL Multiphysics*, software used in large part of the numerical calculations performed in the development of this thesis. Subsequently, the analysis of the transmission bands of a one-dimensional photonic crystal is presented, which is highly helpful to design a photonic crystal that sustains BSWs in the desired wavelength range. Finally, the coupled mode theory (CMT) is presented. The CMT was studied to analyze how the light traveling through the fiber core can couple to a deposited photonic crystal in the vicinity, and calculate the expected transmission curves.

3.1. Electromagnetism as an eigenvalue problem

Maxwell's Equations provide a complete description of electromagnetic phenomena and support all modern information and communication technologies. Through them, it is possible to derive the electromagnetic wave equations. If there are not free charges or currents, Maxwell's equations in SI units are given by:

$$\nabla \times \vec{E}(r,t) = -\frac{\partial \vec{B}(r,t)}{\partial t} \qquad \nabla \cdot \vec{D}(r,t) = 0 \tag{3-1}$$

$$\nabla \times \vec{H}(r,t) = \frac{\partial \vec{D}(r,t)}{\partial t} \qquad \nabla \cdot \vec{B}(r,t) = 0 \tag{3-2}$$

where $\vec{E}$ is the electric field vector, $\vec{H}$ is the magnetic field vector, $\vec{D}$ is the electric flux density vector and $\vec{B}$ is the magnetic flux density vector. If the material is assumed as non-magnetic, linear, isotropic, real and lossless, the electromagnetic fields $\vec{E}$, $\vec{H}$, $\vec{D}$ and $\vec{B}$ can be related as:

$$\vec{D}(r,t) = \varepsilon \vec{E}(r,t) \qquad \vec{B}(r,t) = \mu \vec{H}(r,t) \tag{3-3}$$

where ε is the electrical permittivity and μ is the magnetic permeability, which due to the non-magnetic condition, is equal to the vacuum magnetic permeability ($\mu = \mu_0$). As the Maxwell equations are linear it is possible to separate the time dependence from the spacial dependence of the electric and magnetic fields, as:

$$E(r,t) = E(r)e^{-iwt} \qquad H(r,t) = H(r)e^{-iwt} \tag{3-4}$$

Combining equations (3-1) to (3-4) we get:

$$\nabla \times \vec{E}(r) = -i\omega\mu\vec{H}(r) \qquad \nabla \times \vec{H}(r) = i\omega\varepsilon\vec{E}(r) \tag{3-5}$$

Finally, replacing $\vec{E}(r)$ from equations (3-5), we have:

$$\nabla \times \left(\frac{1}{i\omega\varepsilon}\nabla \times \vec{H}(r)\right) = -i\omega\mu\vec{H}(r) \tag{3-6}$$

then:

$$\nabla \times \left(\frac{1}{\varepsilon}\nabla \times \vec{H}(r)\right) - \omega^2\mu\vec{H}(r) = 0 \tag{3-7}$$

Equation (3-7) is known as the wave equation, which has the form of an eigenvalue equation with eigenfunctions $H(r)$ and eigenvalues $\omega^2\mu$. For mathematical convenience, the wave equation is preferred for $\vec{H}(r)$ instead of $\vec{E}(r)$ because the operator acting on the former is Hermitian, which simplifies the problem [104]. Considering the material-hole distribution, the wave equation solutions for photonic crystal fibers are much more complex than the solutions for standard optical fibers. As the PCF shape significantly changes the light propagation properties, its modal analysis is usually done through computational tools such as finite elements method (FEM) and finite difference time domain method (FDTD) [105].

The FEM allows to solve the wave equation and have an approximate solution, through the discretization of fiber transverse section into small elements, transforming the problem in (3-7) into a matrix form problem given by [106]:

$$\left([A] - n_{eff}^2[B]\right)\{h\} = 0 \tag{3-8}$$

where $\{h\}$ are the eigenvectors and n_{eff}, the effective refractive index, are the eigenvalues.

3.1.1. Photonic crystal fibers

Microstructured optical fibers (MOF) are (typically) silica fibers, in which a holes arrangement (that extends in the axial direction of the fiber) is generated in their cladding region during their manufacturing process [107]. There are some MOF cases of special interest in which the hole arrangement is periodic and the fibers are known as photonic crystal fibers (PCF) [108]. Currently, the difference between the terms MOF and PCF is increasingly diffuse; in fact, today both are used interchangeably to refer to holey optical fibers.

The presence of a arrengement of holes inside the optical fiber modifies the conditions of light transmission, which allows the PCFs to have special optical properties beyond the possibilities of conventional single mode and multimode fibers [11–18,109]. Figure **3-1** shows SEM images of some PCF transverse sections to evidence the wide diversity of size, shape and holes distribution that these fibers may have.

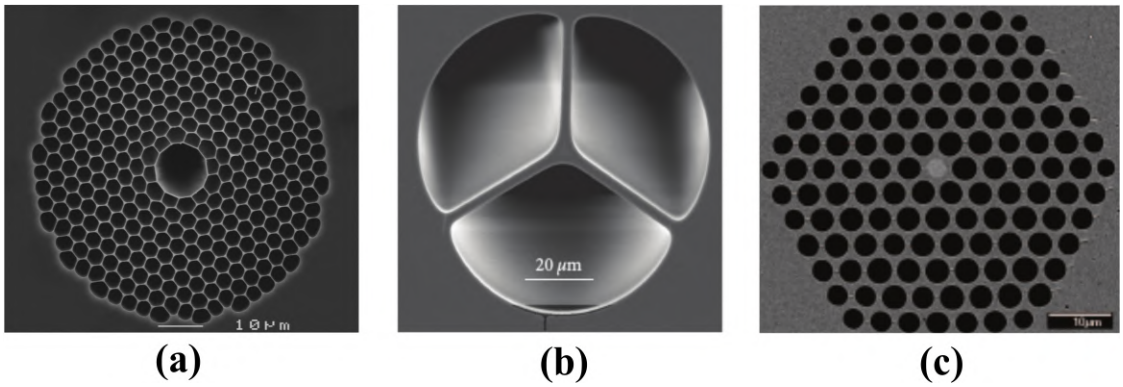

Figure 3-1.: Some configurations of photonic crystal fibers: **(a)** Hollow core PCF [109], **(b)** suspended core PCF [82], and **(c)** doped core PCF [110].

With the development of new PCF designs, light propagation properties of PCFs can be tuned by filling the micro-holes with different materials, among them we can find gases [111], liquids [112,113], metals [114] and stress-generating elements (PANDA fibers) [115,116], the last two are shown in figure **3-2**. Our interest of working with these special fibers is to take advantage of their geometry and analyze the response of controlled depositions of dielectric materials to excite Bloch surface waves inside an optical fiber.

In general, the PCFs have a complex structure and its huge potential in terms of hole shapes

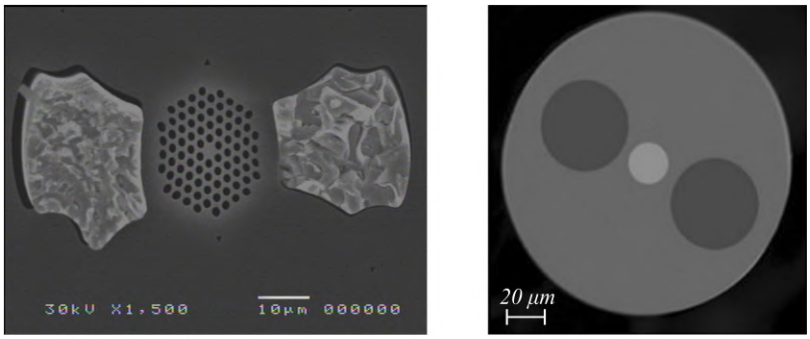

Figure 3-2.: PCF holes filled with: **(a)** internal electrodes [114] and **(b)** stress-generating elements [116].

and arrangement makes difficult to find them a mathematical solution. Many PCF cases are practically impossible to solve analytically, so Maxwell equations must be numerically solved [105, 117].

3.2. Electromagnetic propagation in multilayer structures

Recent advances in dielectric deposition techniques have made possible multilayer growth with constant periodicity, so these structures can be considered as an optical medium [51]. In the simplest case of a periodic stratified structure, exemplified in the figure **3-3**, the refractive index profile is given by:

$$n(x) = \begin{cases} n_2, & 0 < x < b \\ n_1, & b < x < \Lambda \end{cases} \tag{3-9}$$

where Λ is the period, the direction x is normal to the interfaces, and $n(x + \Lambda) = n(x)$.

The distribution of the electric fields can be written in the form $E(x, z) = E(x)e^{i\beta z}$. In addition, in each layer the electric field can be expressed as the sum of the incident and reflected plane wave's electric field. The complex amplitudes of the incident and reflected waves, $a_n^{(\alpha)}$ and $b_n^{(\alpha)}$, at the α layer of the n_{th} unit cell, constitute the components of a column vector $E(x)$. The electric field distribution in the same layer can be written as:

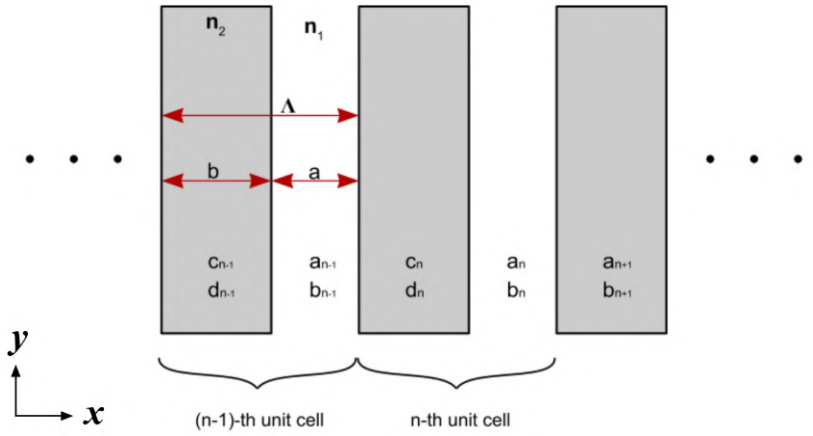

Figure 3-3.: Periodic stratified medium [51].

$$E(x,z) = \left(a_n^{(\alpha)} e^{ik_{\alpha x}(x-n\Lambda)} + b_n^{(\alpha)} e^{-ik_{\alpha x}(x-n\Lambda)}\right) e^{i\beta z} \tag{3-10}$$

where $k_{\alpha x} = \{[(w/c)n_\alpha]^2 - \beta^2\}^{1/2}$ and $\alpha = 1, 2$. The column vectors are related through the continuity conditions at the interfaces, so they are not independent of each other. Imposing the E and $\partial E/\partial z$ continuity conditions at the interface leads to:

$$\begin{bmatrix} a_{n-1} \\ b_{n-1} \end{bmatrix} = \begin{bmatrix} A & B \\ C & D \end{bmatrix} \begin{bmatrix} a_n \\ b_n \end{bmatrix} \tag{3-11}$$

Equation (3-11) is the unit cell translation matrix which relates the complex amplitudes of the incident plane wave a_{n-1} and the reflected plane wave b_{n-1} in one layer of a unit cell to those of the equivalent layer in the next unit cell.

For TE modes the matrix elements are given by:

$$A_{TE} = e^{-ik_{1x}a}\left[\cos(k_{2x}b) - \frac{1}{2}i\left(\frac{k_{2x}}{k_{1x}} + \frac{k_{1x}}{k_{2x}}\right)\sin(k_{2x}b)\right] \tag{3-12}$$

$$B_{TE} = e^{ik_{1x}a}\left[-\frac{1}{2}i\left(\frac{k_{2x}}{k_{1x}} - \frac{k_{1x}}{k_{2x}}\right)\sin(k_{2x}b)\right] \tag{3-13}$$

$$C_{TE} = e^{-ik_{1x}a}\left[\frac{1}{2}i\left(\frac{k_{2x}}{k_{1x}} + \frac{k_{1x}}{k_{2x}}\right)\sin(k_{2x}b)\right] \tag{3-14}$$

$$D_{TE} = e^{ik_{1x}a}\left[\cos(k_{2x}b) + \frac{1}{2}i\left(\frac{k_{2x}}{k_{1x}} + \frac{k_{1x}}{k_{2x}}\right)\sin(k_{2x}b)\right] \tag{3-15}$$

For TM modes the matrix elements are given by:

$$A_{TM} = e^{-ik_{1x}a}\left[\cos(k_{2x}b) - \frac{1}{2}i\left(\frac{n_2^2 k_{1x}}{n_1^2 k_{2x}} + \frac{n_1^2 k_{2x}}{n_2^2 k_{1x}}\right)\sin(k_{2x}b)\right] \tag{3-16}$$

$$B_{TM} = e^{ik_{1x}a}\left[-\frac{1}{2}i\left(\frac{n_2^2 k_{1x}}{n_1^2 k_{2x}} - \frac{n_1^2 k_{2x}}{n_2^2 k_{1x}}\right)\sin(k_{2x}b)\right] \tag{3-17}$$

$$C_{TM} = e^{-ik_{1x}a}\left[\frac{1}{2}i\left(\frac{n_2^2 k_{1x}}{n_1^2 k_{2x}} - \frac{n_1^2 k_{2x}}{n_2^2 k_{1x}}\right)\sin(k_{2x}b)\right] \tag{3-18}$$

$$D_{TM} = e^{ik_{1x}a}\left[\cos(k_{2x}b) + \frac{1}{2}i\left(\frac{n_2^2 k_{1x}}{n_1^2 k_{2x}} + \frac{n_1^2 k_{2x}}{n_2^2 k_{1x}}\right)\sin(k_{2x}b)\right] \tag{3-19}$$

According to the Floquet theorem, a propagating wave is in the form:

$$E_K(x,z) = E_K(x)e^{iKx}e^{i\beta z} \tag{3-20}$$

where $E_K(x)$ is periodic, such as $E_K(x) = E_K(x+\Lambda)$, and the constant K is known as the Bloch wave number. Using equation (3-10), the periodic condition for the Bloch wave can be written as:

$$\begin{bmatrix} a_n \\ b_n \end{bmatrix} = e^{iK\Lambda}\begin{bmatrix} a_{n-1} \\ b_{n-1} \end{bmatrix} \tag{3-21}$$

From the unit cell translation matrix (equation (3-11)) and equation (3-21), it follows that Bloch wave satisfies the eigenvalue problem:

$$\begin{bmatrix} A & B \\ C & D \end{bmatrix}\begin{bmatrix} a_n \\ b_n \end{bmatrix} = e^{-iK\Lambda}\begin{bmatrix} a_n \\ b_n \end{bmatrix} \tag{3-22}$$

where the phase factor $e^{-iK\Lambda}$ are the eigenvalues of the translation matrix. From equation (3-22), one can know that they are given by:

$$e^{iK\Lambda} = \frac{1}{2}(A+D) \pm \left\{\left[\frac{1}{2}(A+D)\right]^2 - 1\right\}^{1/2} \tag{3-23}$$

For the Bloch wave function, equation (3-23) gives the dispersion relation between ω, β and K:

$$K(\beta,\omega) = \frac{1}{\Lambda}\cos^{-1}\left[\frac{1}{2}(A+D)\right] \tag{3-24}$$

When $\left|\frac{1}{2}(A+D)\right| < 1$, K is real and thus there is propagating Bloch wave in the periodic structure. On the other side, when $\left|\frac{1}{2}(A+D)\right| > 1$, K has an imaginary part and the Bloch wave is evanescent in the structure. These are the forbidden bands of a periodic medium.

3.2.1. Photonic band analysis of the 1DPC

The transfer matrix method analysis of the allowed and the forbidden bands of a one-dimensional photonic crystal is presented in the form of a graph, usually named as the band structure. The band structure, also called band diagram or dispersion diagram, is the frequency vs. wave vector graph, calculated for each multilayer structure. Figure **3-4** shows an example of a 1DPC band structure [54], in which is possible to identify some white areas that represent the so-called "forbidden" bands (or non-radiative regions), and the colored areas represent the so-called "allowed" bands (or radiative regions). The forbidden bands are characterized by having a Bloch wavenumber whose imaginary part makes evanescent the Bloch wave component [51]. This means that the Bloch wave cannot propagate inside the 1DPC, contrary to the allowed bands, in which the Bloch wave can propagate within the structure.

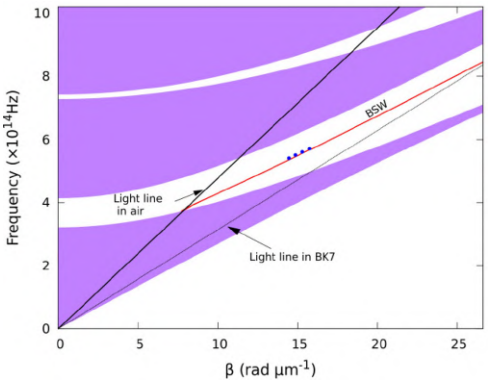

Figure 3-4.: Band diagram of a SiO_2/TiO_2 1DPC, deposited on a prism made of $BK7$ glass, for the TE polarization. The layers thickness are $d_{SiO_2} = 140\ nm$ and $d_{TiO_2} = 96\ nm$ [54].

We are interested in the Bloch surface waves, i.e. those waves that cannot propagate through the 1DPC, which exist in the forbidden bands of the dispersion diagram, and down the light in the air line [54].

To analyze the photonic bands of the 1DPCs, a code was implemented in Matlab named $1DPC\ BandGap$ (see Appendix A) based on the Pochi Yeh et al. general theory [51]. The code was tested by reproducing some results of published references. As an example, figures **3-5** and **3-6** show a direct comparison between the published graphs **(a)** and their reproductions **(b)** made with the $1DPC\ BandGap$ code.

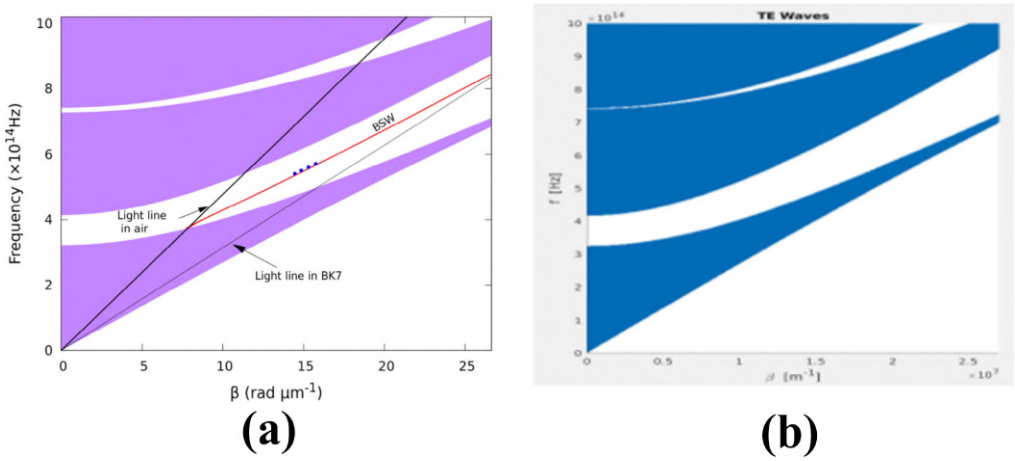

Figure 3-5.: TE Band diagram of a SiO_2/TiO_2 1DPC: **(a)** Published graph [54], and **(b)** graph reproduction.

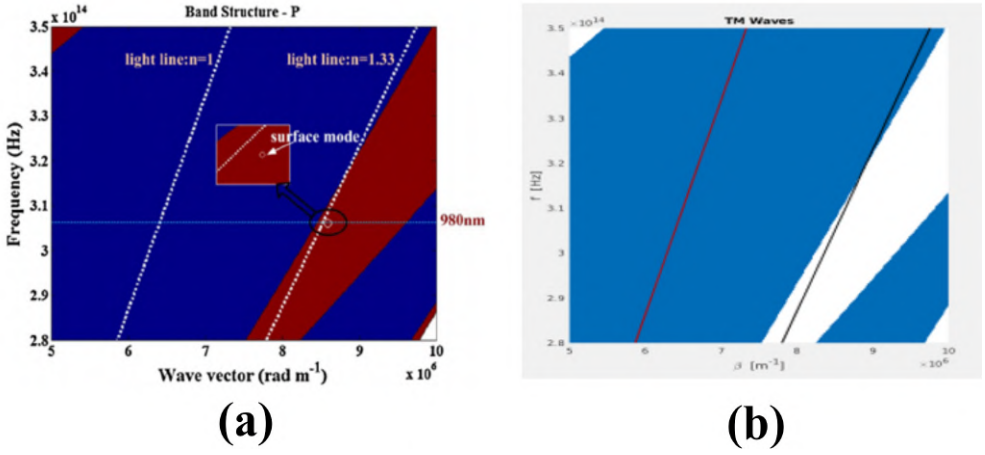

Figure 3-6.: TM Band diagram of a SiO_2/TiO_2 1DPC: **(a)** Published graph [55], and **(a)** graph reproduction.

3.3. Coupled modes theory

The electromagnetic wave propagation in optical fibers is described in terms of normal modes. However, these modes retain their identity only in perfect waveguides without irregularities in their refractive index distribution and their waveguide geometry. Propagation of electromagnetic waves in waveguides with any irregularities must be described using coupled modes theory (CMT) [118]. For example, CMT is commonly used for analyzing multimode and multicore fibers based on a perturbational approach [119]. In our case, the PCF will be assumed as a two cores waveguide, the fiber core and the multilayer structure. Each one can be analyzed independently, and the interactions between them are considered a perturbation to the whole system. Assuming that the fiber is not absorbent, the electric field can be treated as a linear superposition of the individual core fields, as:

$$E(x,y,z) = A_1(z)e^{-i\beta_1 z}E_1(x,y) + A_2(z)e^{-i\beta_2 z}E_2(x,y) \tag{3-25}$$

The subscripts 1 and 2 refers to the fiber core and the multilayer structure respectively, $E_{1,2}$, $A_{1,2}$, and $\beta_{1,2}$ are the electric field distributions, amplitudes and propagation constants of the propagating modes in each isolated core, respectively. The coupled mode equation can be written as:

$$\frac{d}{dz}\begin{bmatrix} A_1 \\ A_2 \end{bmatrix} = i\begin{bmatrix} \beta_1 & \kappa_{12} \\ \kappa_{21} & \beta_2 \end{bmatrix}\begin{bmatrix} A_1 \\ A_2 \end{bmatrix} \tag{3-26}$$

The coupling coefficients κ_{jl} are defined as:

$$\kappa_{jl} = \frac{k_0}{2n_{co,j}} \frac{\int_A (n^2 - n_l^2)E_j^* \cdot E_l \, \mathrm{d}A}{\int_A E_j^* \cdot E_j \, \mathrm{d}A} \tag{3-27}$$

where $(j,l) = (1,2)$ *or* $(2,1)$ and the longitudinal field components are ignored [120]. In equation (3-27) k_0 is the vacuum wave number, n is the refractive index profile of the whole system, n_l is the refractive index profile of the system for the each isolated l-th core, $n_{co,j}$ is the refractive index of the j-th core, and A is the cross-section. In a step-index dual-core fiber the coupling coefficients can be calculated analytically using equation (3-27), but in a PCF with a multilayer structure, a numerical modeling such as finite elements method (FEM) should be used.

The resulting system of differential equations from (3-26) can be used to study the light coupling between two waveguides. For example, it is possible to analyze a system composed

of an optical fiber (A_1) with a dielectric structure (A_2) (single or multilayer) as close to the core that its evanescent field interacts with this dielectric structure. In these cases, it can be assumed as the initial condition that beam light is only injected through the fiber core; therefore $A_2(0) = 0$. As the light propagates in the fiber core (in the z-direction) it can be coupled to the second waveguide, then the solutions $A_1(z)$ and $A_2(z)$ will be the electric field amplitudes of the fiber core mode and the propagating wave mode in the dielectric structure, respectively. It is important to highlight that these electric field amplitudes depend on the distance (z) that light propagates in the perturbed system.

3.3.1. CMT analysis in an optical fiber

The CMT was selected to analyze how the light traveling in the fiber core can be coupled to a multilayer structure and excite surface modes. The CMT was implemented by writing a Matlab code integrated for a general program called CMT and two secondary program called $Script\_Coupling$ and $Script\_Transmission$. These program can be found in Appendix B, and by using them it is possible to calculate the expected transmission spectra, for a given propagation length. To execute the CMT program it is necessary to know the electric field distribution on the fiber cross section, for each one of the independently involved modes.

In this case, the first mode corresponds to the light traveling through the core of the optical fiber, while the second mode corresponds to the excited wave in the deposited structure. The modal analysis to get the electric field distribution of each mode was made in the commercial software *COMSOL Multiphysics*, which is a cross-platform FEM solver and multiphysics simulation software.

To corroborate the method, a D-shaped fiber was analyzed with a tin dioxide ribbon deposited on its flat surface, as shown in figure **3-7**. The analysis was completed with the implemented CMT method and with the commercial software *FIMMWAVE/FIMMPROP*, which is a tool for simulating propagation in optical waveguides.

To study the light coupling performance as a function of the propagation length, two different cases were analyzed, 2 mm and 17 mm. The transmission curves obtained with CMT method and *FIMMWAVE* are shown in figures **3-8** and **3-9**, respectively. It can be seen that even though the calculation procedures are quite different, the results obtained with the two methods are accurate correspond to each other.

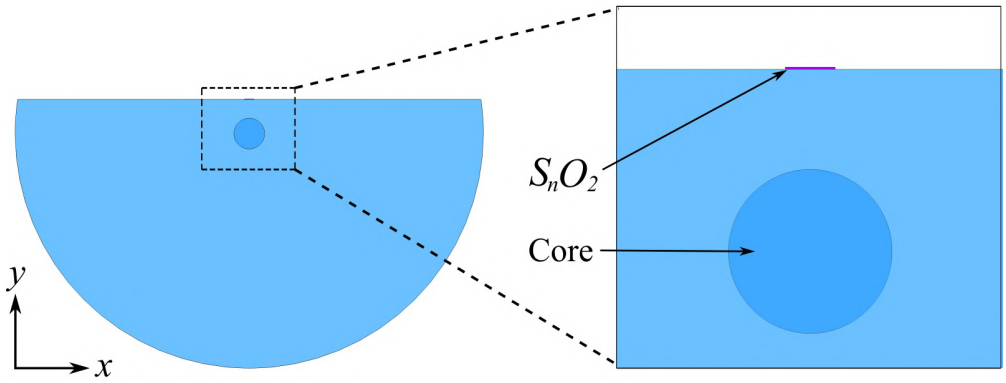

Figure 3-7.: Schematic of a single mode D-shaped fiber with a tin dioxide ribbon deposited on its flat surface. The ribbon width is 2.5 μm and its thickness is 110 nm, while the fiber core and cladding diameter are 8.2 μm and 125 μm.

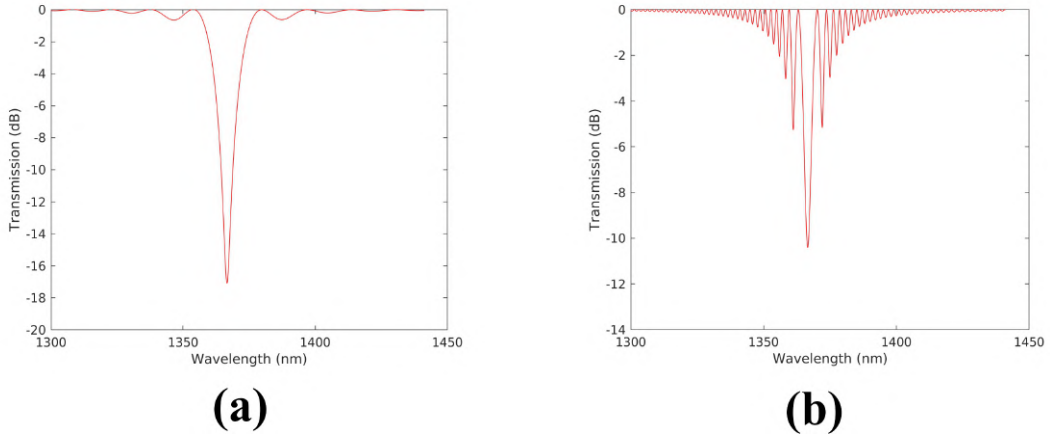

Figure 3-8.: Transmission curves of the proposed structure calculated with the CMT implementation for a propagation length of: **(a)** 2 mm, and **(b)** 17 mm.

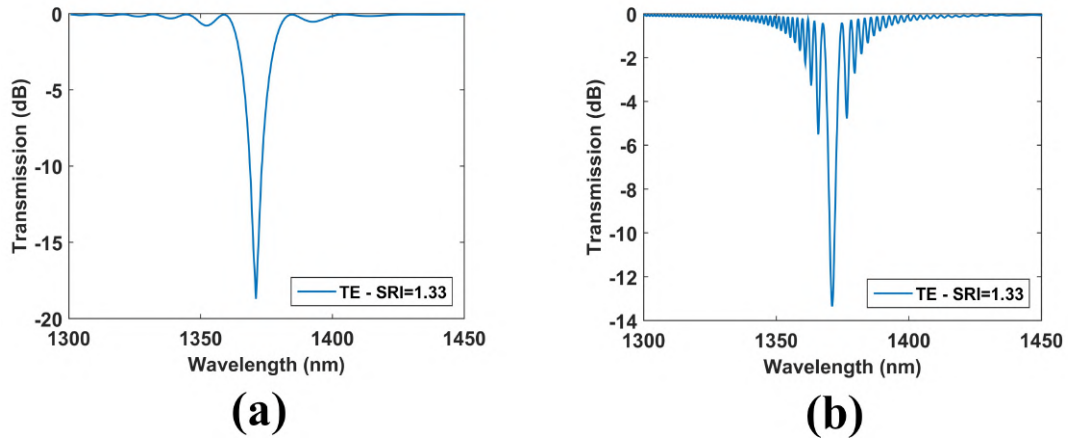

Figure 3-9.: Transmission curves of the proposed structure calculated with *FIMMWAVE* for a propagation length of: **(a)** 2 mm, and **(b)** 17 mm.

3.4. Summary

In summary, in this chapter, the basic theory of light propagation in multilayer structures and the coupled modes theory was reviewed. Additionally, it was implemented a methodology to analyze the light coupling between two waveguides using the CMT, where the electric fields of the propagating modes are calculated using a commercial FEM software. This implementation has great potential since it can be used to study the excitation of surface waves in lossless media. In addition, the CMT implementation can be used to study any system composed of two waveguides, close enough for the evanescent fields to interact and be coupled between them.

4. Experimental verification of BSWs in optical fibers

So far, very few investigations on the BSW excitation in optical fibers have been published, and not all of them have experimental verification. All these works have in common that the configuration used to excite BSWs are essentially variations of the prism-based setups, where the light is incident directly on the photonic crystal. In this chapter, we propose to excite BSWs in a D-shaped single-mode optical fiber through the evanescent field of the light traveling through the fiber core. The first section of this chapter presents an analysis of the optical properties of a single SnO_2 coating film on the planar section of a D-shaped fiber. Then, the design process of the photonic crystal that will be deposited in the D-shaped fiber is shown, and the expected transmission spectra for different numbers of 1DPC layers are calculated. The following section presents the experimental setup used in the depositions of metallic oxide thin films of the 1DPC in the D-shaped fiber. The deposition process is monitored by continuously measuring the transmission spectrum and controlling the thickness of each layer of the 1DPC. Then, a sensitivity analysis of the coated D-shaped fibers is made, by changing the refractive index of the external medium. Finally, a summary of the results is presented.

4.1. Deposition of metallic oxides on D-shaped optical fibers

In order to experimentally verify the excitation of Bloch surface waves in optical fibers, side polished fibers (D-shaped) supplied by the company *Phoenix Photonics* were used. The thin films was deposited using the **Emitech K675X** sputter coater system, using a SnO_2 target from *Plasmaterials, Inc.* and a CuO target from *ZhongNuo Advanced Material Co.*

Ellipsometry was used to measure the refractive index and extinction coefficient of the deposited thin films, using coated microscope slides. The ellipsometry results for SnO_2 and CuO

thin films are shown in figure **4-1**.

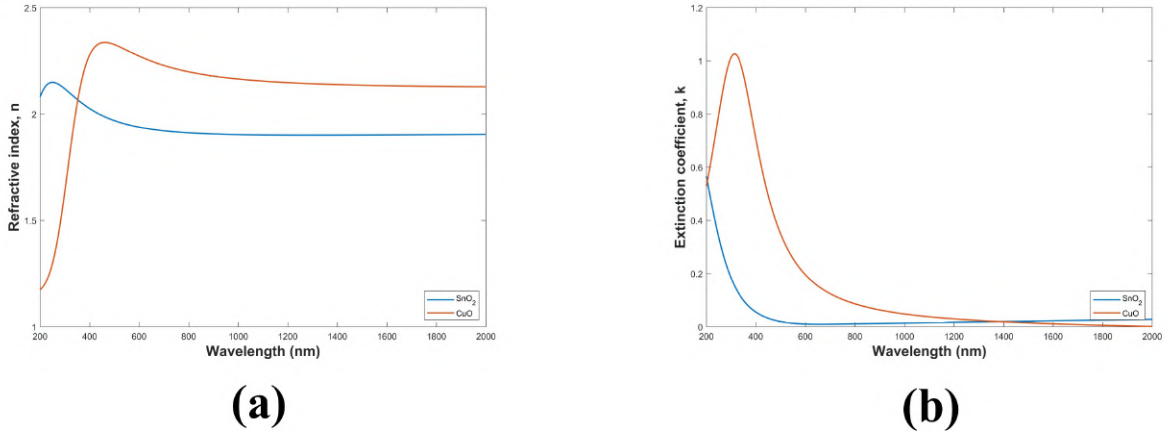

Figure 4-1.: Ellipsometry results for SnO_2 and CuO thin films: **(a)** refractive index (n), and **(b)** extinction coefficient (k).

The SnO_2 and CuO targets were chosen since they exhibit a refractive index contrast close to 0.233 at the near infrared region (1.902 for SnO_2 and 2.134 for CuO at 1550 nm). Additionally, both media has low extinction coefficient values, about 10^{-2}. Nevertheless, it was experimentally observed that the optical properties of the deposited films may vary depending on variables of the sputtering processes, such as the initial vacuum pressure, the deposition pressure or the distance between the target and the fiber. Therefore, it was possible to adjust the extinction coefficient value from the experimental spectra, as will be shown later.

As an example, a simple surface waves case was analyzed, which consists of a 10 mm long D-shaped fiber coated with a single SnO_2 thin layer. Here, the deposition pressures were optimized to minimize the extinction coefficient of the thin layer. Figure **4-2a**, shows the experimental spectrum obtained. It can be seen that the spectrum has an asymmetric profile, where its right broadside shows a clean fall, but its left broadside exhibits multiple peaks. This spectrum feature is related to the excitation of multiple BSW modes in the structure [121], the fundamental mode (BSW1) and the superior order modes (BSW2, BSW3, etc). Higher order resonances are excited at shorter wavelengths, resulting in asymmetric spectra, such as the one obtained. *FIMMWAVE* was used to reproduce the obtained experimental results, where the layer thickness was estimated as 89 nm, and its extinction coefficient as 0.001. The calculated spectrum is shown in figure **4-2b**.

Figure **4-3** complements the analysis, by showing the dispersion curves of the core mode and the BSW modes. It can be seen that the dispersion lines of each mode intersect with the dispersion line of the fiber core, which establishes each mode resonance wavelength. Additionally, the main peak in figure **4-3** is composed by the superposition of the first

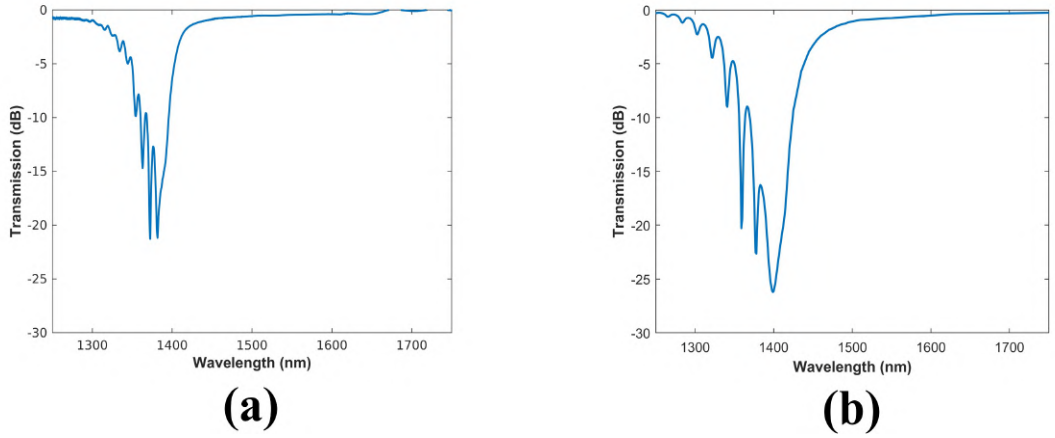

Figure 4-2.: BSW resonances on a D-shaped fiber optic coated with a SnO_2 thin film: **(a)** experimental and **(b)** calculated spectra.

four resonances (BSW 1-4), since their resonance wavelengths are very close. However, the following resonance peaks (BSW5 and higher) can be identified by the crossing point of their dispersion lines with the core-guided-mode dispersion line.

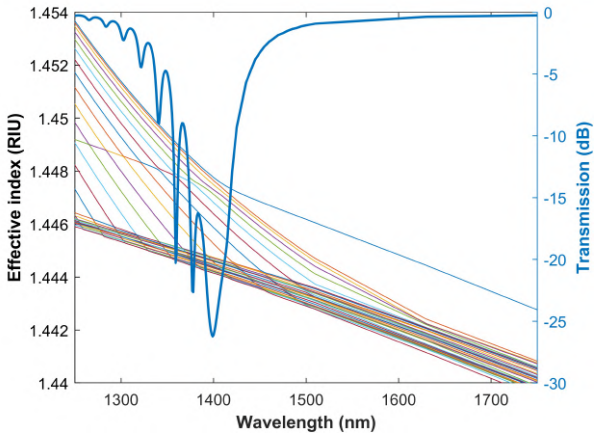

Figure 4-3.: Transmission spectrum and dispersion curves of the BSW resonances in a SnO_2 thin film.

The differences between the experimental and calculated spectra are due to the fact that the optical properties of the deposited film are not known with high precision. However, both spectra correspond well enough to understand the phenomenon and establish that the multiple resonances of BSWs exist and can be excited. Besides, it was verified that metallic oxide thin films with a small extinction coefficient can be deposited with the available equipment.

4.2. Design of the 1DPC

Considering the low refractive index contrast between the SnO_2 and CuO thin films, the thickness of the 1DPC layers must be large enough to ensure that one of the photonic band gaps takes place within the "measurable"near-infrared range, between 1150-1750 nm. Notwithstanding, it is important to consider that the metallic oxide targets may suffer significant wear when the deposition times are very large. Therefore, it was required to search for the minimum thicknesses for each layer that ensures a photonic band gap of the 1DPC in the measurable wavelength range. To find the optimal thicknesses of the 1DPC layers, we used the *Photonic band gap* tool, shown in Appendix A. Figure **4-4** shows the band diagrams for a SnO_2/CuO 1DPC, with layer thickness of 300 nm and 200 nm, respectively. It can be seen that both polarization have a forbidden band at the interest wavelength range. However, as the forbidden band for TE polarization is wider, it will make easier to build a structure to excite TE-BSWs.

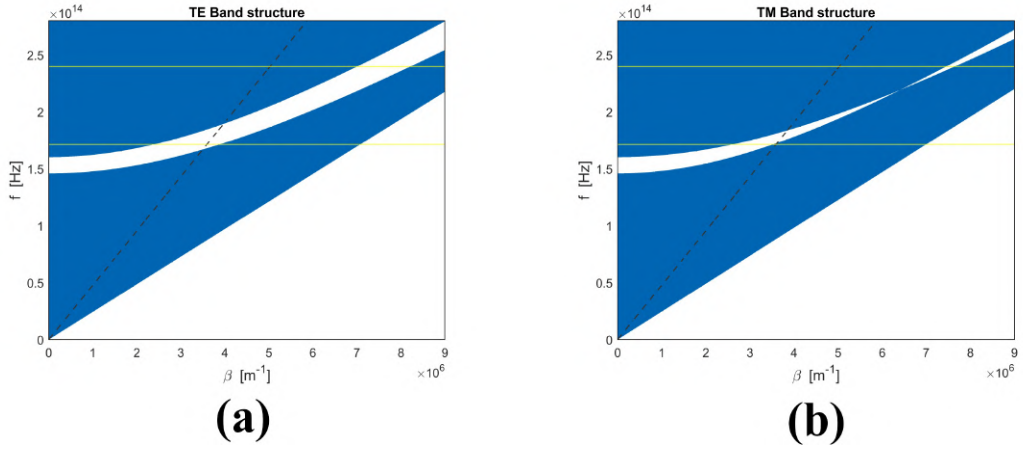

Figure 4-4.: SnO_2/CuO 1DPC band diagram for the **(a)** TE and **(b)** TM polarization. Black dashed lines are the light in the air and yellow lines delimits the measurable wavelengths range.

The transmission spectra of the D-shaped fibers coated with a SnO_2/CuO 1DPC structure were calculated using *FIMMWAVE*. Results are presented in figure **4-5** for 1DPC of 3, 4, 5 and 6 layers. From the figure, we can argue that the 4 layers structure is not optimal for exciting Bloch waves in the selected spectral region, although, as will be shown later, it was possible to make measurements with it. On the other hand, the 3, 5 and 6 multi-layer structures present two distinguishable resonances that correspond to the TE and TM polarization resonances. We were not expecting to observe TM resonances since the narrowness of the prohibited band, showed in the band diagram, will make its excitation difficult.

Computational tools were used to clarify the difference between the TE and TM modes. As

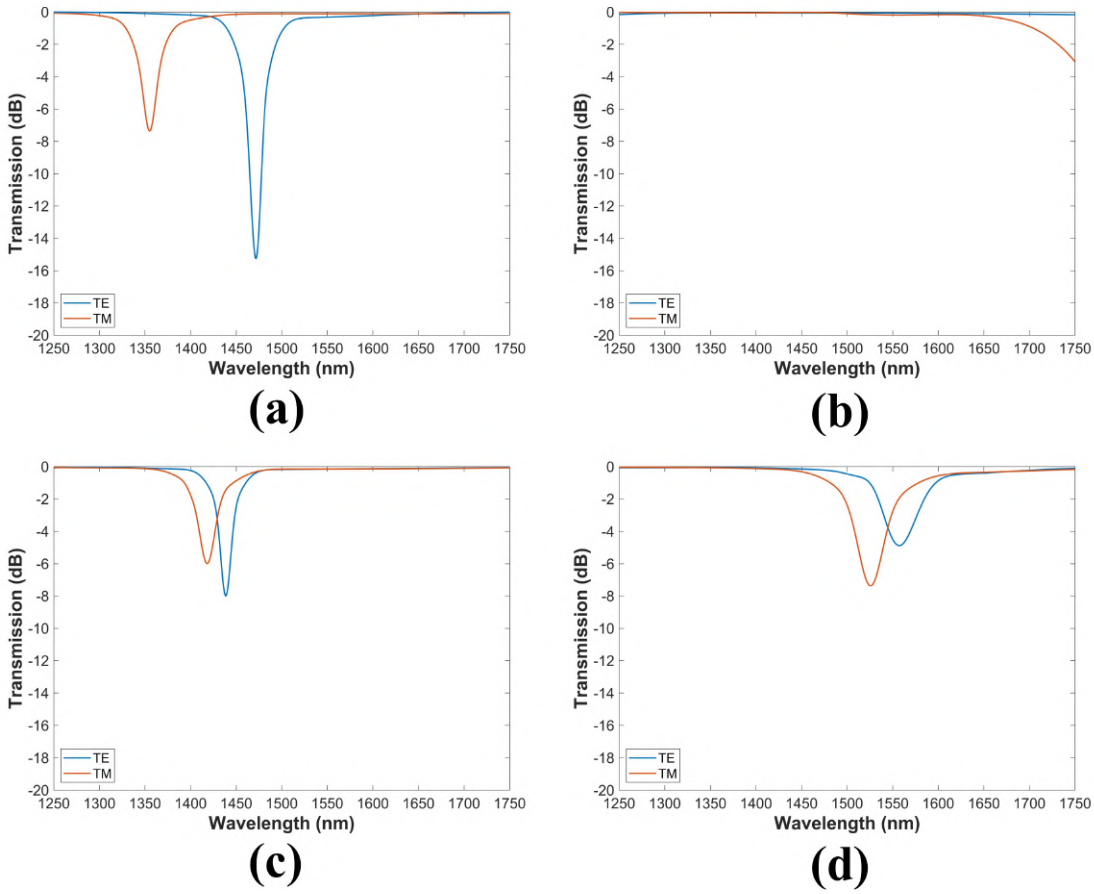

Figure 4-5.: Calculated transmission spectra for the TM and TE polarization for D-shaped coated fiber in air. Each 1DPC has: **(a)** 3-layers, **(b)** 4-layers, **(c)** 5-layers and, **(d)** 6-layers.

an example, the electric field distribution of the 6-layer structure was analyzed in *COMSOL Multiphysics*, and the TE and TM surface modes are presented in figure **4-6**. The electric field amplitude is normalized and the color scale goes from the red areas that represent the maximum electric field intensity zones, to the blue areas where it is zero. The same color scale is used in all the posterior electric field distribution figures. In addition, figure **4-7** shows the profile of the electric field intensity at the center of the fiber for the 3-, 4-, 5-, and 6-layer 1DPC. The figures show that only the TE modes can confine the light at the top layer. On the other hand, TM modes cannot confine the light, and they propagate through the photonic crystal. The electric field distribution of the TE resonances correspond to the expected for the Bloch waves, which are commensurate with the periodicity and symmetry of the 1DPC [122]. On the other hand, the electric field distribution of the TM modes does not correspond to Bloch waves. TM modes exist because the light has a tendency to travel through the higher refractive index media. In this case, the average refractive index is higher in the photonic crystal than in the optical fiber.

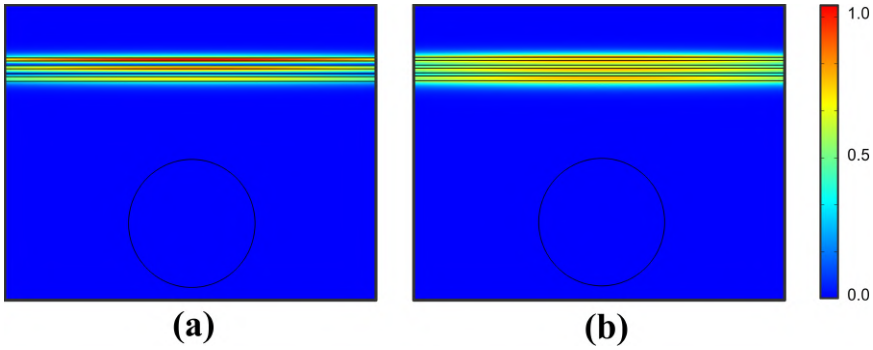

Figure 4-6.: Normalized amplitude of the electric field distribution for the **(a)** TE- and the **(b)** TM-modes excited on the 1DPC coated fiber.

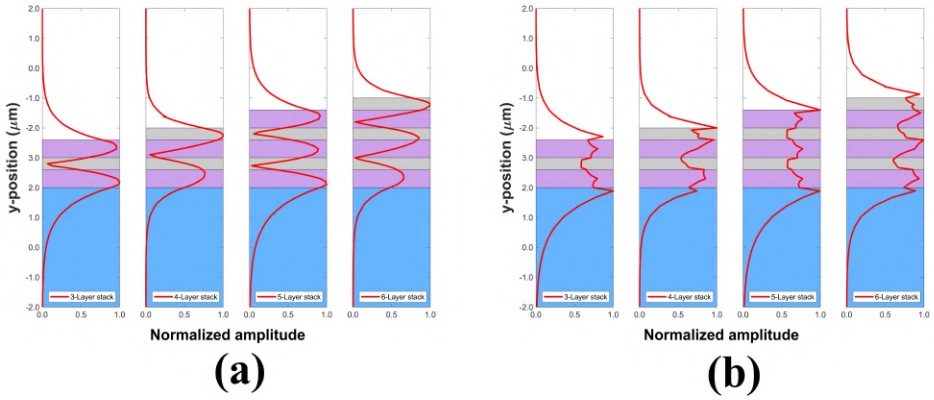

Figure 4-7.: Electric field profile of the **(a)** TE- and the **(b)** TM-modes excited on the 1DPC coated fiber.

In addition, the power confinement difference between a TE and TM modes in the 1DPC coated fiber was analyzed through the calculation of the effective area of the modes [123], defined as [124]:

$$A_{eff} = \frac{\left(\int\int |E|^2 \, \mathrm{d}x\mathrm{d}y\right)^2}{\int\int |E|^4 \, \mathrm{d}x\mathrm{d}y} \tag{4-1}$$

The results are shown in Table **4-1**, where it is confirmed that in all cases the TE resonances have a greater capacity to confine the light, compared to the TM resonances. Finally, the tendency to increase the effective area increases at a higher rate for TM resonances, which confirms that these waves are not confined in the 1DPC, unlike TE resonances.

Table 4-1.: Effective area analysis of the TE- and TM-modes excited on the 1DPC coated fiber.

Layers	Effective Area (μm^2)	
	TE	TM
3	16.50	35.11
4	26.26	38.96
5	25.53	46.55
6	34.43	51.70
7	33.01	58.79
8	36.70	64.42

4.3. 1DPC deposition on D-shaped optical fibers

During the thin film depositions of SnO_2 and CuO, the initial vacuum pressure was established as $P_i = 3 \times 10^{-4}$ $mbar$ and the deposition pressure as $P_d = 6 \times 10^{-2}$ $mbar$. The deposition process was carried out in short time intervals and was monitored in real-time by following the spectral position of each resonance in the transmission spectra. The setup schematic (shown in figure **4-8**) uses a broad-spectrum source consisting of four sleds distributed between 1150-1650 nm. The light source is connected to a linear polarizer and then to a polarization controller. The polarized light passes to the D-shaped fiber, which is located inside the sputter coater system, and the output is connected to an optical spectrum analyzer (OSA). The use of the polarization controller allows selecting each polarization to differentiate between the excited TE and TM modes.

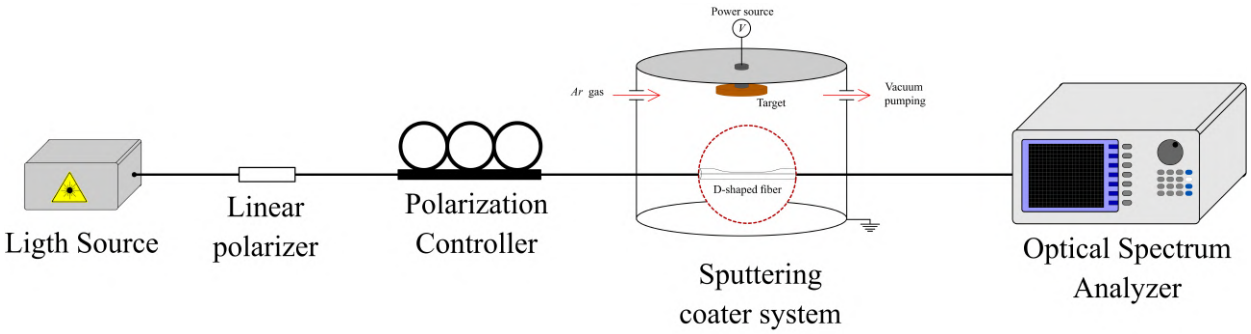

Figure 4-8.: Sputtering system setup

The sputter coater system allows working with two targets and alternately depositing one and the other. To use this functionality, the D-shaped fiber had to be located approximately in the center of the vacuum chamber. This was needed to ensure that both materials are deposited over the fiber having similar deposition rates. As shown in figure **4-9**, several

locations of the D-shaped fiber were tested inside the sputtering machine. However, since the fiber was further away from the target, the deposition times increase up to six times. Finally, the multitarget function could not be used since such long deposition times wear the target faster, compared to a standard use of it.

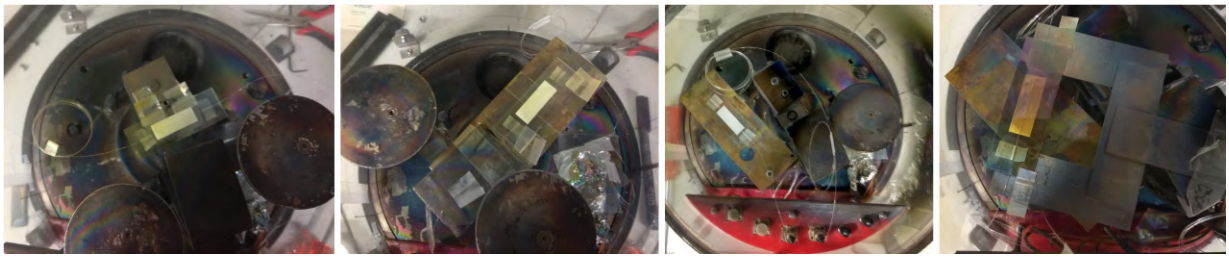

Figure 4-9.: Some positions of the D-shaped fiber inside the sputtering coater system, which were tested during the 1DPC deposition.

Therefore, it was decided to fix the position of the optical fiber and change the target after depositing each layer of the 1DPC. The established working protocol was actually slow, since the entire process of depositing each layer takes approximately two hours, mainly because of the required time to reach the initial vacuum pressure. Notwithstanding, excessive wear of the targets was avoided. Figure **4-10** shows the sputtering coater system **(a)** and a coated D-shaped fiber **(b)**.

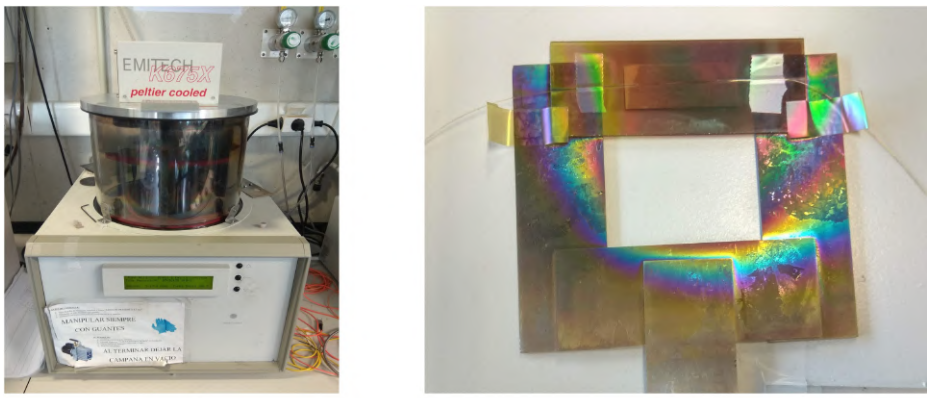

Figure 4-10.: Experimental setup: **(a)** Sputtering coater system and **(b)** D-shaped coated fiber.

To study the resonances excited in the fiber, the experimental transmission spectra were taken with the D-shaped fiber immersed in water (refractive index 1.33). The experimental and calculated spectra of the 3-layer stack coated fiber is presented in figure **4-11**. Two resonances are observed in both spectra, corresponding to the TE and TM polarization. The experimental transmission peaks are wider than the calculated ones, although its spectral

position corresponds to the simulation results. The peak spectral widening can be attributed to the possible irregularities generated during the deposition process. In addition, it is quite possible that the imaginary part of the refractive index of the coating layers is different than expected.

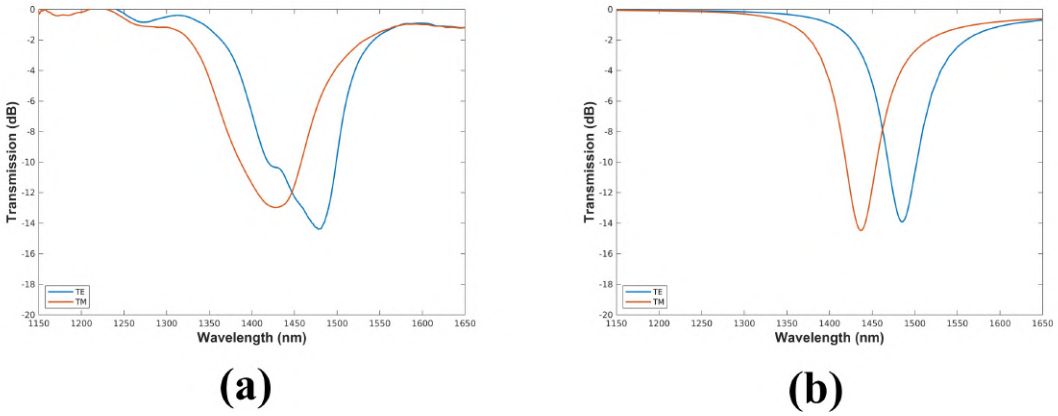

Figure 4-11.: Transmission spectra of the D-shaped fiber coated with the 3-layer stack. **(a)** Experimental and **(b)** calculated spectra.

On the other hand, figure **4-12** shows the experimental and calculated spectra of the fiber coated with the 4-layer stack in water. The calculated spectrum in figure **4-5 (b)** shows that when the fiber is on air, there are no resonances in the analyzed region. However, when the fiber is immersed in water the TM and TE resonances shift to the right side of the electromagnetic spectrum resulting in the transmission spectra shown in figure **4-12**. However, the shallow depth of these resonances, in addition to their large spectral width, increase the requirement to perform measurements using this structure.

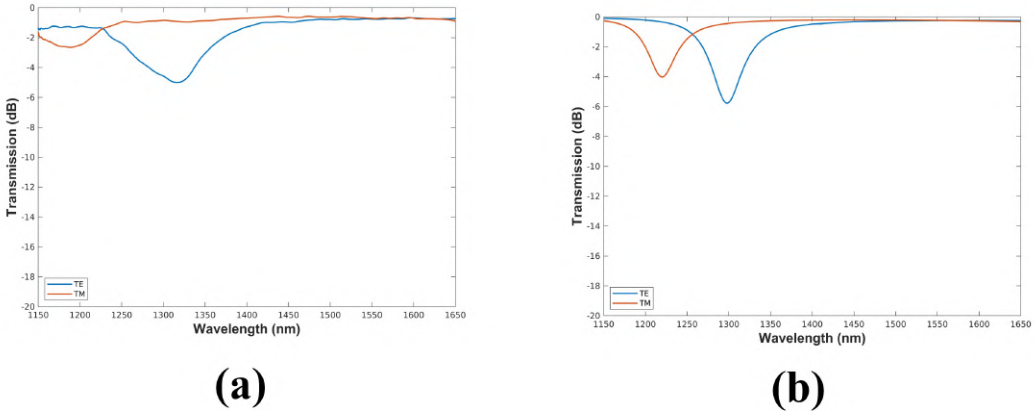

Figure 4-12.: Transmission spectra of the D-shaped fiber coated with the 4-layer stack. **(a)** Experimental and **(b)** calculated spectra.

Finally, the experimental and calculated spectra corresponding to the D-shaped fibers coated with the 5- and 6-layer stacks (immersed in water) are shown in figures **4-13** and **4-14**, respectively. As expected, TE and TM resonances are excited in both structures. It is important to note that as more layers are deposited, the 1DPC band gap gains relevance, and the spectral width of the TE resonances has a tendency to be increasingly narrow. In addition, in these cases, the resonances for both polarization are close enough to consider omitting the use of light polarizers to simplify the experimental setup. This alternative will be analyzed in the next section.

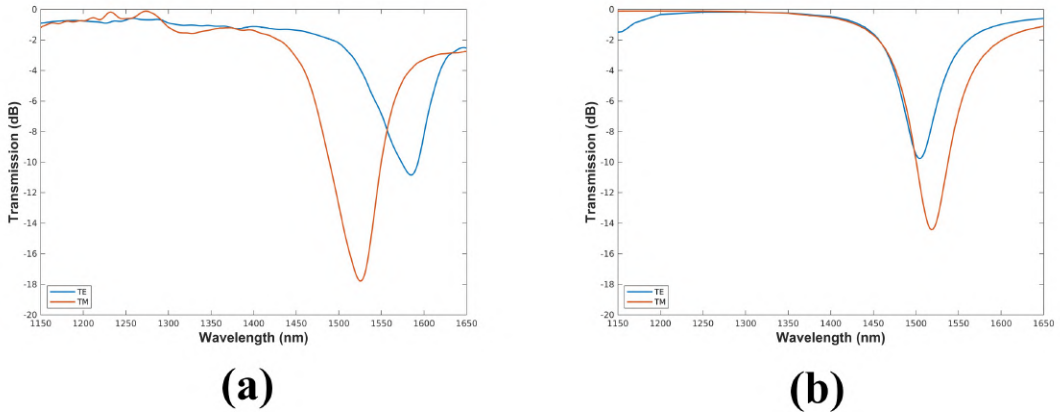

Figure 4-13.: Transmission spectra of the D-shaped fiber coated with the 5-layer stack. **(a)** Experimental and **(b)** calculated spectra.

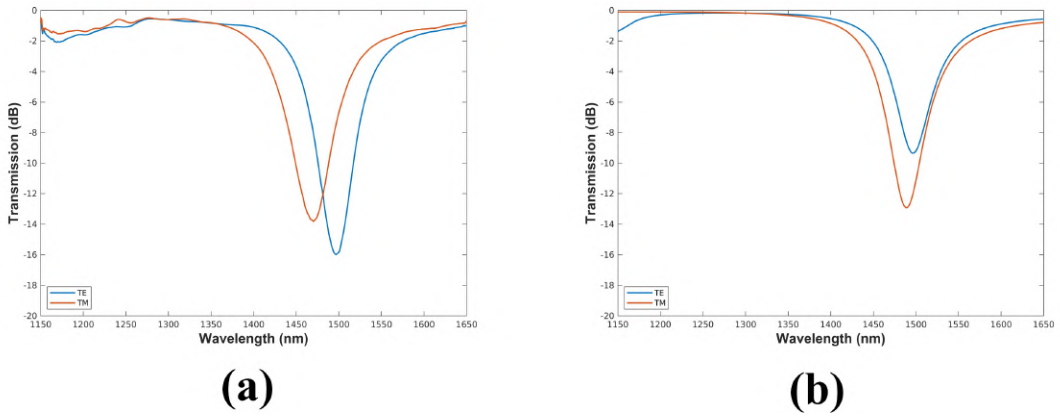

Figure 4-14.: Transmission spectra of the D-shaped fiber coated with the 6-layer stack. **(a)** Experimental and **(b)** calculated spectra.

4.4. Sensitivity analysis of the 1DPC

Among the most widespread applications based on BSW excitation is refractometry, therefore, the D-shaped fibers with deposited multi-layers were used to perform refractive index measurements of aqueous solutions. Nine glycerol-water solutions were prepared at different concentrations to measure the response of each 1DPC in the refractive index range of 1.33 to 1.41. Between each measurement, the fiber had to be cleaned with plenty of water since glycerol tends to adhere to the fiber surface. This was a necessary action to ensure that, after each measuring, all resonance peaks return to its original position and the following measures are not distorted. The refractive index measurement proceeding was performed twice for each fiber. The first time, the response of the TE and TM resonances was analyzed, and the second time the response of the structure to unpolarized light was analyzed. Wavelength shift results for the four deposited structures are shown in Figure **4-15** (all graphs are in the same scale to simplify its interpretation). Finally, the device sensitivity is defined as $S_n = \partial\lambda_{res}/\partial n_A$, where λ_{res} is given in nm and n_A in refractive index units (RIU). The sensitivity results are shown in table **4-2**.

The wavelength shift analysis shows that as more layers are deposited on the D-shaped fiber both resonances reduced their sensitivity. That implies that the excited modes have a strong component of the electric field linked to the 1DPC structure. It is important to highlight that in this structure the TE-BSW modes have lower sensitivity than the TM modes. This happens because the BSW modes are strongly linked to the photonic crystal and most of its electric field is confined inside the SnO_2 layers. On the contrary, the excited TM modes can freely propagate through the photonic crystal without any strong link with it. Since the 1DPC has few layers, the TM modes interact easier with the substrate and the external environment.

Table 4-2.: Sensitivity analysis of the D-shaped fibers with 1DPC.

Layers	**TE modes** (nm/RIU)	**TM modes** (nm/RIU)	**Unpolarized light** (nm/RIU)
3	501.9	1300.8	1000.1
4	114.3	531.4	-
5	512.5	819.2	805.7
6	419.8	720.4	557.3

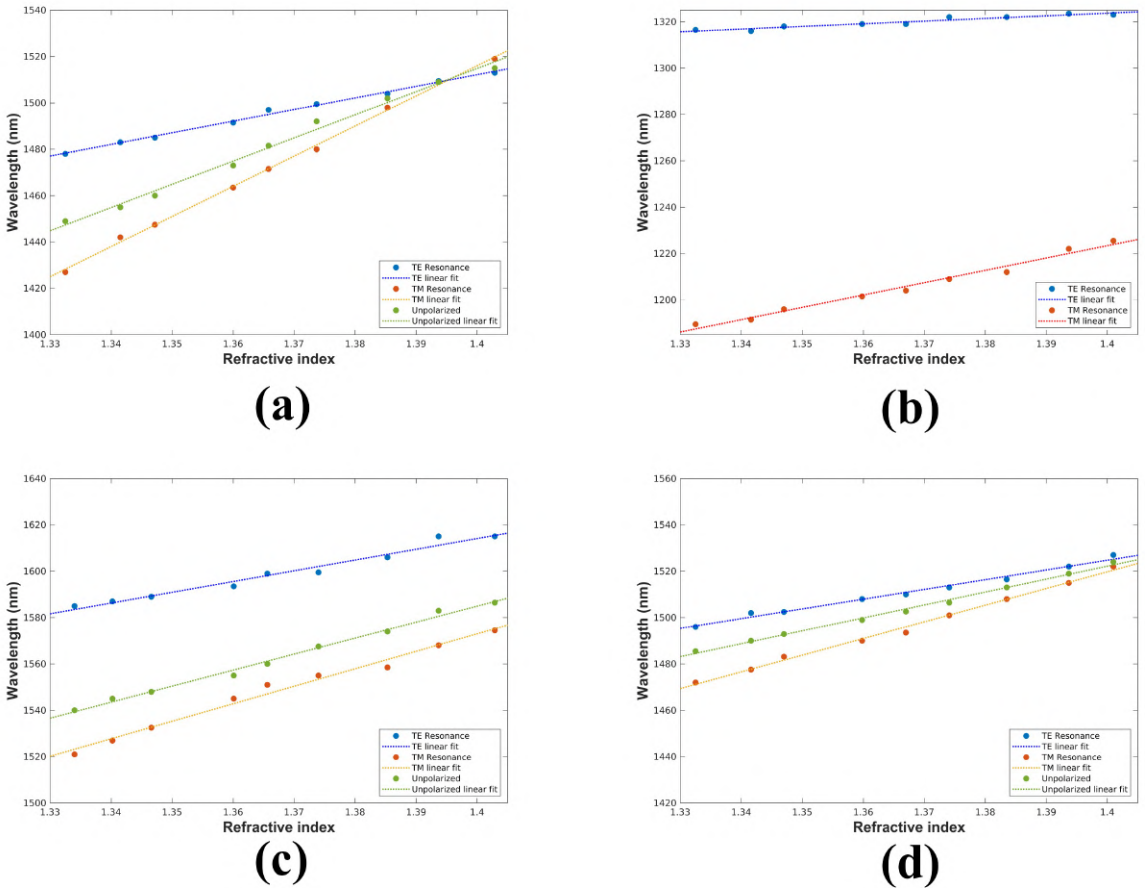

Figure 4-15.: Wavelength shift analysis of the **(a)** 3-layer, **(b)** 4-layer, **(c)** 5-layer and, **(d)** 6-layer 1DPC. The blue, red and green lines represents the measurements for TE polarization, TM polarization and unpolarized light, respectively.

4.5. Summary

In summary, this chapter addressed the design and construction of a photonic crystal on the flat surface of a D-shaped fiber, and the refractometric performance of the structure for several numbers of layers of the 1DPC. It was possible to verify that the excited modes in the structure are susceptible to changes in the refractive index of the external medium, however, the sensitivity decreases as more layers are added to the fiber. This was expected since, as evidenced in figure **4-7**, the more layers the structure has, the electric field of the excited modes is more distributed throughout the photonic crystal. It was considered that the loss of sensitivity would be compensated by a narrowing of the resonance peaks, however, in our results, it was barely evident. It was caused by the two optical characteristics of the deposited films. First, as the refractive index contrast between the two media in the 1DPC is low, the forbidden bands are quite narrow, which makes difficult that the deposited photonic crystal

has the desired characteristics. On the other hand, we can affirm that the imaginary part of the deposited films is relatively high since the multiple peaks —corresponding to the higher-order BSW modes— were not observed in the transmission spectra. It was verified from the simulation results since it was necessary to define 0.01 and 0.02 as the imaginary part of the SnO_2 and the CuO thin layers, respectively. That allowed us to adjust the calculated and experimental spectra.

Finally, we can conclude that it was possible to carry out the first experimental verification of BSWs in D-shaped optical fibers, where the surface waves excitation was made through the evanescent field of the core-guided light. In addition, the viability of the proposed structure as a refractive index sensor was demonstrated. Notwithstanding, we propose to continue with the investigation and adjust the number and optical properties of the materials that form the photonic crystal, in order to achieve narrower resonances, which improve the device figure-of-merit.

5. Bloch surface waves in photonic crystal fibers

5.1. BSWs in multilayer dielectric coated PCF

The content of this section is the result of the peer-reviewed contribution "*Bloch surface wave resonance in photonic crystal fibers: towards ultra-wide range refractive index sensors*" [121], published on April of 2019.

5.1.1. Structure and numerical modeling

1D photonic crystal

We consider a planar 1DPC because the principal region of BSW excitation is the central region of a PCF, which can be approximated as a planar section of the fiber. In this work, the dielectric multilayer structure was designed to sustain BSW modes in the near infrared, which is the common range of operating wavelengths in fiber-optic communication components. The designed 1DPC is shown in figure **5-1**(a) where SiO_2 is used as a substrate. The 1DPC consists of a 4-period stack made of TiO_2 (high-refractive index) and SiO_2 (low-refractive index) layers whose thickness are $d_h = 250\ nm$ and $d_l = 600\ nm$, respectively, and period $\Lambda = d_h + d_l$. As it was mentioned above, the top layer, which will be in contact with the external environment, breaks the 1DPC periodicity, for which a TiO_2 layer of $d = 160\ nm$ thick was initially considered.

Figures **5-1**(b) and **5-1**(c) show the band diagrams of the periodic TiO_2/SiO_2 dielectric structure for the TM- and TE-polarized modes, respectively. The numerical simulations were carried out by means of the transfer matrix method [51]. The diagram's white regions represent the 1DPC forbidden bands, while the dashed lines are the dispersion relations for light propagating in air; $f = \beta c/2\pi$, where β is the propagation constant and c is the speed

of light in vacuum. Dispersion curves for the TM- and TE-polarized BSWs are the green and red lines, respectively, which were calculated by computing the fundamental BSW1, as it will be shown later. As expected, the dispersion curves of the BSW modes are located inside the 1DPC forbidden bands (white regions) and below the analyte light line. The band diagrams show that TE- and TM-polarized BSWs can be excited at near-infrared wavelengths (see the highlighted spectral region in figure **5-1**). However, it is worth mentioning that the dielectric 1DPC can be designed appropriately so that it is possible to excite BSWs at any designable wavelength.

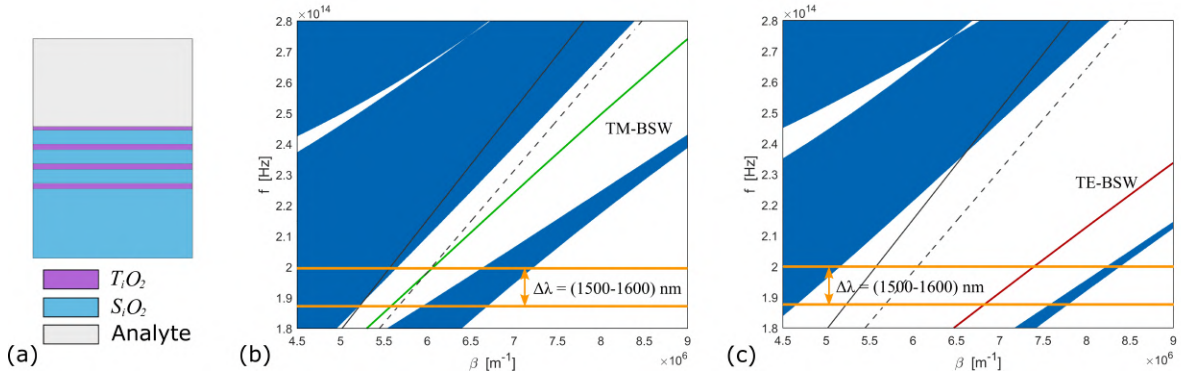

Figure 5-1.: **(a)** Designed 1DPC structure. Band diagrams for **(b)** TM polarization and **(c)** TE polarization. In the band diagrams: white regions are the forbidden bands, the solid and discontinuous black lines are, respectively, the light in the analyte and the substrate, the green and red lines are the calculated TM- and TE-polarized BSW dispersion curves, respectively, and orange lines highlight the spectral region of interest ($\Delta\lambda$ = 1500-1600 nm). For the analysis, the analyte refractive index was assumed as $n_A = 1.33$.

Photonic crystal fiber

We consider a *Ge*-doped suspended-core three-hole silica PCF, which has been successfully fabricated using the stack and draw technique [125]. This PCF can have exposed regions of the fiber core —often referred to as side-opened suspended-core PCF— to accelerate the fluid filling and access the fiber core and thus achieve real-time sensing [126]. Additionally, using this PCF is possible to design a multi-analyte sensor [86], a topic that will be addressed in subsequent investigations. The dielectric layers of the designed 1DPC can be deposited on the inner surface of one (or more) hole of the PCF by using high-pressure chemical vapor deposition (HPCVD). Uniform dielectric thin films have been reported inside PCF holes using HPCVD technology, with barely 2 % thickness variation [127]. Figure **5-2** shows the cross-section of the PCF and the inset is a zoom of the fiber central region, where it can be identified that the 1DPC is only deposited inside channel 1 (CH1). As we can see in this

figure, CH1 is considered to contain analyte, while channels CH2 and CH3 are filled with air. The bridge thickness is $a = 2\ \mu m$, the core diameter is $2\ \mu m$, the minimum distance between the core and the holes is $b = 2\ \mu m$, and the bridge curvature radius is $r = 11.93\ \mu m$.

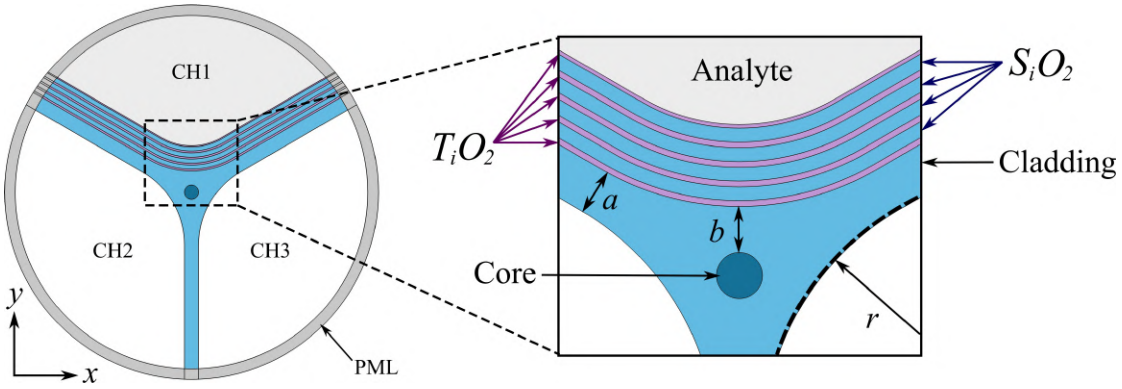

Figure 5-2.: Schematic of the *Ge*-doped suspended-core silica PCF with a TiO_2/SiO_2 4-period multilayer structure designed to sustain Bloch surface wave modes.

In order to calculate the propagating modes in the structure, the vector wave equation was solved using *COMSOL Multiphysics* finite element software, where a perfectly matched layer (PML) was added to avoid reflections at the boundaries. Silica and titanium oxide refractive indexes were calculated using Sellmeier equation with coefficients reported in [128], and the fiber core refractive index was calculated using coefficients reported in [129] for 4 % *Ge*-doped silica.

It has been theoretically and experimentally demonstrated that surface waves, such as SPPs, can be excited and coupled from the fiber core modes [8]. The guided light in the core generates an evanescent field that can excite an SPP wave at the resonant wavelength. The same analysis can be applied for the case of resonance between a core-guided mode and a Bloch wave in the dielectric 1DPC. Now, the evanescent field of the y-polarized core mode excites the TM-polarized BSW modes while the evanescent field of the x-polarized core mode excites the TE-polarized BSW modes. Figure **5-3** shows the electric field distributions of the core-guided mode and the fundamental TM- and TE-polarized surface modes. The insets present the electric-field distributions of surface waves along the 1DPC in the fiber central region (white dashed line), which, as expected, the BSW field decays exponentially in the 1DPC and in the homogeneous external medium due to Bragg reflection and total internal reflection (TIR), respectively [51, 130].

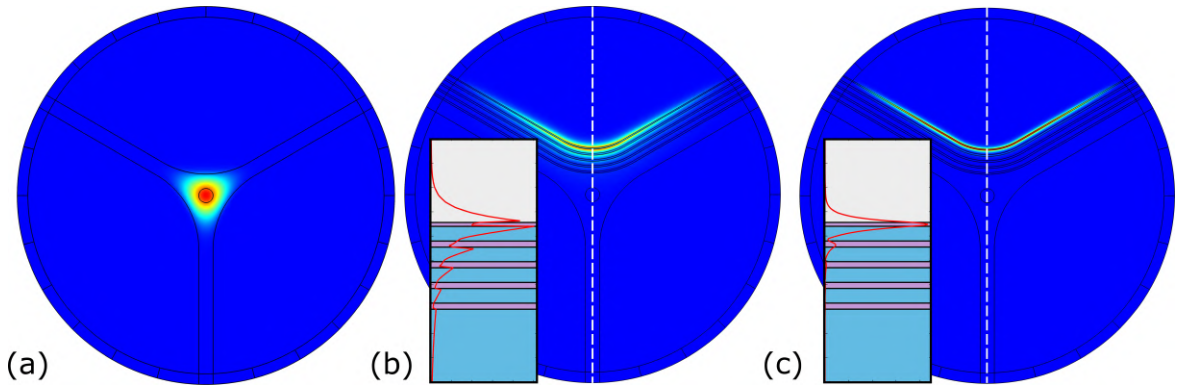

Figure 5-3.: Electric field distribution in the PCF with 1DPC: **(a)** core-guided mode, **(b)** TM-polarized BSW mode and **(c)** TE-polarized BSW mode. The insets present the electric-field of the Bloch waves along the 1DPC in the fiber central region. In general, for this structure, the TM-polarized BSWs have an evanescent tail that significantly penetrates the homogeneous external medium and therefore are of greater interest for sensing applications.

5.1.2. BSW excitation

The resonance excitation of BSWs can be studied by analyzing the dispersion curves of the propagating modes in the structure of the PCF, represented by the dotted curves in figure **5-4** for the TM- and TE-polarized BSWs. Resonance is characterized by a peak loss in the transmission spectrum of the core-guided mode, which indicates the largest energy transfer from the core-guided mode to the BSW mode at a particular wavelength, where the effective refractive indexes (n_{eff}) of the core-guided mode and the BSW mode coincide. As expected from the band diagrams of the 1DPC structure in figure **5-1**, the polarization state of the light has a significant effect on the excitation spectrum of the Bloch waves. For instance, in this case for each state of light polarization, four BSW modes supported by the 1DPC are involved in the coupling properties of the designed PCF. In general, the phase-matching conditions for the excitation of the BSWs by the fundamental core-guided mode indicate that the resonance wavelength of a BSW mode of lower order occurs at a longer wavelength than a BSW mode of high order. It can also be seen that the resonance wavelengths of the TM-polarized BSWs are closer to each other than those observed for the TE-polarized BSWs, which has a significant effect on the structure of the attenuation bands in the transmission spectrum of the core-guided mode, as shown later. The insets in figure **5-4** show the electric field distributions of the BSW modes that indicate the nature of the coupling and the transfer of energy from the fundamental core-guided mode to the BSW modes.

Because the confinement losses are very small, the transmission spectra in figure **5-4** were

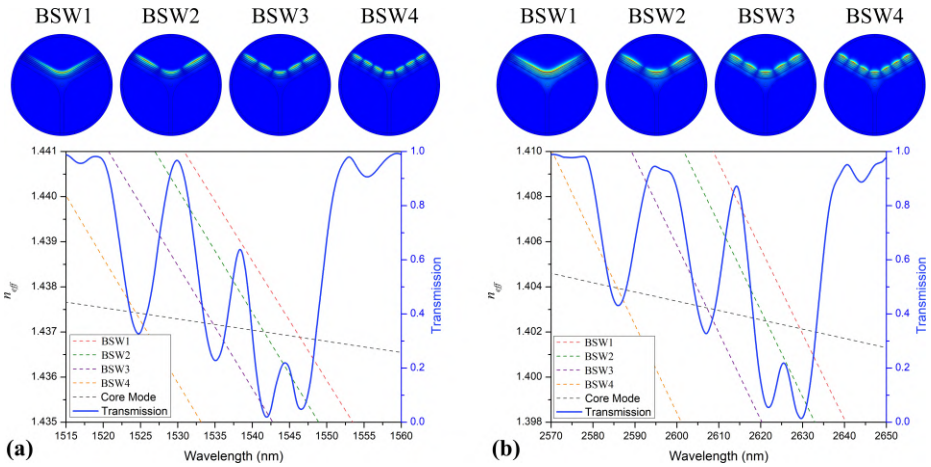

Figure 5-4.: Dispersion curves (dashed lines) of the modes and transmission spectra (blue solid lines) of the designed PCF with the 1DPC in CH1, assuming an analyte medium of $n_A = 1.33$ and a 1DPC length of 1.0 mm and 0.7 mm for the TM- and TE-polarized BSWs, respectively: **(a)** y-polarized core-guided mode excites the TM-polarized BSW modes, **(b)** x-polarized core-guided mode excites the TE-polarized BSW. The insets correspond to the electric-field distributions of the excited TM- and TE-polarized BSW modes in the spectral ranges analyzed.

calculated using coupled mode theory (CMT) [120], assuming an analyte medium of $n_A = 1.33$ and a 1DPC length of 1.0 mm and 0.7 mm for the TM- and TE-polarized BSWs, respectively. As we can see, the computed transmission spectra feature four attenuation bands for the y-polarized core-guided mode in the wavelength range of 1.515-1.560 μm, caused by the Bloch excitations at 1546.4 (BSW1), 1541.6 (BSW2), 1534.8 (BSW3) and 1524.4 nm (BSW4), and four attenuation bands for the x-polarized core-guided mode in the wavelength range of 2.57-2.65 μm, caused by the Bloch excitations at 2629.4 (BSW1), 2621.2 (BSW2), 2607.2, (BSW3) and 2585.8 nm (BSW4). As will be shown below, the difference between the amount of light coupled at each resonance peak is due to the fact that the energy transferred from the fiber core to a BSW mode is a function of the length of the structure, which in this case leads to a higher coupling efficiency for the TM-BSW2 and TE-BSW1 modes.

It is important to note that the resonance wavelength depends on the 1DPC design, especially on the properties of the top layer. Considering TiO_2 as the top layer, the resonance wavelength can be adjusted by choosing the proper thickness of the 1DPC top layer. As an example, figure **5-5** shows the resonant wavelength as a function of the top layer thickness for the fundamental TM- and TE-polarized BSW modes with $n_A = 1.33$. The insets in this figure show the electric field distribution of the BSW1 for different thickness of the top layer. From this figure it is possible to see, at the lower limit, that the resonant wavelength of

the TM-polarized Bloch mode is less sensitive when the thickness of the top layer is below 70 nm, which is explained because the Bloch wave travels inside the stack, so this mode is named as a Bloch sub-surface wave (BSSW) [53, 131]. BSSWs have been used for detection, however it has been shown that if the analyzed substance can not penetrate the multilayer (as the case we are considering) these are less sensitive waves than the BSW [132]. In contrast, the TE-polarized Bloch mode does not show this behavior and it is revealed that as the thickness of the top layer is thinner the BSW mode is more confined and, consequently, the evanescent field component decreases, which it is not favorable for sensing applications.

On the other hand, at the upper limit of figure **5-5**, the TE-polarized Bloch mode reaches the maximum possible when the top layer thickness is greater than 200 nm. In this case, the distribution of the electric field shows that the Bloch mode is extended in the stack and the evanescent field component in the external environment is very small, which means that the BSW1 dispersion curve moves towards the edge of the band gap when the top layer becomes thicker, until it is comparable to the TiO_2 layers in the stack. In contrast, at this upper limit one can see that the TM-polarized Bloch mode still does not reach the maximum possible.

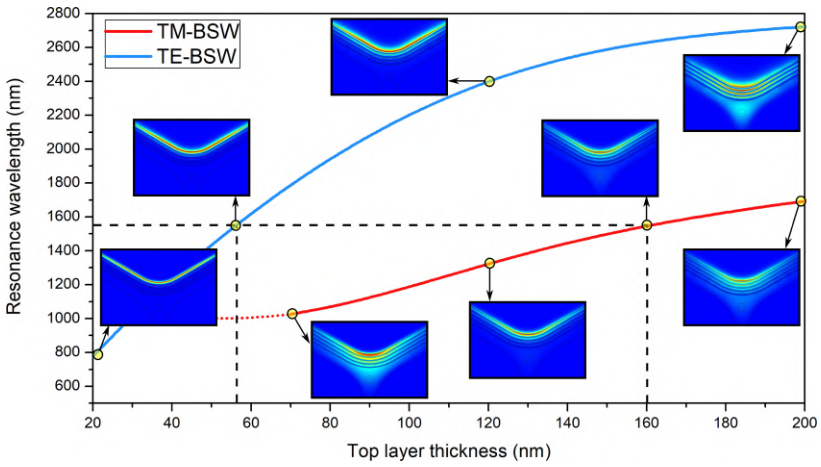

Figure 5-5.: Resonance wavelength of the BSW1 mode as a function of the top layer thickness with $n_A = 1.33$. The blue and red curves represent the TM and TE modes, respectively.

Figure **5-5** further shows that for a given value of top layer thickness, TM- and TE-polarized Bloch waves are excited in very different spectral regions. If it is intended to excite both polarization at the same wavelength, then two structures with different top layer thicknesses should be designed. Finally, it can be concluded that by properly selecting the top layer thickness of the multilayer structure, the Bloch waves can be excited in any desired polarization state over a wide range of wavelengths, from visible to infrared.

5.1.3. Ultra-wide range refractive index sensor

From our simulation results above, we demonstrated that a TiO_2/SiO_2 dielectric 1DPC can be designed in 1550 nm telecom band. Figure **5-5** show that a TE-polarized BSW will be excited when the top layer thickness is 56 nm and a TM-polarized BSW will be excited when the top layer thickness is 160 nm. However, as can be seen in the field distributions in figure **5-5**, at 1550 nm the TE-polarized BSW is very confined in the top layer and, therefore, will have a reduced interaction with the analyte in CH1, which is crucial for the operation of a refractive index sensor. Accordingly, the structure with the top layer thickness of 160 nm was chosen as a refractive index sensing structure with the TM-polarized BSW mode excitation.

In order to evaluate the performance of the three-hole suspended-core PCF-based BSW sensor, an extended range of analyte refractive index, from 1.0 to 1.4, was considered, as shown in figure **5-6** for a 1.5-mm-long sensor. In general, the resonance peaks are very sharp. It can be seen that the four most excited loss peaks move towards longer wavelengths, and the loss of the core-guided mode gradually increases as the analyte refractive index increases. With the increase of the resonance wavelength, the effective refractive index decreases significantly, as a result the refractive index contrast between the core-guided mode and the BSW mode is reduced, which leads to stronger coupling between the core-guided mode and the BSW mode. Considering the wavelength sensitivity, the BSW1 resonance peak is more suitable for refractive index sensing (see yellow dots). In this figure it is clear that higher-order BSW modes are excited close to the BSW1 mode, especially the BSW2 mode, as already observed for the TM-polarized modes, which causes the BSW1 resonance peak to have a non-optimized spectral profile, such as it is shown later. Clearly, the designed sensor can detect analyte refractive index changes in the proposed extended range. This implies that with the analyzed structure, it is possible to have an ultra-wide range sensor with which gases, bio-analytes and liquids with high refractive index can be sensed.

The resonant wavelength shift, with respect to the analyte variation, is shown in figure **5-7**(a), and the sensor sensitivity, defined as $S_n = \partial\lambda_{res}/\partial n_A$, is shown in figure **5-7**(b). It is possible to see that the BSW1 resonant wavelength shift is approximately linear for low values of analyte refractive index ($1.0 < n_A < 1.15$), a trend confirmed by the sensor sensitivity analysis. Nevertheless, for higher analyte refractive index values ($1.15 < n_A < 1.4$), the sensor response and sensibility exhibit a nonlinear feature due, as already explained, to the strong mode coupling between the core-guided mode and the BSW mode. When the analyte refractive index is $n_A = 1.4$, the sensor sensitivity reaches 2575 nm/RIU, which is comparable with most of the PCF-based SPP sensors [8].

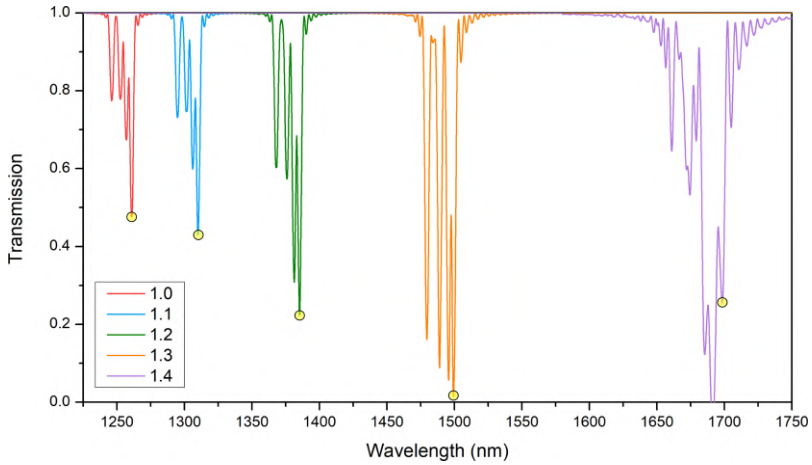

Figure 5-6.: Transmission spectra as a function of the analyte refractive index for a TM-polarized BSW sensing structure based on three-hole suspended-core PCF with a 1DPC length of 1.5 mm.

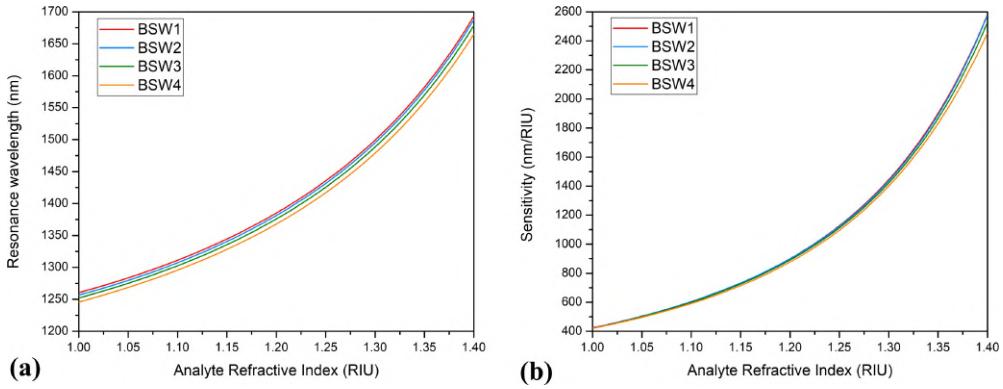

Figure 5-7.: Operation of the TM-polarized BSW sensor based on three-hole suspended-core PCF with a 1DPC length of 1.5 mm in an ultra-wide refractive index range. **(a)** Resonance wavelength shift and **(b)** sensitivity.

In order to obtain the highest efficiency of the PCF-based BSW sensor, its response can be optimized by calculating the transmission curves for different sensor lengths, in order to find the conditions in which the coupling between the core mode and the surface modes is optimum. As an example, in figure **5-8** an optimization process is carried out, where it was assumed an aqueous analyte refractive index ($n_A = 1.33$). The full-width-at-half-maximum (FWHM) analysis of the optimized systems can be found in table **5-1**. It is worth mentioning that larger propagation lengths were not considered, given that a longer sensor will optimize the coupling of higher order modes, and it will not be possible to track the BSW1 resonance peak.

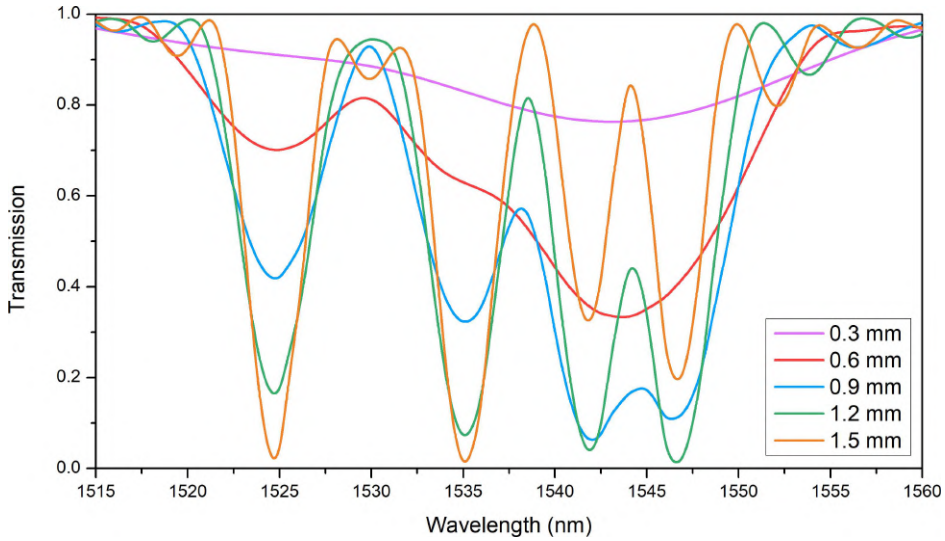

Figure 5-8.: Transmission spectra of the sensing structure for five different sensor lengths.

A more comprehensive description of the sensor response can be given by the figure-of-merit (FOM) analysis of the resonance peak in the transmission spectra, defined as $FOM = S_n/\text{FWHM}$ [8]. The FOM parameter is an important characteristic to evaluate the performance of a resonant sensor. In table **5-1**, it can be seen that the sensor length plays an important role to define the sensor quality, represented here as the FOM parameter.

Table 5-1.: FWHM and FOM analysis of the proposed sensing structure for $n_A = 1.33$. The sensitivity value is $S_n = 1693\ nm/RIU$.

Sensor Length (mm)	**FWHM** (nm)	**Coupled Ligth** (%)	**FOM** (RIU^{-1})
0.50	17.1	53	98.8
0.60	17.0	67	99.7
0.70	17.1	78	98.9
0.80	16.9	87	99.9
0.90	11.1	90	152.5
1.00	10.2	96	166.0
1.10	9.5	99	178.2
1.20	9.3	99	189.0
1.30	3.9	96	430.8
1.40	3.5	89	489.3
1.50	3.1	81	549.7
1.60	2.8	71	611.2
1.70	2.5	50	669.2
1.80	3.5	24	481.0

For short sensor lengths, the BSWs loss peaks overlap due to their band width, however, as the sensor length increases, each of the resonance peaks becomes narrower and can be differentiated. When the sensor length is $L \geq 1.30\ mm$, the FHWM of the BSW1 loss peak is not affected for higher-order resonances, then the sensor FOM substantially increases, reaching a value of 669 RIU^{-1} (see table **5-1**), which is better than a lot of PCF-based SPP sensors [8,133,134]. However, as the sensor FOM increases, the depth of the BSW1 loss peak decreases. Then $L = 1.70\ mm$ can be considered as the optimized sensor length to detect refractive indexes in the vicinity of $n_A = 1.33$.

5.1.4. Conclusion

In summary, this work proposes a electromagnetic surface waves-supporting dielectric multilayer structure deposited inside a PCF, where BSWs can be excited through the evanescent field of the core-guided mode. The presence of an additional dielectric layer on the top of the multilayer enables a direct manipulation of the BSWs. It is shown that the properties of the platform define both the propagation and manipulation properties of the surface modes. To demonstrate the concept of the platform, a refractive index sensor based on BSW resonance in the near infrared is designed that can operate in an ultra-wide range of refractive indexes, from 1.0 to 1.4. The designed PCF sensor achieves a sensitivity comparable to the sensitivity of reported PCF SPR sensors, with an ultrahigh sensing figure-of-merit. The structure of the designed PCF BSW sensor is simple and easy to fabricate. Results are promising for high resolution refractive index sensing.

5.2. BSWs in single-layer dielectric coated PCF

The contents of this section are partial results of the working paper "*Bloch surface waves in single-layer dielectric coating in photonic crystal fibers*".

5.2.1. Structure and numerical modeling

In this work, we propose to use a commercial PCF, which under lateral polishing process could be transformed into a D-shaped PCF. This process has already been done in PCFs, although the polishing quality results have been diverse [135–137]. In particular, we consider the commercial fiber *SC-5.0-1040, NKT Photonics*. The hole period is $\Lambda = 3.10\ \mu m$, the hole diameter is $d = 1.61\ \mu m$ and the core diameter is $d_{co} = 5.0\ \mu m$. The lateral polishing of

the PCF should approach the center of the fiber, leaving two rows of holes between the flat surface and the PCF core. A single dielectric thin layer should be deposited on the resulting flat surface to excite BSWs from the evanescent field of the propagating light in the fiber core. Figure **5-9** shows the schematic of the transverse section of the single-layer dielectric coated D-shaped PCF.

During a previous design stage, the number of rows of holes between the core and the polished surface was studied. We found that, for the chosen fiber, a maximum of two rows of holes must be left. Otherwise, the coupling between the core-guided light and the coating layer is as weak that surface waves cannot be excited. Other complementary studies, allowed us to find that using non-commercial fibers (with a lower filling fraction than commercial PCFs) it is possible to leave more rows of holes between the core and the polished surface. However, the manufacturing cost of the non-commercial PCF becomes a barrier that may difficult future experimental verification.

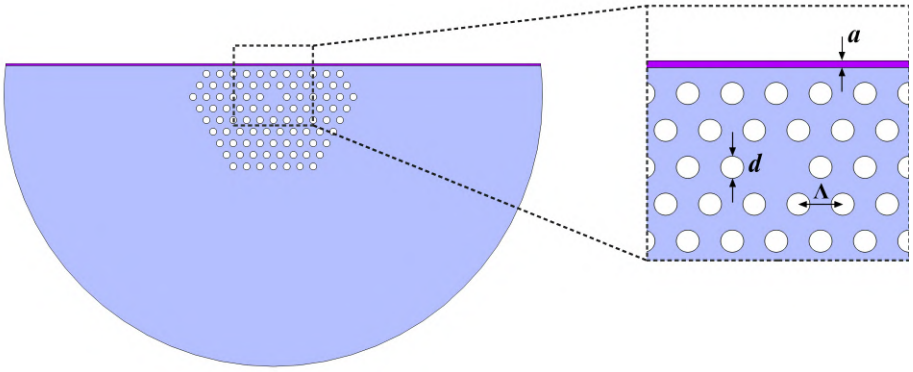

Figure 5-9.: Transverse section of the coated D-shaped PCF. The hole period of the PCF is $\Lambda = 3.10\ \mu m$, their diameter is $d = 1.61\ \mu m$, and a is the top layer thickness.

The proposed structure was analyzed for two different materials of the coating film, tin dioxide (SnO_2) and titanium dioxide (TiO_2). The refractive index (n) and extinction coefficient (k) values of SnO_2 were taken from experimental measurements, as shown in the previous chapter. On the other hand, the TiO_2 refractive index was calculated using the Sellmeier equation (the coefficients were taken from reference [128]), while its extinction coefficient $k_{TiO_2} = 4 \times 10^{-4}$ was taken from the literature [138, 139]. Figure **5-10** shows the refractive index of both materials in the near infrared spectral range.

As an example, the electric field distribution of the first three BSW modes are shown in figure **5-11**, for the **(a)** TE- and **(b)** TM-polarization. All graphics were made at each resonance wavelength, considering a 100 nm thick TiO_2 "top layer", and were plotted without including the fiber core, to spotlight the electric field profile of the BSWs at the same conditions. The electric field distribution of the TE and TM modes show that the guided light penetrates the photonic crystal of the PCF, and the light intensity is evanescent in direction to the external

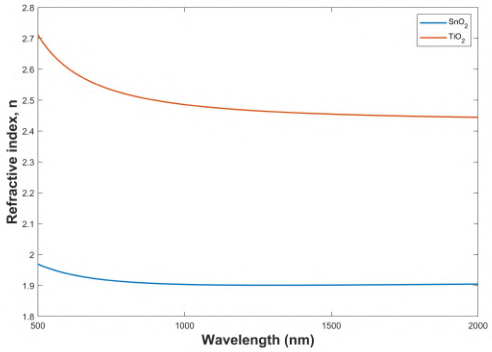

Figure 5-10.: Refractive index of tin dioxide (SnO_2) and titanium dioxide (TiO_2).

medium and to the photonic crystal. Therefore, these modes can be classified as BSWs, since they are excited at the interface between a dielectric medium and a photonic crystal (in this case is two-dimensional), and being confined in the top layer they are evanescent in either of the perpendicular directions.

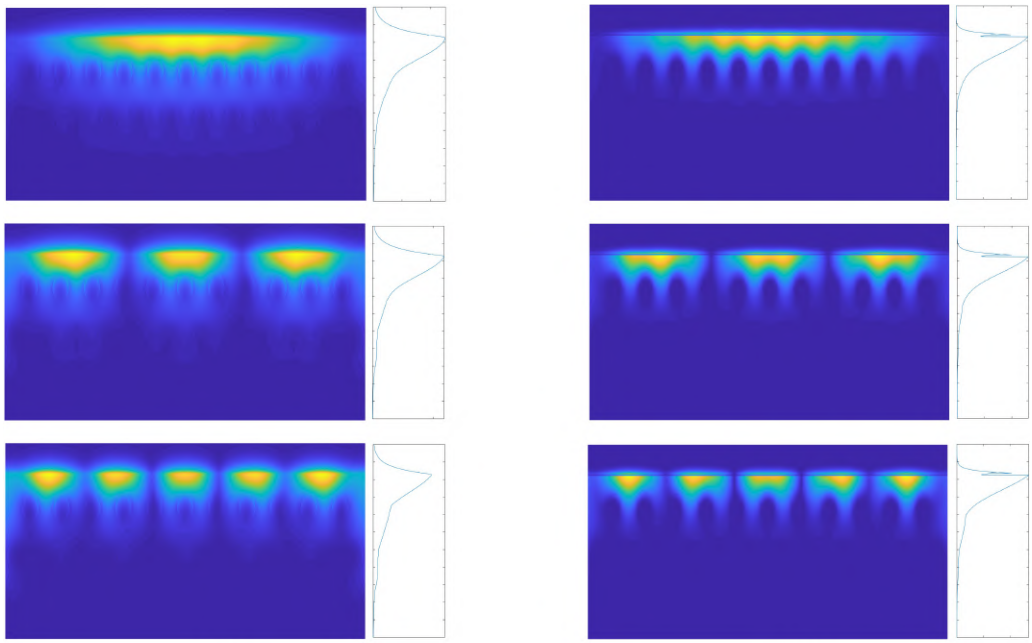

Figure 5-11.: Electric field distribution of the (from top to bottom) BSW1, BSW2 and BSW3 modes, for the **(a)** TE and **(b)** TM polarization.

As previously shown, the resonance wavelength of the BSWs has a strong dependence on the top layer properties. As an example, figure **5-12** presents the resonant wavelength shift of the fundamental TM- and TE-polarized BSW modes, as a function of the top layer thickness. The numerical simulations were made using *FIMMWAVE*, considering a top layer of **(a)**

SnO_2 and **(b)** TiO_2, assuming air as the external medium.

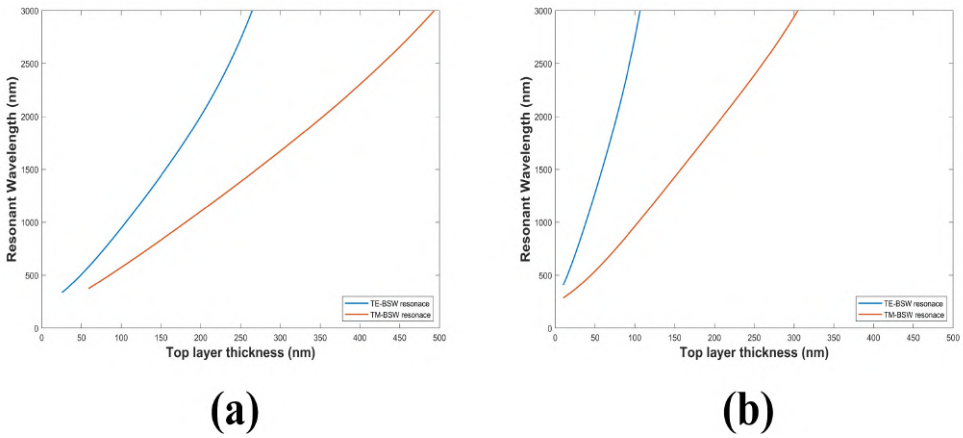

Figure 5-12.: Spectral position of the BSW1 resonance wavelength as a function of the top layer thickness. **(a)** SnO_2 top layer, and **(b)** TiO_2 top layer. The blue and red curves represent the TE and TM modes, respectively.

Figure **5-12** shows that if it is pretended to excite a BSW1 mode at a fixed wavelength, thinner top layers are needed if TiO_2 is used instead of SnO_2. In addition, for the same top layer thickness the BSW modes are excited at longer wavelengths for the TiO_2 films, compared to the SnO_2 films. It was expected because, in the analyzed spectral range, the refractive index is higher for TiO_2 than for SnO_2. Then, it was proposed to analyze the response of the structure for each top layer material, by increasing the refractive index of the external medium. As both polarizations were considered, then two thicknesses have to be chosen for each material. Then, if the fiber has a 131.5 nm thick SnO_2 top layer the TE-BSW1 mode will be excited near 1250 nm. However, if instead the top layer thickness is 227 nm, the excited mode will be the TM-BSW1. Analogously for TiO_2, two thicknesses of 50 nm nm and 134 nm were chosen to find the resonances TE-BSW1 and TM-BSW1 around 1250 nm, respectively.

5.2.2. Single-layer coated D-shaped PCF as a refractive index sensor

In order to evaluate the performance of the single-layer coated D-shaped PCF design as a refractometric sensor, the refractive index of the external media was changed from 1.0 to 1.25. Higher refractive index values were not studied since the BSW resonances move beyond 1750 nm, outside the range of the electromagnetic spectrum where we can measure. Figure **5-13** shows the displacement of the wavelength resonance of the BSW1 modes for both structures and polarizations.

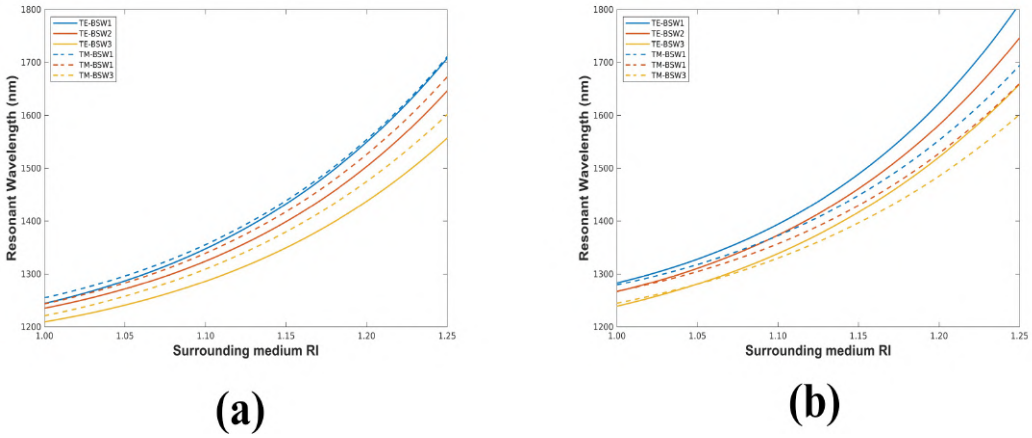

Figure 5-13.: Resonance wavelength shift of the BSW1, BSW2 and BSW3 modes (blue, red and yellow lines, respectively) as a function of surrounding refractive index. **(a)** SnO_2 top layer, and **(b)** TiO_2 top layer. Solid lines represents the TE modes and dashed lines represents the TM modes.

Figure **5-13** shows that in the selected refractive index range, the excited resonances in the TiO_2 top layer have larger resonant wavelength shift than the excited resonances in the SnO_2 top layer. It was expected since the TiO_2 refractive index is much higher than that of SnO_2 ($n_{TiO_2} = 2.45$ and $n_{SnO_2} = 1.85$, at 1500 nm). The analysis of the proposed structures as a refractive index sensor is performed through the calculation of the sensitivity, defined as $S_n = \partial\lambda_{res}/\partial n_{ext}$. Figure **5-14** shows the sensitivity results for both structures, where it can be seen that as expected, the structure with TiO_2 has higher sensitivity, within which the TE-BSW1 resonance stands out.

From the sensitivity analysis, we can conclude that coating the fiber with a TiO_2 top layer is a better option, regardless of the polarization chosen. Notwithstanding, all the analyzed D-shaped PCF configurations have high sensitivity compared to other BSWs-based sensors [121]. As an example, the previously proposed sensing device based on the TM-BSW excitation on a multilayer stack within a suspended core PCF has a sensitivity of 1100 nm/RIU (for $n_A = 1.25$). At the same polarization and external refractive index, the single-layer coated D-shaped PCF has a sensitivity of 4554 nm/RIU and 4085 nm/RIU (for a top layer of SnO_2, and TiO_2, respectively).

Since the four studied configurations have similar sensitivity, it is necessary to establish an additional parameter to choose the optimal design. The FOM analysis provides an additional parameter related to the performance of a sensing system. Since the FOM depends on the FWHM of the resonance peaks, it is needed to calculate the transmission spectra of each BSW resonance. Figures **5-15** and **5-16** show the transmission spectra of the single-layer coated PCF sensing devices as a function of the refractive index of the external medium.

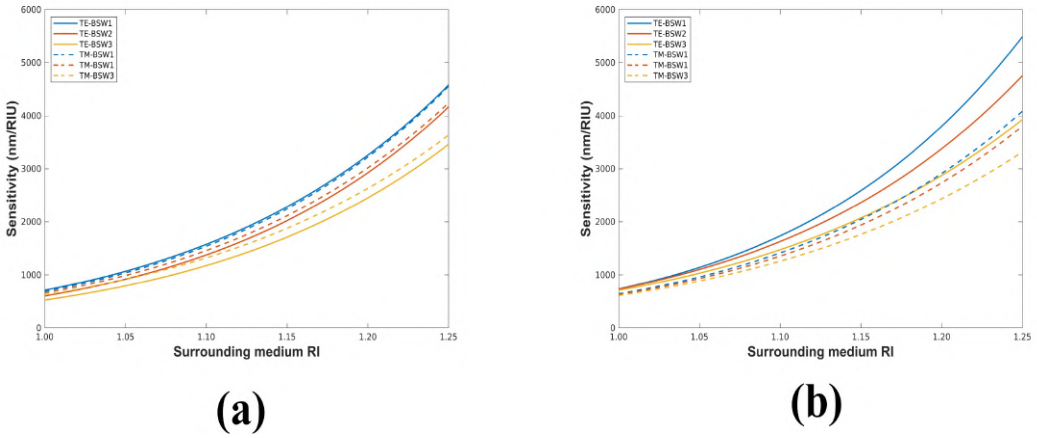

Figure 5-14.: Sensitivity of the BSW1, BSW2 and BSW3 modes (blue, red and yellow lines) as a function of surrounding refractive index. **(a)** SnO_2 top layer, and **(b)** TiO_2 top layer. Solid lines represents the TE modes and dashed lines represents the TM modes.

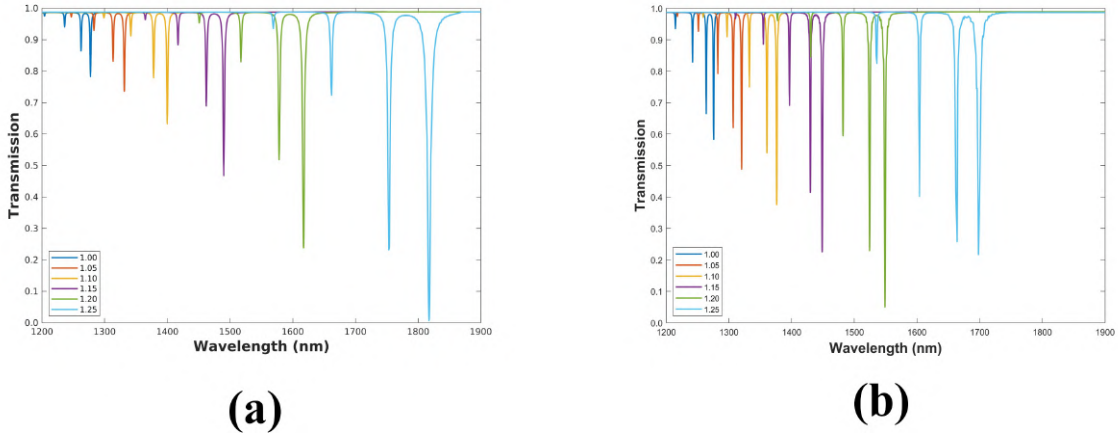

Figure 5-16.: Spectral response of the BSW sensing structure based on a 15 mm long D-shaped PCF coated with a single layer of TiO_2. Transmission spectra for the **(a)** TE- and **(b)** TM-polarized BSWs.

The spectral width of the resonance peaks is strongly related to the refractive index (real and imaginary part) of the coating layer. Then, the obtained transmission spectra with a TiO_2 top layer (figure **5-16**) are deeper and narrower than the obtained with a SnO_2 top layer (figure **5-15**). Consequently, the structures with a TiO_2 top layer present higher values of the FOM parameter. Table **5-2** presents the summary results for the particular case of BSW1 at a external refractive index of $n_{ext} = 1.25$ for TE and TM polarizations.

Table **5-2** shows that the BSW resonances of the D-shaped PCF coated with a SnO_2 top

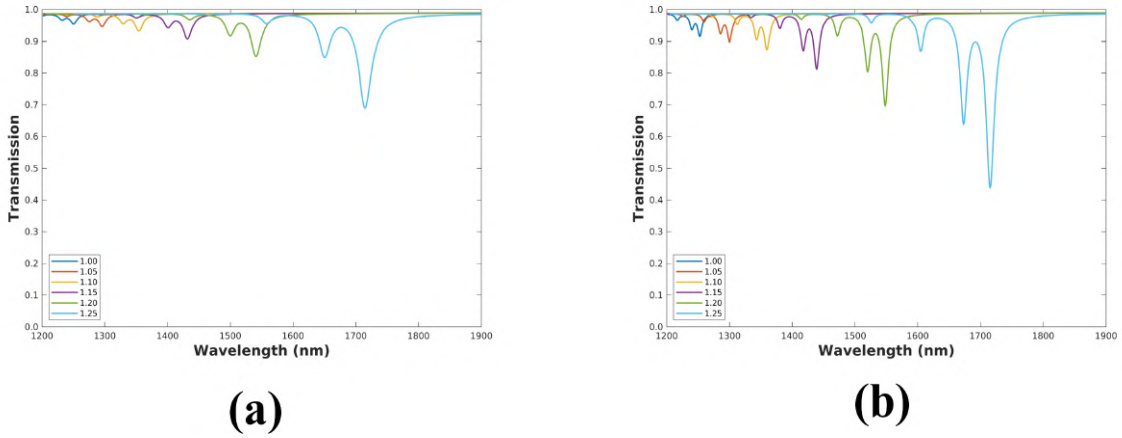

Figure 5-15.: Spectral response of the BSW sensing structure based on a 15 mm long D-shaped PCF coated with a single layer of SnO_2. Transmission spectra for the **(a)** TE- and **(b)** TM-polarized BSWs.

Table 5-2.: FWHM, sensitivity and FOM analysis of the BSW1 in the proposed sensing structures at $n_{ext} = 1.25$.

	SnO2		***TiO2***	
	TE	**TM**	**TE**	**TM**
Sensitivity				
(nm/RIU)	4580	4554	5492	4085
FWHM				
(nm)	26.5	19.5	5.5	3.5
FOM				
(RIU^{-1})	173	234	998	1167

layer have high values of the FOM values (173 and 234 nm/RIU) compared to other sensing structures based on surface waves [8, 121]. However, the extremely narrow peaks of the resonances excited at the coated fiber with TiO_2 reach values over 1000 nm/RIU. To the best of our knowledge, it could be the highest FOM of sensing applications based on electromagnetic surface waves.

5.2.3. Conclusion

In summary, this work proposes to post-process a conventional PCF to transform it into a D-shaped PCF and deposit a single dielectric layer on its flat surface. The designed PCF was proposed as a sensing device based on BSW excitation. The single-layer coated D-shape PCF

sensing device based on BSW has higher sensitivity than other BSW based sensors and the highest FOM for sensors based on electromagnetic surface waves. In addition, it is proposed to analyze the performance of the designed sensing system based on a single-layer coated PCF, at the refractive index range of $1.33 < n_A < 1.40$, with a view to the development of biological sensors.

5.3. Summary

In summary, in this chapter two configurations to excite BSWs in PCFs from the evanescent field of the guided light in the fiber core were theoretically proposed. The proposed configuration in the first section consists of a dielectric multilayer, coating the inner walls of one hole of a suspended-core PCF. On the other side, the second proposed configuration consists of a single dielectric layer coating the photonic crystal of a processed commercial PCF. It was shown that both configurations allow the excitation of BSWs waves in PCF fibers, using different strategies to design the interface dielectric - photonic crystal. However, the designed single-layer coated PCF structure is easier to built and has substantial advantages as a sensor device, in terms of sensitivity and merit figure. Finally, remains pending to achieve the experimental evidence of one (or both) proposed systems.

6. Conclusions and future work

6.1. Conclusions

In recent decades, many technological advances have been achieved in the telecommunication and sensing fields, many of them have been driven by investigations in photonic. Within the recent investigations, the research in electromagnetic surface waves has great potential for the development of new photonic devices, especially surface waves in dielectric interfaces. In addition, as a result of the cost reduction of optical fibers and the associated equipment, there is a growing interest in all-fiber devices. This doctoral thesis offers a new perspective on the research and development of new photonic devices, by proposing the use of unconventional fibers to excite surface waves. In this way, it is possible to excite the BSW resonances, and simultaneously take advantage of the flexibility and unique advantages offered by other fibers such as PCFs.

The first chapters of this thesis focused on reviewing the current status of developments based on electromagnetic surface waves, the understanding of the general theory of ESW in dielectric interfaces and the excitation conditions of BSWs in multilayer structures, particularly in PCFs. Based on the study of the theory of electromagnetic surface waves in dielectric interfaces, a computational tool was designed to predict the behavior of the light propagating in multilayer structures. The use of this computing tool allows us to study the different Bloch modes that a multilayer structure supports and facilitates the designing process of a 1DPC that supports BSW excitation. In addition, it was proposed to excite BSWs using the evanescent field of the core-guided light in optical fibers. The coupled mode theory was used to demonstrate the veracity of the proposed excitation method, and a computational tool was designed to apply the CMT, where the electric field distribution of the coupled modes was calculated using a commercial FEM software. This tool allowed to perform the coupling analysis between two propagating modes in lossless media. Later it was possible to verify the veracity of the obtained results using the CMT-based method, applying advanced computational tools.

In addition, the first experimental verification of BSW excitation in a D-shaped fiber was carried out, where the evanescent field of the core-guided light was used to excite the surface

modes. The photonic crystal used consist of a multilayer stack of SnO_2/CuO deposited on the D-shaped fiber. The structure was designed using the developed tools, taking into account the limitations that impose the available equipment, and the experimental results were validated through computational tools. It was also shown that the multilayer structure on a D-shaped fiber is viable as a refractive index detector based on BSWs, however, its usefulness can be extended to other research areas, such as the development of optical filters, resonant cavities, among others.

Subsequently, in this thesis, two structures were proposed as sensing applications based on BSW excitation in PCFs. The first proposed structure consisted of a multilayer dielectric stack deposited inside the holes of a suspended core PCF. The stack supports BSWs excited by the evanescent field of the light guided in the PCF core. It was shown that the design properties of the multilayer structure modifies the excitation conditions of the BSW, which can be adjusted to operate in any spectral region. The proposed structure operates as an ultra-wide range refractometric sensor, with sensitivity comparable to other surface wave sensors based on SPP, but a higher figure of merit. The obtained results are promising specially with a view to the development of applications in high-resolution refractive index sensing. The second proposed sensing structure based on BSWs consisted of a single dielectric layer deposited on the flat surface on a laterally polished PCF. The structure supports BSWs excited through the evanescent field of the light guided in the PCF core. It was showed that the proposed device can operate as a refractive index sensor and the performance of different dielectric layers was analyzed. The designed sensor has a high sensitivity comparable to some LMR based sensors, preserving the spectral width of BSWs. The designed device considerably exceeds the figure of merit of most SPR and LMR sensors in optical fibers.

Finally, we can affirm that the potential to develop devices based on BSWs excitation in optical fibers has been numerically and experimentally verified. The use of unconventional fibers presents an immense range of possibilities that, if used correctly, can enhance the potential of BSWs for applications in photonic devices.

6.2. Future work

We showed that Bloch waves can be excited in commercial SMF-28 D-shaped fibers coated with a 1DPC up to six-layer of SnO_2/CuO. Notwithstanding, we consider that the obtained experimental results can be improved by optimizing the materials used in the 1DPC. In particular, it is imperative to reduce the imaginary part of refractive index of the deposited films in order to narrow the spectral width of the resonance peaks and, accordingly, increase the device figure-of-merit. We propose to continue with this research line and carry out the numerical calculations and the experimental verification.

Additionally, it is still pending to carry out the experimental verification of the proposed structures in chapter 5. On the side of BSWs in multilayer dielectric coated PCF, there exist the difficulty of making dielectric depositions inside the internal holes of the optical fiber. However, recent advances in the deposition of multilayer structures of Si/SiO_2 are found in the literature, so we expect that it can be achieved in the medium term. On the other hand, the experimental verification of the BSWs in single-layer dielectric coated PCF is contingent on achieving a good quality of the lateral polishing of the fiber. As mentioned earlier, PCFs have already been laterally polished, although the results are diverse. Currently, our research group is working on the design of a lateral polishing system to implement the D-shaped PCF and carry out the experimental evidence of the results obtained in simulations.

Finally, we believe that this work opens the door for future investigations on electromagnetic surface waves. Even though sensing applications based on ESWs had been widely studied, with a renewed emphasis on the biosensing [4, 57, 64, 75, 78, 98, 99, 131, 136, 140, 141], these waves have many other photonic applications. Among them one can find optical switching [142,143], devices active control [144,145], laser emission [146], optical resonators [147], quasicrystals [148], metamaterials [145, 149], nonlinear optics [148, 150]. Accordingly, we expect to continue developing the research line of surface electromagnetic waves in dielectric interfaces based on optical fibers.

A. Appendix: Photonic band gap

```
1
2  %% 1DPC BandGap
3
4  clc
5  clear all
6  t0 = cputime ;
7  % parpool(2)
8
9  n1 = 1.4440236217      ;    % SiO2 (Refractive index of the first layers)
10 n2 = 2.45318483577     ;    % TiO2  (Refractive index of the second layers)
11 a = 600e-9             ;    % Thickness of the first layers
12 b = 250e-9             ;    % Thickness of the first layers
13 nA = 1.0               ;    % Analyte RI
14
15 A = a + b              ;    % Structure period
16 c = 299792458          ;    % Speed of light
17 i = 0 ; j = 0 ; n = 0 ;
18
19 %% Graphs limits
20
21 x_min = 4.5e6    ;
22 x_max = 9e6      ;
23 y_min = 1.8e14   ;
24 y_max = 2.8e14   ;
25
26 %
27 N = 2000               ; % Resolution in each axis
28 w_max = 2*pi*y_max   ;
29 B_max = x_max         ;
30 w_min = 2*pi*(y_max-y_min)/N     ;
31 B_min = (x_max-x_min)/N          ;
32
33 P_w = (w_max-w_min)/N    ;
34 P_B = (B_max-B_min)/N    ;
35
36 for w = w_min : P_w : w_max
37      j = j+1 ;
38      i=0 ;
39      w_1(j) = w ;
```

```
40
41      for B = B_min : P_B : B_max
42          i = i+1 ;
43          B_1(i) = B ;
44
45          k1x = ( ((w/c)*n1)^2 - B^2 )^(1/2) ;
46          k2x = ( ((w/c)*n2)^2 - B^2 )^(1/2) ;
47
48          %ABCD Matrix : TE modes
49
50          A_TE = ( exp(-1i*k1x*a) )*( cos(k2x*b) - (1/2)*1i*( k2x/k1x + k1x/k2x
                )* sin(k2x*b) ) ;
51          B_TE = ( exp(1i*k1x*a) )*( -(1/2)*1i*( k2x/k1x - k1x/k2x )*sin(k2x*b)
                ) ;
52          C_TE = ( exp(-1i*k1x*a) )*( (1/2)*1i*( k2x/k1x - k1x/k2x )*sin(k2x*b)
                ) ;
53          D_TE = ( exp(1i*k1x*a) )*( cos(k2x*b) + (1/2)*1i*( k2x/k1x + k1x/k2x )
                *sin(k2x*b) ) ;
54
55          %ABCD Matrix : TM modes
56
57          A_TM = ( exp(-1i*k1x*a) )*( cos(k2x*b) - (1/2)*1i*( (k1x*n2^2)/(k2x*n1
                ^2) + (k2x*n1^2)/(k1x*n2^2) )*sin(k2x*b) ) ;
58          B_TM = ( exp(1i*k1x*a) )*( -(1/2)*1i*((k1x*n2^2)/(k2x*n1^2) - (k2x*n1
                ^2)/(k1x*n2^2) )*sin(k2x*b) ) ;
59          C_TM = ( exp(-1i*k1x*a) )*( (1/2)*1i*((k1x*n2^2)/(k2x*n1^2) - (k2x*n1
                ^2)/(k1x*n2^2) )*sin(k2x*b) ) ;
60          D_TM = ( exp(1i*k1x*a) )*( cos(k2x*b) + (1/2)*1i*(  (k1x*n2^2)/(k2x*n1
                ^2) + (k2x*n1^2)/(k1x*n2^2) )*sin(k2x*b) ) ;
61
62          TE(i,j) =  ( (1/2)*( A_TE + D_TE ) )  ;
63          TM(i,j) =  ( (1/2)*( A_TM + D_TM ) )  ;
64
65          ABS_TE(i,j) = abs ( (1/2)*( A_TE + D_TE ) )  ;
66          ABS_TM(i,j) = abs ( (1/2)*( A_TM + D_TM ) )  ;
67
68          ABS_TE_1 = (ABS_TE(i,j)) ;
69          if  ABS_TE_1 <= 1
70  %           K_TE_R(i,j) = 1 ;
71              K_TE_R(j,i) = 1 ;
72          else
73  %           K_TE_R(i,j) = 0 ;
74              K_TE_R(j,i) = 0 ;
75          end
76
77          ABS_TM_1 = (ABS_TM(i,j)) ;
78          if  ABS_TM_1 <= 1
79              K_TM_R(j,i) = 1 ;
```

```
80          else
81              K_TM_R(j,i) = 0 ;
82          end
83      end
84  end
85
86  [B_2,w_2] = meshgrid(B_1,w_1);
87
88  %% Experimental BSW results
89
90  D_TM = [ 1000 1.62220103673 ; 1100 1.57300497801 ; 1200 1.53544764779 ; 1300
        1.50432555898 ; 1400 1.47636033126 ; 1500 1.44967626133 ; 1600
        1.42573297071 ; 1700 1.411219 ];
91  y_TM = c ./(D_TM(:,1)*1e-9);
92  x_TM = (2*pi./(D_TM(:,1)*1e-9)).*(D_TM(:,2));
93
94  D_TE = [1000 1.98281522327 ; 1100 1.92937448658 ; 1200 1.88221289171 ; 1300
        1.8401250861 ; 1400 1.80211143391 ; 1500 1.7672894918 ; 1600
        1.7348672214 ; 1700 1.70413757583 ] ;
95  y_TE = c ./(D_TE(:,1)*1e-9)      ;
96  x_TE = (2*pi./(D_TE(:,1)*1e-9)).*(D_TE(:,2))     ;
97
98  %%
99
100 map = [1, 1, 1
101      0, 0.4, 0.7]      ;
102 nS = 1.45              ;
103
104 W_1 = B_1*c/(2*pi*1) ; % Ligth in air line
105
106 %% TM Waves BandStructure
107
108 n=n+1;
109 figure(n)
110 pcolor (B_2,w_2/(2*pi),K_TM_R)
111 axis([x_min x_max y_min y_max])
112 shading interp
113 xlabel('\beta  [m^{-1}]','FontSize',12)
114 ylabel('f  [Hz]','FontSize',12)
115 colormap(map)
116 title('TM Band structure')
117 hold on
118 plot(B_1,W_1,'--','Color',[0.2,0.2,0.2],'LineWidth',1.0)
119 plot(x_TM,y_TM,'Color',[0,0.7,0], 'LineWidth',1.5)
120 rectangle('Position',[x_min y_min (x_max-x_min) (y_max-y_min)])
121
122 %% TE Waves BandStructure
123
```

```
124 n=n+1;
125 figure(n)
126 pcolor (B_2,w_2/(2*pi),K_TE_R)
127 axis([x_min x_max y_min y_max])
128 shading interp
129 xlabel('\beta  [m^{-1}]','FontSize',12)
130 ylabel('f  [Hz]','FontSize',12)
131 colormap(map)
132 title('TE Band structure')
133 hold on
134 plot(B_1,W_1,'--','Color',[0.2,0.2,0.2],'LineWidth',1.0)
135 plot(x_TE,y_TE,'Color',[0.7,0,0], 'LineWidth',1.5)
136 rectangle('Position',[x_min y_min (x_max-x_min) (y_max-y_min)])
137
138 %% Timer
139
140 tf = cputime -t0 ;
141 disp('Elapsed time (s)')
142 disp (tf)
```

B. Appendix: Coupled mode theory

General CMT Script

```
1
2  tic
3
4  %% Theoretical model: Snyder and Love
5  % Units: um
6
7  clc
8  clear
9  close all
10 format longG
11
12 %% Linear regression
13
14 % Core dispersion data
15 data_CO = [
16 950      ,        1.444785869      ;
17 955      ,        1.444656773      ;
18 960      ,        1.444527807      ;
19 965      ,        1.444398947      ;
20 970      ,        1.444270189      ;
21 975      ,        1.444141515      ;
22 980      ,        1.444012935      ;
23 ];
24
25 %SWs dispersion data
26 data_SW = [
27 950      ,        1.446298861      ;
28 955      ,        1.445776944      ;
29 960      ,        1.445265508      ;
30 965      ,        1.444763823      ;
31 970      ,        1.444271594      ;
32 975      ,        1.443788357      ;
33 980      ,        1.443313738      ;
34 ];
35
36 %% Linear fit
37
```

```
38 fit_CO = polyfit( data_CO(:,1) , data_CO(:,2) , 1 ) ;    %Core Fit
39 m_CO = fit_CO(1)  ;  b_CO = fit_CO(2) ;
40
41 fit_SW = polyfit( data_SW(:,1) , data_SW(:,2) , 1 ) ;    %SW fit
42 m_SW = fit_SW(1)  ;  b_SW = fit_SW(2) ;
43
44 %% Resonant Wavelength
45
46 intercept = (b_SW-b_CO)/(m_CO-m_SW) ;        %Resonant Wavelength
47 intercept_L = round(intercept,1) ;           %Rounded resonant wavelength
48 neff_intercept = m_CO*intercept + b_CO ;
49 Lambda = intercept       ;
50 lambda = Lambda/1000     ;
51
52 disp('Resonant wavelength in nm')
53 disp(round(intercept,1))
54
55 %% Maximum propagation length
56
57 zf = 100 ;             %Maximum length z ( in mm )
58 zf = zf*1000 ;         %Units conversion (mm to um)
59 zp = 0.005 ;           %Step ( in um )
60 z = 0:zp:zf ;
61
62
63 %% Refractive indexes of the core (n_1) and the top layer (n_2)
64
65 %SiO2 refractive index (Sellmeier equation)
66     n_1 = sqrt(1+(0.6961663*lambda^2)/( lambda^2-((0.0684043^2)))+ (0.4079426*
          lambda^2)/(lambda^2-((0.1162414^2))) + (0.8974794*lambda^2)/( lambda
          ^2-(9.896161^2))) ;
67 %TiO2 refractive index (Sellmeier equation)
68     n_2 = sqrt(5.913+(0.2441/(lambda^2-(0.0803)))) ;
69 %Si refractive index (Sellmeier equation)
70 %     n_2 = sqrt(1+(10.6684*lambda^2)/( lambda^2-((0.3015^2)))+ (0.0030*lambda
     ^2)/(lambda^2-((1.1347^2))) + (1.5413*lambda^2)/( lambda^2-(1104.0^2) )) ;
71 %Fixed refractive index
72 %     n_2 = 1.91 ;
73
74
75 %% Electric Field Data
76
77 %Read electric field data files (COMSOL solution)
78 archivo_CO  = 'TM_BSW1_1CO.txt'   ;
79 archivo_SW  = 'TM_BSW1_2SW.txt'   ;
80 archivo_ALL = 'TM_BSW1_3All.txt'  ;
81
82 %% Execute subscript of coupling at resonant wavelength
```

```
83      Script_Coupling
84  %%
85
86      figure(2)
87      print -dpng -r600 TM_BSW1.png
88
89      disp('Saving ...')
90          save(strcat('TM_BSW1'))
91      disp('Saving COMPLETED')
92
93  % return
94
95  %% Propagation Length
96
97  z_E = 15 ;              % Length z (in mm) to calculate the transmition figure
98  z_E = z_E*1000 ;        % Units conversion (mm to um)
99
100 %% Resonance wavelength and evaluation interval
101
102 wide = 25         ;     % Spectral
103 Lambda_p = 0.01 ;       % Wavelength step
104
105 %% Execute Transmission Script at the selected wavelength bandwidth
106     Script_Transmission
107 %%
108
109     figure(3)
110     print -dpng -r600 TM_BSW1_15mm
111
112     save('TM_BSW1_15mm.mat','Lambda_plot','P1_max','Lambda_i','Lambda_f', '
            results')
113
114 %%
115
116 toc
```

Script coupling

```
1
2  % Counters
3  n = 1 ;
4  l = 0 ;
5  n_cont = 0 ;
6  ii = 0 ;
7
8  disp(archivo_CO)
```

```
9  disp(archivo_SW)
10 disp(archivo_ALL)
11 disp('     ')
12 disp('Reading electric field data ...')
13
14          % File 1: Core mode data
15          fid1 =fopen(archivo_CO,'r');
16          A=textscan(fid1,'%f %f %f %f %f %f','headerlines',0);
17          A=cell2mat(A);        fclose(fid1);
18
19          % File 2: Surface mode data
20          fid2 =fopen(archivo_SW,'r');
21          B=textscan(fid2,'%f %f %f %f %f %f','headerlines',0);
22          B=cell2mat(B);        fclose(fid2);
23
24          % File 3: n3 refractive index distribution
25          fid3 =fopen(archivo_ALL,'r');
26          C=textscan(fid3,'%f %f %f','headerlines',0);
27          C=cell2mat(C);        fclose(fid3);
28
29          %Data, core 1
30          X1 = A(:,1) ;    Y1 = A(:,2) ;    n1 = A(:,6) ;
31          Ex1 = A(:,3) ;   Ey1 = A(:,4) ;   Ez1 = A(:,5) ;
32
33          Xmin = min (X1) ;    Xmax = max (X1) ;
34          Ymin = min (Y1) ;    Ymax = max (Y1) ;
35          p = X1(2,1)-X1(1,1) ;
36
37          %Data, core 2
38          X2 = B(:,1) ;    Y2 = B(:,2) ;    n2 = B(:,6) ;
39          Ex2 = B(:,3) ;   Ey2 = B(:,4) ;   Ez2 = B(:,5) ;
40
41          %Data n_all
42          nall = C(:,3) ;
43
44          % Electric Field norm, core 1
45          normE1 = ( (abs(Ex1)).^2 + (abs(Ey1)).^2 + (abs(Ez1)).^2 ).^(1/2) ;
46          [Xq,Yq] = meshgrid(Xmin:p:Xmax,Ymin:p:Ymax);
47          V1 = griddata(X1,Y1,normE1,Xq,Yq);
48
49          % Electric Field norm, core 2
50          normE2 = ( (abs(Ex2)).^2 + (abs(Ey2)).^2 + (abs(Ez2)).^2 ).^(1/2) ;
51          V2 = griddata(X2,Y2,normE2,Xq,Yq);
52
53          clear A B C %Erase matrices A B C to free memory
54
55 disp('Reading electric field data COMPLETED')
56 disp('    ')
```

```
57
58 %%
59 clear A1 A2 ans B_1 B_2 C1 C2 D11 D12 D21 D22 f fcn fit Int_E1 Int_E1E1
       Int_E1E2 Int_E2 Int_E2E1 Int_E2E2 j k0 L L1 L2 m M P1 P2 sp V V11 V12 V21
       V22 n_0 na_1 na_2 x y yu yl yr yz zx per ym z_per z_max z_mx P1m
60 %%
61
62 disp('Transmission vs Propagation length ...')
63
64         clear P1m z_m ;
65
66         % Numerical aperture
67         NA = 0.14 ;
68         % Core refractive index
69         n_0 = sqrt( NA^2 + n_1^2 ) ;
70         % Analyte refracive index
71         f=length(n1)-1000;
72         nA = n1(f) ;
73         disp('RI :            Low index media            High index media
                          External media     ')
74         disp(round([n_1 n_2 nA],5))
75
76         neff_1 = m_CO*Lambda + b_CO ;
77         neff_2 = m_SW*Lambda + b_SW ;
78
79         % Integration terms
80
81         na_1 = (nall.^2 - n1.^2) ;
82         na_2 = (nall.^2 - n2.^2) ;
83
84         % Diferential equation solution
85
86         k0 =  2*pi/lambda ;
87         B_1 = neff_1*k0 ;
88         B_2 = neff_2*k0 ;
89
90         Int_E1E2 = sum( ( na_2 ).*( conj(Ex1).*Ex2 + conj(Ey1).*Ey2 )*(p^2) )
               ;
91         Int_E2E1 = sum( ( na_1 ).*( conj(Ex2).*Ex1 + conj(Ey2).*Ey1 )*(p^2) )
               ;
92         Int_E1E1 = sum( ( na_1 ).*( conj(Ex1).*Ex1 + conj(Ey1).*Ey1 )*(p^2) )
               ;
93         Int_E2E2 = sum( ( na_2 ).*( conj(Ex2).*Ex2 + conj(Ey2).*Ey2 )*(p^2) )
               ;
94         Int_E1 = sum( ( conj(Ex1).*Ex1 + conj(Ey1).*Ey1 ).*(p^2) ) ;
95         Int_E2 = sum( ( conj(Ex2).*Ex2 + conj(Ey2).*Ey2 ).*(p^2) ) ;
96
97         D12 = (k0/(2*n_1)) * Int_E1E2/Int_E1 ;
```

```
98          D21 = (k0/(2*n_2)) * Int_E2E1/Int_E2 ;
99          D11 = (k0/(2*n_1)) * Int_E1E1/Int_E1 ;
100         D22 = (k0/(2*n_2)) * Int_E2E2/Int_E2 ;
101
102         % Analytical Solution of the differential equations system
103
104         M = [ 1i*(B_1+D11), 1i*D12 ; 1i*D21 , 1i*(B_2+D22) ] ;
105
106         [V,L] = eig(M) ;
107
108         V11 = V(1,1) ;   V12 = V(1,2) ;
109         V21 = V(2,1) ;   V22 = V(2,2) ;
110         L1 = L(1,1) ;    L2 = L(2,2) ;
111
112         C2 = V21 / ( V12*V21-V11*V22 ) ;
113         C1 = ( -V22/V21 )*C2 ;
114
115         A1 = C1*V11*exp(L1*z) +  C2*V12*exp(L2*z) ;
116         A2 = C1*V21*exp(L1*z) +  C2*V22*exp(L2*z) ;
117
118         P1 = real(A1).^2 ;
119         P2 = real(A2).^2 ;
120
121         y = P1(:,1:(1/zp+1)) ;
122         x = z(:,1:(1/zp+1)) ;
123         yu = max(y);
124         yl = min(y);
125         yr = (yu-yl);
126         yz = y-yu+(yr/2);
127         zx = x(yz .* circshift(yz,[0 1]) <= 0);      % Find zero-crossings
128         per = 2*mean(diff(zx));                      % Estimate period
129         ym = mean(y);                                % Estimate offset
130
131         fit = @(b,x)  b(1).*(sin(2*pi*x./b(2) + 2*pi/b(3))) + b(4);      %
                Function to fit
132         fcn = @(b) sum((fit(b,x) - y).^2);                               %
                Least-Squares cost function
133         sp = fminsearch(fcn, [yr;  per;  -1;  ym]) ;
134         z_per = round(2*per/zp);
135         m = z_per*1 ;
136
137         z_max = length(z)-m ;
138         z_mx = round(length(z)/m) ;
139
140         P1m = zeros(1,z_mx-2) ;
141         z_m = zeros(1,z_mx-2) ;
142
143                 for j =  1 : z_mx-2
```

```
144                         P1m(1,j) = max ( P1(1,(j*m):(m*(j+1))) ) ;
145                         z_m(1,j) = (m*j)*zp ;
146                 end
147
148         f1_z = z ; f1_P1 = P1 ; f1_z_m = z_m ; f1_P1m = P1m ;
149
150         %% Fig.2  Electric field norm and  T vs L
151
152         % Core 1
153         figure(2)
154         subplot(2,2,1)
155         mesh (Xq,Yq,abs(V1))
156         % title('Electric field norm - Core mode')
157         view (2)
158
159         % Core 2
160         figure(2)
161         subplot(2,2,2)
162         mesh (Xq,Yq,abs(V2))
163         % title('Electric field norm - BSW mode')
164         view (2)
165
166         clear Xq Yq V1 V2 normE1 normE2
167
168         figure(2)
169         subplot(2,2,[3 4])
170         plot(f1_z/1000,f1_P1,'b','linewidth',0.1)
171         hold on
172         plot(f1_z_m/1000, f1_P1m,'k','linewidth',0.1)
173         axis([0 max(f1_z)/1000 0 1])
174         xlabel('Propagation length (mm)')
175         ylabel('Transmission')
176         title(['Resonant wavelength = ' num2str(intercept_L) ' nm'])
177
178         %%
179
180         clear A1 A2 P2 f1_z z f1_P1 P1 f1_z_m z_m f1_P1m P1m
181
182 disp('Transmission vs Propagation length COMPLETED')
183 disp('    ')
```

Script Transmission

```
1
2 format longG
3 disp('    ')
```

```
4  disp('Transmission curve ...')
5  disp('    ')
6
7  Lambda_i = intercept_L - wide/2  ;       % Initial wavelength
8  Lambda_f = intercept_L + wide/2  ;       % Final wavelength
9  Length = (Lambda_f-Lambda_i)/Lambda_p;
10
11 n_per = 20;           %100%/n_per == Amount of data to show.
12
13 z_EE2 = z_E ;
14
15 for z_EE = z_EE2
16
17         clear z z_E
18
19         z_E = z_EE ;    % Change if it is necessary to evaluate another
               propagation length
20
21         z =  z_E-m*zp/2 : zp : z_E+m*zp/2 ;
22
23         Lambda_plot = Lambda_i : Lambda_p : Lambda_f;
24         ii = 0 ;
25         nP = -1 ;
26
27                 P1m = zeros(1,z_mx-2) ;
28                 z_m = zeros(1,z_mx-2) ;
29                 P1_max = zeros(1,Length+1) ;
30
31                 Lambda_vector = Lambda_i : Lambda_p : Lambda_f ;
32                 n_dat = length(Lambda_vector);
33                 n_per2 = round(n_dat/n_per) ;
34
35         % parfor jj = 1:n_dat
36         for jj = 1:n_dat
37
38                 Lambda = Lambda_vector(jj);
39                 lambda = Lambda/1000 ;
40
41         %****************************************************************
42         %  Remove this section if 'parfor' is active
43                 nP = nP + 1 ;
44                 n_cont = n_cont + 1 ;
45                 if n_cont == n_per2
46                         P = round(100*nP/Length) ;
47                         disp(['Wavelength = ' num2str(Lambda) ' nm          '
                              num2str(P) ' % Completed' ])
48                         n_cont = 0;
49                 end
```

```
50  %*************************************************************
51
52  % Numerical aperture
53  NA = 0.14 ;
54  % Core refractive index
55  n_0 = sqrt( NA^2 + n_1^2 ) ;
56  % Analyte refracive index
57  f=length(n1)-1000;
58  nA = n1(f) ;
59
60  neff_1 = m_CO*Lambda + b_CO ;
61  neff_2 = m_SW*Lambda + b_SW ;
62
63  % Integration terms
64
65  na_1 = (nall.^2 - n1.^2) ;
66  na_2 = (nall.^2 - n2.^2) ;
67
68  % Diferential equation solution
69
70  k0 =  2*pi/lambda ;
71  B_1 = neff_1*k0 ;
72  B_2 = neff_2*k0 ;
73
74  Int_E1E2 = sum( ( na_2 ).*( conj(Ex1).*Ex2 + conj(Ey1).*Ey2 )*(p^2) )
        ;
75  Int_E2E1 = sum( ( na_1 ).*( conj(Ex2).*Ex1 + conj(Ey2).*Ey1 )*(p^2) )
        ;
76  Int_E1E1 = sum( ( na_1 ).*( conj(Ex1).*Ex1 + conj(Ey1).*Ey1 )*(p^2) )
        ;
77  Int_E2E2 = sum( ( na_2 ).*( conj(Ex2).*Ex2 + conj(Ey2).*Ey2 )*(p^2) )
        ;
78  Int_E1 = sum( ( conj(Ex1).*Ex1 + conj(Ey1).*Ey1 ).*(p^2) ) ;
79  Int_E2 = sum( ( conj(Ex2).*Ex2 + conj(Ey2).*Ey2 ).*(p^2) ) ;
80
81  D12 = (k0/(2*n_1)) * Int_E1E2/Int_E1 ;
82  D21 = (k0/(2*n_2)) * Int_E2E1/Int_E2 ;
83  D11 = (k0/(2*n_1)) * Int_E1E1/Int_E1 ;
84  D22 = (k0/(2*n_2)) * Int_E2E2/Int_E2 ;
85
86  % Analytical Solution of the differential equations system
87
88  M = [ 1i*(B_1+D11), 1i*D12 ; 1i*D21 , 1i*(B_2+D22) ] ;
89
90  [V,L] = eig(M) ;
91
92  V11 = V(1,1) ;   V12 = V(1,2) ;
93  V21 = V(2,1) ;   V22 = V(2,2) ;
```

```
94          L1 = L(1,1) ;    L2 = L(2,2) ;
95
96          C2 = V21 / ( V12*V21-V11*V22 ) ;
97          C1 = ( -V22/V21 )*C2 ;
98
99          A1 = C1*V11*exp(L1*z) +  C2*V12*exp(L2*z) ;
100         A2 = C1*V21*exp(L1*z) +  C2*V22*exp(L2*z) ;
101
102         P1 = real(A1.^2) ;
103         P2 = real(A2.^2) ;
104
105         P1_max(jj) = max ( P1 ) ;
106
107         end
108
109         disp('    ')
110         disp('Transmission curve COMPLETED')
111         disp('    ')
112
113         [MIN,pos] = min(P1_max)                    ;
114         Lambda_plot(pos)
115
116         a1 = pos                                   ;
117         a2 = length(Lambda_plot) - pos             ;
118         kk_max = min (a1,a2) - 1                   ;
119         P1_max2 = P1_max                           ;
120
121         for kk = 1:1:kk_max
122                 P1_max2(pos+kk) = ( P1_max(pos+kk) + P1_max(pos-kk) )/2 ;
123                 P1_max2(pos-kk) = P1_max2(pos+kk)
                                                       ;
124         end
125
126         %% Transmission
127
128         figure(3)
129         plot(Lambda_plot,P1_max2,'b','Linewidth',1.5)
130         xlim([round(Lambda_i) round(Lambda_f)])
131         ylim([0  1])
132         xlabel('Wavelength (nm)','FontSize',12)
133         ylabel('Transmission','FontSize',12)
134         set(gca,'yticklabel',num2str(get(gca,'ytick')','%.1f'))
135
136         %% Transmission in dB
137         % logP1_max2 = 10*log10(P1_max2) ;
138         % n=n+1;
139         % figure(4)
140         % plot(Lambda_plot,logP1_max2,'b','Linewidth',1.5)
```

```
141         %xlim([Lambda_i Lambda_f])
142         %ylim([-inf  0])
143         %%plot(x_2,TE_2,'b','Linewidth',1.5)
144         %xlabel('Wavelength (nm)','FontSize',12) ;
145         %ylabel('Transmission (dB)','FontSize',12) ;
146
147         clear fit x y
148         x = Lambda_plot.' ;
149         y = P1_max2.' ;
150         fmin = min(y);
151         y2 = y-max(y) ;
152         f1 = fit(x,y2,'gauss1');
153         a0 = f1.a1 ;      b0 = f1.b1 ;     c0 = f1.c1 ;
154
155
156         f = fit(x,y2,'gauss5');
157
158                 a1 = f.a1 ;      b1 = f.b1 ;     c1 = f.c1 ;
159                 a2 = f.a2 ;      b2 = f.b2 ;     c2 = f.c2 ;
160                 a3 = f.a3 ;      b3 = f.b3 ;     c3 = f.c3 ;
161                 a4 = f.a4 ;      b4 = f.b4 ;     c4 = f.c4 ;
162                 a5 = f.a5 ;      b5 = f.b5 ;     c5 = f.c5 ;
163
164                 G1 =  a0*exp(-((x-b0)/c0).^2) + 1 ;
165                 G5 =  a1*exp(-((x-b1)/c1).^2) + a2*exp(-((x-b2)/c2).^2) + a3*
                        exp(-((x-b3)/c3).^2) + a4*exp(-((x-b4)/c4).^2) + a5*exp
                        (-((x-b5)/c5).^2) + 1 ;
166
167                 figure(5)
168                 plot(x,y,'b')
169                 hold on
170                 plot(x,G1,'k:')
171                 hold on
172                 plot(x,G5,'r--')
173                 hold on
174                 plot([min(x) max(x)],[(1+fmin)/2 (1+fmin)/2],'k--')
175         %     title(['Wide = ' Ancho ' nm'])
176                 h=legend('Data','Gauss fit','Gauss5 fit','Half maximun','
                        Location','southeast') ;
177                 set(h,'FontSize',10) ;
178                 xlabel('Wavelength (nm)','FontSize',12) ;
179                 ylabel('Transmission (dB)','FontSize',12) ;
180                 xlim([Lambda_i Lambda_f])
181                 ylim([0  1])
182
183                 f1 =  @(w)a1*exp(-((w-b1)/c1)^2) + a2*exp(-((w-b2)/c2)^2) + a3
                        *exp(-((w-b3)/c3)^2) + a4*exp(-((w-b4)/c4)^2) + a5*exp(-((
                        w-b5)/c5)^2) + (1-fmin)/2 ;
```

```
184                 raiz1 = fzero(f1,[min(x), b0]) ;
185                 raiz2 = fzero(f1,[b0, max(x)]) ;
186                FWHM = raiz2 - raiz1;
187
188                 results = [round(b0,2), round(FWHM,2), round(100*(1-fmin),1)]
                        ;
189                 disp('                    CENTER (nm)                    FWHM Gauss5 (
                        nm)              MAX LOSSES (%)')
190                 disp(results)
191
192 end
```

References

[1] Junxi Zhang, Lide Zhang, and Wei Xu. Surface plasmon polaritons: physics and applications. *Journal of Physics D: Applied Physics*, 45(11):113001, 2012.

[2] Xiangang Luo and Lianshan Yan. Surface plasmon polaritons and its applications. *IEEE Photonics Journal*, 4(2):590 – 595, 2012.

[3] R. C. Jorgenson and S. S. Yee. A fiber-optic chemical sensor based on surface plasmon resonance. *Sensors and Actuators B: Chemical*, 12(3):213–220, 1993.

[4] Sujan Chakma, Md Abdul Khalek, Bikash Kumar Paul, Kawsar Ahmed, Md Rabiul Hasan, and Ali Newaz Bahar. Gold-coated photonic crystal fiber biosensor based on surface plasmon resonance: Design and analysis. *Sensing and Bio-Sensing Research*, 18(February):7–12, 2018.

[5] A. V. Kavokin, I. A. Shelykh, and G. Malpuech. Lossless interface modes at the boundary between two periodic dielectric structures. *Physical Review B*, 72:233102, 2005.

[6] Jr. John A. Polo, Tom G. Mackay, and Akhlesh Lakhtakia. *Electromagnetic Surface Waves*. Elsevier, 2013.

[7] Emiliano Descrovi, Tristan Sfez, Lorenzo Dominici, Wataru Nakagawa, Francesco Michelotti, Fabrizio Giorgis, and Hans-Peter Herzig. Near-field imaging of Bloch surface waves on silicon nitride one-dimensional photonic crystals. *Optic Express*, 16(8):5453–5464, 2008.

[8] Dora Juan Juan Hu, Ho Pui Ho, and Received Month Day. Recent advances in plasmonic photonic crystal fibers: design, fabrication and applications. *Adv. Opt. Photonics*, 9(2):257–314, 2017.

[9] Michele Scaravilli, Alberto Micco, Giuseppe Castaldi, Giuseppe Coppola, Mariano Gioffrè, Mario Iodice, Vera La Ferrara, Vincenzo Galdi, and Andrea Cusano. Excitation of Bloch Surface Waves on an Optical Fiber Tip. *Advanced Optical Materials*, 6(19):1–10, 2018.

[10] Marco Consales, Marco Pisco, and Andrea Cusano. Lab-on-fiber technology: A new avenue for optical nanosensors. *Photonic Sensors*, 2(4):289–314, 2012.

[11] R. M. Wynne. A fabrication process for microstructured optical fibers. *Journal of Lightwave Technology*, 24:4304 – 4313, 2006.

[12] T. A. Birks, J. C. Knight, and P. St. J. Russell. Endlessly single-mode photonic crystal fiber. *Optics Letters*, 22(13):961–963, 1997.

[13] J.C. Knight, J. Arriaga, T.A. Birks, A. Ortigosa-Blancha, W.J. Wadsworth, and P.St.J. Russell. Anomalous dispersion in photonic crystal fiber. *IEEE Photonics Technology Letters*, 12(7):807–809, 2000.

[14] Chuang Wu, Bai-Ou Guan, Zhi Wang, and Xinhuan Feng. Characterization of pressure response of Bragg gratings in grapefruit microstructured fibers. *Optics Letters*, 30(14):1785–1787, 2005.

[15] Kazunori Suzuki, Hirokazu Kubota, Satoki Kawanishi, Masatoshi Tanaka, and Moriyuki Fujita. Optical properties of a low-loss polarization-maintaining photonic crystal fibers. *Optics Express*, 9(13):676–680,, 2001.

[16] Andrew Michie, John Canning, Mattias Åslund Katja Lyytikäinen, and Justin Digweed. Temperature independent highly birefringent photonic crystal fibre. *Optics Express*, 12(21):5160–5165, 2004.

[17] Hyun-Min Kim, Tae-Hun Kim, Bongkyun Kim, and Youngjoo Chung. Enhanced transverse load sensitivity by using a highly birefringent photonic crystal fiber with larger air holes on one axis. *Aplied Optics*, 49(20):3841–3845, 2010.

[18] J. F. Botero-Cadavid, J. D. Causado-Buelvas, and P. Torres. Spectral properties of locally pressed fiber Bragg gratings written in polarization maintaining fibers. *Journal of Lightwave Technology*, 28(9):1291–1297,, 2010.

[19] Charles Jewart, Kevin P. Chen, Ben McMillen, Michael M. Bails, and Steven P. Levitan. Sensitivity enhancement of fiber Bragg gratings to transverse stress by using microstructural fibers. *Optics Letters*, 31(15):2260–2262, 2006.

[20] Cicero Martelli, John Canning, Nathaniel Groothoff, and Katja Lyytikainen. Strain and temperature characterization of photonic crystal fiber Bragg gratings. *Optics Letters*, 30(14):1785–1787, 2005.

[21] G. S. Wiederhecker, C. M. B. Cordeiro, F. Couny, F. Benabid, S. A. Maier, J. C. Knight, C. H. B. Cruz, and H. L. Fragnito. Field enhancement within an optical fibre

with a subwavelength air core. *Nature Photonics*, 1(2):115–118, 2007.

[22] E. Reyes-Vera, E. González-Valencia, J. F. Botero-Cadavid, P. Torres, G. Chesini, and C.M.B. Cordeiro. Induced birefringence analysis in an all-fiber device based on photonic crystal fiber with integrated electrodes. In *Latin America Optics and Photonics Conference (LAOP) (Optical Society of America, Washington, DC), ThF2*, 2010.

[23] Erick Estefen Reyes Vera. Análisis de una fibra Óptica microestructurada con electrodos internos. Thesis (physical engineer), Universidad Nacional de Colombia – Sede Medellín, Facultad de Ciencias, 2009.

[24] Anuj K. Sharma, Rajan Jha, and B. D. Gupta. Fiber-optic sensors based on surface plasmon resonance: A comprehensive review. *IEEE Sensors Journal*, 7(8):1118–1129, 2007.

[25] R. H. Ritchie. Plasma losses by fast electrons in thin films. *Phys.Rev*, 106(5):874–881, 1957.

[26] John A. Polo and A. Lakhtakia. Surface electromagnetic waves: A review. *Laser and Photonics Reviews*, 5(2):234–246, 2011.

[27] T. Turbadar. Complete absorption of light by thin metal films. *Proc. Phys. Soc*, 73(1):40–44, 1959.

[28] Andreas Otto. Excitation of nonradiative surface plasma waves in silver by the method of frustrated total reflection. *Zeitschrift fur Physik*, 216(4):398–410, 1968.

[29] E. Kretschmann and H. Raether. Radiative decay of non radiative surface plasmons excited by light. *Z. Naturforsch.*, A 23:2135–2136, 1968.

[30] Jirí Homola, Sinclair S. Yee, and Gunter Gauglitz. Surface plasmon resonance sensors: review. *Sensors and Actuators B: Chemical*, 54(1-2):3–15, 1999.

[31] Raman Kashyap and Galina Nemova. Surface plasmon resonance-based fiber and planar waveguide sensors. *Journal of Sensors*, 2009:1–9, 2009.

[32] Hyungseok Pang, HyoungJ. Cho, and PatrickL. Likamwa. On-Chip Surface Plasmon Resonance Sensor. *Journal of Nanoscience and Nanotechnology*, 8(10):4968–4971, 2008.

[33] Jae Heon Ahn, Tae Yeon Seong, Won Mok Kim, Taek Sung Lee, Inho Kim, and Kyeong-Seok Lee1. Fiber-optic waveguide coupled surface plasmon resonance sensor. *Optic Express*, 20(19):21729–21738, 2012.

[34] Mikhail Erdmanis, Diana Viegas, Markus Hautakorpi, Steffen Novotny, Jose Luis Santos, and Hanne Ludvigsen. Comprehensive numerical analysis of a surface-plasmon-resonance sensor based on an H-shaped optical fiber. *Optics Express*, 19(15):13980–13988, 2011.

[35] Amrit Patnaik, K. Senthilnathan, and Rajan Jha. Graphene-Based Conducting Metal Oxide Coated D-Shaped Optical Fiber SPR Sensor. *IEEE Photonics Technology Letters*, 27(23):2437–2440, 2015.

[36] Nelson Gómez-Cardona and Pedro Torres. Sensitivity analysis of SPR sensors based on suspended-core microstructured optical fibers. In *Latin America Optics and Photonics Conference (Optical Society of America, 2012), LS4C.2*, 2012.

[37] Nelson Dario Gomez Cardona. Modelización y realización experimental de sensores de campo evanescente basados en resonancia de plasmones de superficie en fibras ópticas. Master thesis, Universidad Nacional de Colombia – Sede Medellín, Facultad de Ciencias, 2011.

[38] Ignacio Del Villar, Francisco J. Arregui, Carlos R. Zamarreño, Jesus M. Corres, Candido Bariain, Javier Goicoechea, Cesar Elosua, Miguel Hernaez, Pedro J. Rivero, Abian B. Socorro, Aitor Urrutia, Pedro Sanchez, Pablo Zubiate, Diego Lopez, Nerea De Acha, Joaquin Ascorbe, and Ignacio R. Matias. Optical sensors based on lossy-mode resonances. *Sensors and Actuators, B: Chemical*, 240:174–185, 2017.

[39] F Yang and J.R. Sambles. Determination of the optical permittivity and thickness of absorbing films using long range modes. *Journal of Modern Optics*, 44(6):1155–1163, 1997.

[40] I. Del Villar, C. R. Zamarreño, M. Hernaez, P. Sanchez, F. J. Arregui, and I. R. Matias. Generation of Surface Plasmon Resonance and Lossy Mode Resonance by thermal treatment of ITO thin-films. *Optics and Laser Technology*, 69:1–7, 2015.

[41] Ignacio Del Villar, Victor Torres, and Miguel Beruete. Experimental demonstration of lossy mode and surface plasmon resonance generation with Kretschmann configuration. *Optics Letters*, 40(20):4739, 2015.

[42] V. Torres, M. Beruete, P. Sánchez, and I. Del Villar. Indium tin oxide refractometer in the visible and near infrared via lossy mode and surface plasmon resonances with Kretschmann configuration. *Applied Physics Letters*, 108(4):043507, 2016.

[43] M. I. D'yakonov. New type of electromagneticwave propagating at an interface. *Sov. Phys. JETP*, 67(4):714–716, 1988.

[44] Osamu Takayama, Lucian Crasovan, David Artigas, and Lluis Torner. Observation of Dyakonov surface waves. *Physical Review Letters*, 102(4):043903, 2009.

[45] Kartiek Agarwal, John A. Polo, and Akhlesh Lakhtakia. Theory of Dyakonov–Tamm waves at the planar interface of a sculptured nematic thin film and an isotropic dielectric material. *Journal of Optics A: Pure and Applied Optics*, 11(7):074003, 2009.

[46] Drew Patrick Pulsifer, Muhammad Faryad, and Akhlesh Lakhtakia. Observation of the Dyakonov–Tamm wave. *Physical Review Letters*, 111(24):243902, 2013.

[47] Drew Patrick Pulsifer, Muhammad Faryad, and Akhlesh Lakhtakia. Parametric investigation of prism-coupled excitation of Dyakonov–Tamm waves. *Journal of Optical Society of America B*, 30(8):2081–2089, 2013.

[48] Farhat Abbas, Akhlesh Lakhtakia, Qaisar A. Naqvi, and Muhammad Faryad. An optical-sensing modality that exploits Dyakonov–Tamm waves. *Phonotincs Research*, 3(1):5–8, 2015.

[49] Felix Bloch. Über die quantenmechanik der elektronen in kristallgittern. *Zeitschrift für Physik*, 52(7):555–600, Jul 1929.

[50] Igor Yevgenyevich Tamm. Über eine mögliche art der elektronenbindung an kristalloberflächen. *Zeitschrift für Physik*, 72(11):849–850, 1932.

[51] Pochi Yeh, Amnon Yariv, and Chi-Shain Hong. Electromagnetic propagation in periodic stratified media. I. General theory. *Journal of the Optical Society of America*, 67(4):423–438, 1977.

[52] Pochi Yeh, Amnon Yariv, and A. Y. Cho. Optical surface waves in periodic layered media. *Applied Physics Letters*, 32(2):105–105, 1978.

[53] Muhammad Umar Khan and Brian Corbett. Bloch surface wave structures for high sensitivity detection and compact waveguiding. *Science and Technology of Advanced Materials*, 17(1):398–409, 2016.

[54] Yanhui Li, Tianlin Yang, Zhiyong Pang, Guiqiang Du, Shumei Song, and Shenghao Han. Phase-sensitive Bloch surface wave sensor based on variable angle spectroscopic ellipsometry. *Optic Express*, 22(18):21403–21410, 2014.

[55] Weijing Kong, Zheng Zheng, Yuhang Wan, Shuna Li, and Jiansheng Liu. High-sensitivity sensing based on intensity-interrogated Bloch surface wave sensors. *Sensors and Actuators B: Chemical*, 193:467–471, 2014.

[56] Shuna Li, Jiansheng Liu, Zheng Zheng, Yuhang Wan, Weijing Kong, and Yu Sun. Highly sensitive, Bloch surface wave D-type fiber sensor. *IEEE Sensors Journal*, 16(5):1200–1204, 2016.

[57] Marco Liscidini and J. E. Sipe. Enhancement of diffraction for biosensing applications via Bloch surface waves. *Applied Physics Letters*, 91(25):253125–3, 2007.

[58] T. Kovalevich, P. Boyer, M. Suarez, R. Salut, M.S. Kim, H.P Herzig, M.P. Bernal, and T. Grosjean. Polarization controlled directional propagation of Bloch surface wave. *Optic Express*, 25(6):5710–5715, 2017.

[59] Emiliano Descrovi, Tristan Sfez, Marzia Quaglio, Daniele Brunazzo, Lorenzo Dominici, Francesco Michelotti, Hans Peter Herzig, Olivier J. F. Martin, , and Fabrizio Giorgis. Guided Bloch surface waves on ultrathin polymeric ridges. *Nano Letters*, 10(6):2087–2091, 2010.

[60] Bobo Du, Yangwu Li, Dexing Yang, and Hua Lu. High-performance optical sensing based on electromagnetically induced transparency-like effect in Tamm plasmon multilayer structures. *Applied Optics*, 58(17):4569, 2019.

[61] A. Y. Cho, A. Yariv, and P. Yeh. Observation of confined propagation in Bragg waveguides. *Applied Physics Letters*, 30(9):471–472, 1977.

[62] W. M. Robertson and M. S. May. Surface electromagnetic wave excitation on one-dimensional photonic band-gap arrays. *Applied Physics Letters*, 74(13):1800–1802, 1999.

[63] F. Villa, L. E. Regalado, F. Ramos-Mendieta, J. Gaspar-Armenta, and T. Lopez-Ríos. Photonic crystal sensor based on surface waves for thin-film characterization. *Optics Letters*, 27(8):646–648, 2002.

[64] Valery N. Konopsky and Elena V. Alieva. Photonic crystal surface waves for optical biosensors. *Analytical chemistry*, 79(12):4729–4735, 2007.

[65] Marco Liscidini, Dario Gerace, Daniele Sanvitto, and Daniele Bajoni. Guided Bloch surface wave polaritons. *Applied Physics Letters*, 98(12):121118, 2011.

[66] T. Tu, F. Pang, S. Zhu, J. Cheng, H. Liu, J. Wen, and T. Wang. Excitation of Bloch surface wave on tapered fiber coated with one-dimensional photonic crystal for refractive index sensing. *Optic Express*, 25(8):9019–9027, 2017.

[67] Qi Wang and Wan Ming Zhao. A comprehensive review of lossy mode resonance-based fiber optic sensors. *Optics and Lasers in Engineering*, 100:47–60, 2018.

[68] Letizia De Maria, Mario Martinelli, and Giorgio Vegetti. Fiber-optic sensor based on surface plasmon interrogation. *Sensors and Actuators B: Chemical*, 12(3):221–223, 1993.

[69] Radan Slavík, Jirí Homola, and Jirí Ćtyroký. Single-mode optical fiber surface plasmon resonance sensore optical fiber surface plasmon resonance. *Sensors and Actuators B: Chemical*, 54(1-2):74–79, 1999.

[70] M. Piliarik, J. Homola, Z. Maníková, and J. Ćtyroký. Surface plasmon resonance sensor based on a single-mode polarization-maintaining optical fiber. *Sensors and Actuators B: Chemical*, 90(1-3):236–242, 2003.

[71] A. Trouillet, C. Ronot-Trioli, C. Veillas, and H. Gagnaire. Chemical sensing by surface plasmon resonance in a multimode optical fibre. *Pure and Applied Optics: Journal of the European Optical Society Part A*, 5(2):227–237, 1995.

[72] Carlos Avelino de Jesus Gouveia. *Refractometric Platforms for Label-Free Biochemical Sensing*. PhD thesis, Universidade da Madeira, 2013.

[73] A. Diéz, M.V. Andrés, and J.L. Cruz. In-line fiber-optic sensors based on the excitation of surface plasma modes in metal-coated tapered fibers. *Sensors and Actuators B: Chemical*, 73(2-3):95–99, 2001.

[74] Yoon-Chang Kim, Wei Peng, Soame Banerji, and Karl S. Booksh. Tapered fiber optic surface plasmon resonance sensor for analyses of vapor and liquid phases. *Optics Letters*, 30(17):2218–2220, 2005.

[75] Ming-Hung Chiu, Shinn-Fwu Wang, and Rong-Seng Chang. D-type fiber biosensor based on surface-plasmon resonance technology and heterodyne interferometry. *Optic Letters*, 30(3):233–235, 2005.

[76] Ming-Hung Chiu, Chih-Hsien Shih, and Ming-Hsin Chi. Optimum sensitivity of single-mode D-type optical fiber sensor in the intensity measurement. *Sensors and Actuators B: Chemical*, 123(2):1120–1124, 2007.

[77] Mikhail Erdmanis, Diana Viegas, Markus Hautakorpi, Steffen Novotny, José Luis Santos, and Hanne Ludvigsen. Comprehensive numerical analysis of a surface-plasmon-resonance sensor based on an H-shaped optical fiber. *Optics Express*, 19(15):13980–13988, 2011.

[78] Maksim Skorobogatiy and Andrei V. Kabashin. Photon crystal waveguide-based surface plasmon resonance biosensor. *Applied Physics Letters*, 89(14):143518, 2006.

[79] A. Hassani and M. Skorobogatiy. Design of the microstructured optical fiber-based surface plasmon resonance sensors with enhanced microfluidics. *Optic Express*, 14(24):11616–11621, 2006.

[80] A. S. Webb, F. Poletti, D. J. Richardson, and J. K. Sahu. Suspended-core holey fiber for evanescent-field sensing. *Optical Engineering Letters*, 46(1):010503, 2007.

[81] M. Bravo, A. M. R. Pinto, M. Lopez-Amo, J. Kobelke, and K. Schuster. High precision micro-displacement fiber sensor through a suspended-core Sagnac interferometer. *Optics Letters*, 37(2):202–204, 2012.

[82] Salvador Torres-Peiro, Antonio Dıez, Jose Luis Cruz, and Miguel Vicente Andres. Temperature sensor based on Ge-doped microstructured fibers. *Journal of Sensors*, 2009:1–5, 2009.

[83] Markus Hautakorpi, Maija Mattinen, and Hanne Ludvigsen. Surface-plasmon-resonance sensor based on three-hole microstructured optical fiber. *Optics Express*, 16(12):8427–8432, 2008.

[84] Xia Yu, Ying Zhang, Shanshan Pan, Ping Shum, Min Yan, Yehuda Leviatan, and Changming Li. A selectively coated photonic crystal fiber based surface plasmon resonance sensor. *Journal of Optics*, 22(1):1–4, 2010.

[85] Jianrong Xue, Shuguang Li, Yuzhe Xiao, Wei Qin, Xujun Xin, and Xingping Zhu. Polarization filter characters of the gold-coated and the liquid filled photonic crystal fiber based on surface plasmon resonance. *Optics Express*, 21(11):13733–13740, 2013.

[86] Nelson D. Gómez-Cardona, Erick Reyes-Vera, and Pedro Torres. Multi-plasmon resonances in microstructured optical fibers: Extending the detection range of SPR sensors and a multi-analyte sensing technique. *IEEE Sens. J.*, 18(18):7492–7498, 2018.

[87] Ignacio Del Villar, Carlos R. Zamarreño, Miguel Hernaez, Francisco J. Arregui, and Ignacio R. Matias. Lossy mode resonance generation with indium-tin-oxide-coated optical fibers for sensing applications. *Journal of Lightwave Technology*, 28(1):111–117, 2010.

[88] A. Tz Andreev, B. S. Zafirova, E. I. Karakoleva, A. O. Dikovska, and P. A. Atanasov. Highly sensitive refractometers based on a side-polished single-mode fibre coupled with a metal oxide thin-film planar waveguide. *Journal of Optics A: Pure and Applied Optics*, 10(3):035303, 2008.

[89] Pedro Sanchez, Carlos R. Zamarreño, Miguel Hernaez, Ignacio R. Matias, and Francisco J. Arregui. Optical fiber refractometers based on Lossy Mode Resonances by means

of SnO2 sputtered coatings. *Sensors and Actuators, B: Chemical*, 202:154–159, 2014.

[90] Aritz Ozcariz, Iñaki Martinez, Carlos Ruiz Zamarreño, and Francisco Javier Arregui. Development of Copper Oxide Thin Film for Lossy Mode Resonance-Based Optical Fiber Sensor. *Proceedings*, 2(13):893, 2018.

[91] Miguel Hernáez, Ignacio Del Villar, Carlos R. Zamarreño, Francisco J. Arregui, and Ignacio R. Matias. Optical fiber refractometers based on lossy mode resonances supported by TiO2 coatings. *Sensors and Actuators, B: Chemical*, 49(20):3980–3985, 2010.

[92] P. Sanchez, C. R. Zamareño, M. Hernaez, I. Del Villar, C. Fernandez-Valdivielso, I. R. Matias, and F. J. Arregui. Lossy mode resonances toward the fabrication of optical fiber humidity sensors. *Measurement Science and Technology*, 23(1):014002, 2012.

[93] J. Ascorbe, J. M. Corres, I. R. Matias, and F. J. Arregui. High sensitivity humidity sensor based on cladding-etched optical fiber and lossy mode resonances. *Sensors and Actuators, B: Chemical*, 233:7–16, 2016.

[94] P. Zubiate, C. R. Zamarreño, I. Del Villar, I. R. Matias, and F. J. Arregui. D-shape optical fiber pH sensor based on Lossy Mode Resonances (LMRs). *2015 IEEE SENSORS - Proceedings*, pages 1–4, 2015.

[95] P. Zubiate, C. R. Zamarreño, I. Del Villar, I. R. Matias, and F. J. Arregui. Tunable optical fiber pH sensors based on TE and TM Lossy Mode Resonances (LMRs). *Sensors and Actuators, B: Chemical*, 231:484–490, 2016.

[96] Satyendra K. Mishra, Sruthi P. Usha, and Banshi D. Gupta. A lossy mode resonance-based fiber optic hydrogen gas sensor for room temperature using coatings of ITO thin film and nanoparticles. *Measurement Science and Technology*, 27(4):045103, 2016.

[97] Uilian José Dreyer, Aritz Ozcariz, Joaquín Ascorbe, Pablo Zubiate, Ignacio Vitoria, Cicero Martelli, Jean Carlos Cardozo da Silva, and Carlos Ruiz Zamarreño. Gas Detection Using LMR-Based Optical Fiber Sensors. *Proceedings*, 2(13):890, 2018.

[98] A. B. Socorro, J. M. Corres, I. Del Villar, F. J. Arregui, and I. R. Matias. Fiber-optic biosensor based on lossy mode resonances. *Sensors and Actuators, B: Chemical*, 174:263–269, 2012.

[99] A.B. Socorro-Leránoz, D. Santano, I. Del Villar, and I.R. Matias. Trends in the design of wavelength-based optical fibre biosensors (2008–2018). *Biosensors and Bioelectronics: X*, 1(1):100015, 2019.

[100] Abian B. Socorro, Ignacio Del Villar, Jesus M. Corres, Francisco J. Arregui, and Ignacio R. Matias. Tapered single-mode optical fiber pH sensor based on lossy mode resonances generated by a polymeric thin-film. *IEEE Sensors Journal*, 12(8):2598–2603, 2012.

[101] M. Scaravilli, G. Castaldi, A. Cusano, and V. Galdi. Grating-coupling-based excitation of Bloch surface waves for lab-on-fiber optrodes. *Optic Express*, 24(24):27771–27784, 2016.

[102] M. Scaravilli, G. Castaldi, A. Cusano, and V. Galdi. High-sensitivity label-free optical fiber optrodes based on the excitation of Bloch surface waves. In *Sixth European Workshop on Optical Fibre Sensors*, 2016.

[103] Xiao-Jie Tan and Xiao-Song Zhu. Optical fiber sensor based on Bloch surface wave in photonic crystals. *Optic Express*, 24(14):16016–16026, 2016.

[104] Rajesh V. Nair and R. Vijaya. Photonic crystal sensors: An overview. *Progress in Quantum Electronics*, 34(3):89–134, 2010.

[105] Arismar Cerqueira. Recent progress and novel applications of photonic crystal fibers. *Reports on Progress in Physics*, 73(2):024401–21, 2009.

[106] F. Poli, A. Cucinotta, and S. Selleri. *Photonic Crystal Fibers: Properties and Applications*. Springer Netherlands, 2007.

[107] Esteban Gonzalez Valencia. Redes de Bragg en fibras ópticas microestructuradas. Master thesis, Universidad Nacional de Colombia – Sede Medellín, Facultad de Ciencias, 2013.

[108] J. C. Knight, T. A. Birks, P. St. J. Russell, and D. M. Atkin. All-silica single-mode optical fiber with photonic crystal cladding. *Optics Letters*, 21(19):1547–1549, 1996.

[109] F. Couny, H. Sabert, P. J. Roberts, D. P. Williams, A. Tomlinson, B. J. Mangan, L. Farr, J. C. Knight, T. A. Birks, and P. St. J. Russell. Visualizing the photonic band gap in hollow core photonic crystal fibers. *Optics Express*, 13(2):558, 2005.

[110] Bai-Ou Guan, Da Chen, Yang Zhang, Hong-Jun Wang, and Hwa-Yaw Tam. Bragg gratings in pure-silica polarization-maintaining photonic crystal fiber. *IEEE Photonics Technology Letters*, 20(3):1980–1982, 2008.

[111] Guofeng Yan, A. Ping Zhang, Guiying Ma, Binhao Wang, Bongkyun Kim, Jooeun Im, Sailing He, and Youngjoo Chung. Fiber-optic acetylene gas sensor based on microstructured optical fiber Bragg gratings. *IEEE Photonics Technology Letters*, 23(21):1588–

1590, 2011.

[112] Wenyuan Wang, Xiaojin Yin, Jian Wu, Youfu Geng, Xiaoling Tan, Yongqin Yu, Xueming Hong, Yu Du, and Xuejin Li. Realization of all-in-fiber liquid-core microstructured optical fiber. *IEEE Photonics Technology Letters*, 28(6):609 – 612, 2016.

[113] S. L. DeHaven, S. Albin, and W.C. Kelliher. Liquid filled microstructured optical fiber for x-ray detection. *Optics Express*, 18(13):13754–13760, 2010.

[114] Erick Estefen Reyes Vera. Estudio teórico y experimental de un dispositivo de fibra óptica micro-estructurada con electrodos internos. Master thesis, Universidad Nacional de Colombia – Sede Medellin, Facultad de Ciencias, 2013.

[115] Toshihito Hosaka, Yutaka Sasaki, Katsunari Okamoto, and Juichi Noda. Stress-applied polarization-maintaining optical fibers. design and fabrication. *Electronics and Communications in Japan*, 68(3):37–47, 1985.

[116] Qi Mo, Zhikun Hong, Dawei Yu, Songnian Fu, Liang Wang, Kyunghwan Oh, Ming Tang, and Deming Liu. All-fiber spatial rotation manipulation for radially asymmetric modes. *Scientific Reports*, 7(1):2539–9, 2017.

[117] Arismar Cerqueira, K. Z. Nobrega, F. Di Pasquale, and H. E. Hernandez-Figueroa. A powerful tool based on finite element method for designing photonic crystal devices. In José Neuman de Souza, Petre Dini, and Pascal Lorenz, editors, *Telecommunications and Networking - ICT 2004*, pages 287–295, Berlin, Heidelberg, 2004. Springer Berlin Heidelberg.

[118] D. Marcuse. Coupled-mode theory for anisotropic optical waveguides. *The Bell System Technical Journal*, 54(6):985–995, 1975.

[119] Xiaoming Xi. Helically twisted solid-core photonic crystal fibers. Doctoral thesis, University of Erlangen-Nuremberg, 2015.

[120] Allan W. Snyder and John D. Love. *Optical waveguide theory*. Springer US, 1983.

[121] Esteban Gonzalez-Valencia, Rodrigo Acuna Herrera, and Pedro Torres. Bloch surface wave resonance in photonic crystal fibers: towards ultra-wide range refractive index sensors. *Optics Express*, 27(6):8236–8245, 2019.

[122] Matthias Saba and Gerd Schröder-Turk. Bloch Modes and Evanescent Modes of Photonic Crystals: Weak Form Solutions Based on Accurate Interface Triangulation. *Crystals*, 5(1):14–44, 2015.

[123] Linfei Gao, Liangxiao Tang, Feifei Hu, Ruimin Guo, Xingjun Wang, and Zhiping Zhou. Active metal strip hybrid plasmonic waveguide with low critical material gain. *Optics Express*, 20(10):11487, 2012.

[124] V. Shahraam Afshar, T. M. Monro, and C. Martijn de Sterke. Understanding the contribution of mode area and slow light to the effective Kerr nonlinearity of waveguides. *Optics Express*, 21(15):18558, 2013.

[125] S. Torres-Peiró, A. Díez, J. L. Cruz, and M. V. Andrés. Fundamental-mode cutoff in liquid-filled Y-shaped microstructured fibers with Ge-doped core. *Optics Letters*, 33(22):2578–2580, 2008.

[126] Guanjun Wang, Chao Wang, Shen Liu, Jing Zhao, Changrui Liao, Xizhen Xu, Haijian Liang, Guolu Yin, and Yiping Wang. Side-opened suspended core fiber-based surface plasmon resonance sensor. *IEEE Sens. J.*, 15(7):4086–4092, 2015.

[127] Rongrui He, Pier J. A. Sazio, Anna C. Peacock, Noel Healy, Justin R. Sparks, Mahesh Krishnamurthi, Venkatraman Gopalan, and John V. Badding. Integration of gigahertz-bandwidth semiconductor devices inside microstructured optical fibres. *Nature Photonics*, 6:174–179, 2012.

[128] Bahaa E. A. Saleh and Malvin Carl Teich. *Fundamentals of photonics*. Wiley, 2007.

[129] Volkmar Brückner. *Elements of optical networking*. Vieweg+Teubner Verlag, 2011.

[130] Aleksei P. Vinogradov, Aleksandr V. Dorofeenko, Aleksandr M. Merzlikin, and Aleksandr A. Lisyansky. Surface states in photonic crystals. *Phys.-Usp.*, 53(3):243–256, 2010.

[131] Gilberto A. Rodriguez, Judson D. Ryckman, Yang Jiao, and Sharon M. Weiss. A size selective porous silicon grating-coupled bloch surface and sub-surface wave biosensor. *Biosens. Bioelectron.*, 53:486–493, 2014.

[132] Gilberto A. Rodriguez, John D. Lonai, Raymond L. Mernaugh, and Sharon M. Weiss. Porous silicon bloch surface and sub-surface wave structure for simultaneous detection of small and large molecules. *Nanoscale Research Letters*, 9:383, 2014.

[133] Bing-Hong Liu, Yong-Xiang Jiang, Xiao-Song Zhu, Xiao-Li Tang, and Yi-Wei Shi. Hollow fiber surface plasmon resonance sensor for the detection of liquid with high refractive index. *Optics Express*, 21(26):32349–32357, 2013.

[134] Yong-Xiang Jiang, Bing-Hong Liu, Xiao-Song Zhu, Xiao-Li Tang, and Yi-Wei Shi. Long-range surface plasmon resonance sensor based on dielectric/silver coated hollow

fiber with enhanced figure of merit. *Optics Letters*, 40(5):744–747, 2015.

[135] Qingli Xie, Yuzhi Chen, Xuejin Li, Zhen Yin, Lele Wang, Youfu Geng, and Xueming Hong. Characteristics of D-shaped photonic crystal fiber surface plasmon resonance sensors with different side-polished lengths. *Applied Optics*, 56(5):1550, 2017.

[136] Tiesheng Wu, Yu Shao, Ying Wang, Shaoqing Cao, Weiping Cao, Feng Zhang, Changrui Liao, Jun He, Yijian Huang, Maoxiang Hou, and Yiping Wang. Surface plasmon resonance biosensor based on gold-coated side-polished hexagonal structure photonic crystal fiber. *Optics Express*, 25(17):20313, 2017.

[137] Xianchao Yang, Ying Lu, Baolin Liu, and Jianquan Yao. Simultaneous measurement of refractive index and temperature based on SPR in D-shaped MOF. *Applied Optics*, 56(15):4369, 2017.

[138] Yuhang Wan, Zheng Zheng, Weijing Kong, Ya Liu, Zhiting Lu, and Yusheng Bian. Direct experimental observation of giant Goos – Hänchen shifts from bandgap-enhanced total internal reflection. *Optics Letters*, 36(18):3539–3541, 2011.

[139] Shuna Li, Jiansheng Liu, Zheng Zheng, Yuhang Wan, Weijing Kong, and Sun Yu. Characteristic optimization of multilayer dielectric for the Bloch-surface-wave based sensor. In *Green Computing and Communications (GreenCom)*, 2013.

[140] Francesca Frascella, Serena Ricciardi, Paola Rivolo, Valeria Moi, Fabrizio Giorgis, Emiliano Descrovi, Francesco Michelotti, Peter Munzert, Norbert Danz, Lucia Napione, Maria Alvaro, and Federico Bussolino. A fluorescent one-dimensional photonic crystal for label-free biosensing based on bloch surface waves. *Sensors*, 13:2011–2022, 2013.

[141] Maksim Skorobogatiya and Andrei V. Kabashin. Photon crystal waveguide-based surface plasmon resonance biosensor. *Applied Physics Letters*, 89(14):143518, 2006.

[142] Yuhang Wan, Weijing Kong, Zheng Zheng, Xin Zhao, Ya Liu, and Yusheng Bian. Fiber-pigtailed optical switch based on gigantic bloch-surface-wave-induced Goos-Hanchen shifts. In *2012 IEEE Photonics Conference, IPC 2012*, volume 4, pages 36–37, 2012.

[143] Yuhang Wan, Zheng Zheng, Weijing Kong, Xin Zhao, and Jiansheng Liu. Fiber-to-fiber optical switching based on gigantic bloch-surface-wave- induced goos-hanchen shifts. *IEEE Photonics Journal*, 5(1), 2013.

[144] Eun Jung Lee, Sun Young Choi, Hwanseong Jeong, Nam Hun Park, Woongbin Yim, Mi Hye Kim, Jae Ku Park, Suyeon Son, Sukang Bae, Sang Jin Kim, Kwanil Lee, Yeong Hwan Ahn, Kwang Jun Ahn, Byung Hee Hong, Ji Yong Park, Fabian Rotermund, and Dong Il Yeom. Active control of all-fibre graphene devices with electrical

gating. *Nature Communications*, 6(6851):1–6, 2015.

[145] Angelos Xomalis, Iosif Demirtzioglou, Eric Plum, Yongmin Jung, Venkatram Nalla, Cosimo Lacava, Kevin F. MacDonald, Periklis Petropoulos, David J. Richardson, and Nikolay I. Zheludev. Fibre-optic metadevice for all-optical signal modulation based on coherent absorption. *Nature Communications*, 9(1):1–7, 2018.

[146] Dietmar Korn, Matthias Lauermann, Sebastian Koeber, Patrick Appel, Luca Alloatti, Robert Palmer, Pieter Dumon, Wolfgang Freude, Juerg Leuthold, and Christian Koos. Lasing in silicon-organic hybrid waveguides. *Nature Communications*, 7:1–9, 2016.

[147] Matteo Menotti and Marco Liscidini. Optical resonators based on Bloch surface waves. *Journal of the Optical Society of America B*, 32(3):431, 2015.

[148] Barak Freedman, Ron Lifshitz, Jason W. Fleischer, and Mordechai Segev. Phason dynamics in nonlinear photonic quasicrystals. *Nature Materials*, 6(10):776–781, 2007.

[149] Zhengyu Huang, Theodore B. Norris, and Evgenii Narimanov. Nanoscale fingerprinting with hyperbolic metamaterials. *APL Photonics*, 4(2):026103, 2019.

[150] Denis Träger, Robert Fischer, Dragomir N. Neshev, Andrey A. Sukhorukov, Cornelia Denz, Wieslaw Królikowski, and Yuri S. Kivshar. Nonlinear Bloch modes in two-dimensional photonic lattices. *Optics Express*, 14(5):1913, 2006.